

NORTHWESTERN UNIVERSITY

Molecular Mechanisms of Orai1 Channel Activation by STIM1

A DISSERTATION

SUBMITTED TO THE GRADUATE SCHOOL

IN PARTIAL FULFILLMENT OF THE REQUIREMENTS

for the degree

DOCTOR OF PHILOSOPHY

Field of Life Sciences

By

Priscilla See-Wai Yeung

EVANSTON, ILLINOIS

December 2018

© Copyright by Priscilla See-Wai Yeung, 2018

All rights reserved

**ABSTRACT****Molecular Mechanisms of Orai1 Channel Activation by STIM1**

Priscilla See-Wai Yeung

Store-operated  $\text{Ca}^{2+}$  entry through Orai1 channels mediate transcriptional, proliferative, and effector cell programs in many cells and are activated through a unique inside-out mechanism involving binding of the endoplasmic reticulum  $\text{Ca}^{2+}$  sensor, STIM1, to cytoplasmic sites on Orai1. Mutations in Orai1 that block channel activation or evoke constitutive channel activity are known to cause debilitating diseases in humans such as immunodeficiency, autoimmunity, myopathy, and thrombocytopenia. However, our understanding of the underlying molecular mechanisms of these diseases is limited by gaps in our fundamental knowledge of how Orai1 channels are gated. In particular, although atomic level details of Orai structure including the pore and putative ligand binding domains are resolved, how the gating signal is communicated to the pore and opens the gate is unknown.

This dissertation synthesizes our work over the past four years on the molecular mechanisms of Orai1 gating by STIM1. Chapter 2 summarizes a project (led by Megumi Yamashita) in which we identified residue F99 as a key component of the channel gate that is activated through pore helix rotation following STIM1 binding. In Chapter 3, I present my work on the roles of the transmembrane domains (TMs) in relaying the gating signal from STIM1 binding to the pore. We used scanning mutagenesis to identify fifteen residues in TMs 1-4 whose perturbation activates Orai1 channels independently of STIM1. Cysteine accessibility analysis and molecular dynamics simulations indicated that constitutive activation of the most robust

variant, H134S, arises from a pore conformational change that opens a hydrophobic gate to augment pore hydration, similar to gating evoked by STIM1. Mutational analysis of this locus suggests that H134 acts as steric brake to stabilize the closed state of the channel. In addition, atomic packing analysis revealed distinct functional contacts between the TM1 pore helix and the surrounding TM2/3 helices, including one set mediated by a cluster of interdigitating hydrophobic residues, and another by alternative ridges of polar and hydrophobic residues. Perturbing these contacts via mutagenesis destabilizes STIM1-mediated Orai1 channel gating, indicating that these bridges between TM1 and the surrounding TM2/3 ring are critical for conveying the gating signal to the pore. These findings help develop a framework for understanding the global conformational changes and allosteric interactions between topologically distinct domains that are essential for activation of Orai1 channels. Chapter 4 discusses the potential role of human mutation Orai1 L138F in channel activation and inactivation. In Chapter 5, I present preliminary results and hypotheses about specialized features in the Orai1 protein that may facilitate pore opening, including the presence of water crevices behind the pore helices and the M101 latch that stabilizes F99 into the rotated state.

## ACKNOWLEDGEMENTS

This thesis could not be possible without everyone who helped me along this journey. I would like to first thank my thesis advisor, Murali Prakriya, who has been supportive from our first meeting in his office when he took a chance on a rotation student who knew nothing about patch clamping nor ion channels. Over the past four years, he has been a valuable source of knowledge and encouragement, and I appreciate his generosity with his time and energy in nurturing me into becoming a more independent researcher. This work would not have been possible without my mentor, scientific partner, and friend, Megumi Yamashita, battling alongside me every day to figure out how Orai1 channels open. There is no chance that I could have tested hundreds of mutants without her help and guidance. I would also like to thank everyone who has been a part of the Prakriya lab during my time here: Agila Somasundaram, Amit Jairaman, Ann Shim, Leida Tirado-Lee, Andrew Shum, Anna Toth, Lauren Sybert, Kotaro Hori, Chelsea Maguire, Michaela Novakovic, Natalie Bernstein, Nisha Shrestha, Mehdi Maneshi, Timothy Kountz, Martinna Raineri Tapias, Toneisha Stubbs, and Shogo Tsujikawa. They have been a pleasure to work with and contributed ideas during countless lab meetings.

Many thanks to our excellent molecular dynamics collaborators Christopher Ing and Régis Pomès, who have contributed significantly to this work and to many thought-provoking scientific discussions. I greatly appreciate the guidance and patience of Douglas Freymann, whose expert insights into the structural aspects of Orai1 gating has been irreplaceable, as well as that of my other thesis committee members Alfred George Jr. and Indira Raman, who have offered many helpful and constructive suggestions during our meetings. I owe a great deal of gratitude to my undergraduate research advisor, Paul Axelsen, who first sparked my interest in research and

continues to challenge me to push my limits. I would also like to thank the directors and administrators of the NU Medical Scientist Training Program (MSTP), especially Jayms Peterson, who always has an open door and gave valuable advice at crucial junctures of my journey through the program thus far. My gratitude extends to the leadership teams of the Molecular Biophysics Training Program (MBTP) and Driskill Graduate Program for providing numerous opportunities for me to develop as a scientist.

I would also like to thank my friends both outside and within Northwestern, particularly those in my cohorts of the MSTP and MBTP. It has been fun to grow together and help each other succeed. Finally, I would like to dedicate this thesis to my parents and my brother. I thank my family for supporting my decision to pursue a MD/PhD degree away from home and for helping me keep things in perspective. They have been a constant source of encouragement, prayers, and love throughout all the ups and downs of this journey.

## TABLE OF CONTENTS

7

<b>COPYRIGHT PAGE</b>	<b>2</b>
<b>ABSTRACT</b>	<b>3</b>
<b>ACKNOWLEDGEMENTS</b>	<b>5</b>
<b>TABLE OF CONTENTS</b>	<b>7</b>
<b>LIST OF FIGURES AND TABLES</b>	<b>10</b>
<b>CHAPTER 1: INTRODUCTION</b>	<b>13</b>
Store-operated calcium entry	13
Molecular components of CRAC channels	14
Permeation, selectivity, and pore architecture of Orai1 channels	16
Structure of Orai channels	19
<b>CHAPTER 2: PORE OPENING MECHANISM OF ORAI1 CHANNELS</b>	<b>20</b>
<u>Introduction</u>	20
<u>Results</u>	23
<u>Discussion</u>	27
<b>CHAPTER 3: MAPPING THE FUNCTIONAL ANATOMY OF ORAI1</b>	
<b>TRANSMEMBRANE DOMAINS FOR CRAC CHANNEL GATING</b>	<b>28</b>
<u>Introduction</u>	28
<u>Results</u>	30
Scanning mutagenesis of Orai1 transmembrane helices reveals numerous constitutively active CRAC channels	30
Differential modulation of GOF Orai1 cysteine mutants by STIM1	35

H134 regulates Orai1 gating through a steric mechanism	8 38
The GOF H134S Orai1 pore configuration mimics STIM1-gated channels	41
Molecular simulations show that H134S rotates TM1 and enhances pore hydration	43
Atomic packing and hydrophobicity analysis reveals distinct functional contacts between the TM1 and TM2/3 helices	48
A cluster of TM3-TM1 hydrophobic contacts is critical for STIM1-mediated Orai1 gating	51
The disease mutation S97C activates Orai1 through a hydrophobic switching mechanism	53
<u>Discussion</u>	56
<u>Future Directions</u>	62
Manipulation of Orai1 activity by cross-linking TM residues	62
Regulation of gating and Ca <sup>2+</sup> selectivity by the F187 Locus	65
Comprehensive analysis of the serine ridge	67
Functional significance of the TM2/3 ring and its interface with TM4	68
Experimental validation of the conformational changes detected in MD simulations	70
Mutational analysis of the A235 locus at the TM4-TM2/3 ring interface	73
<b>CHAPTER 4: ACTIVATION OF THE ORAI1 CHANNEL GATE IS REGULATED BY A PORE HELIX BRACE FORMED BY TM2</b>	<b>75</b>
<u>Introduction</u>	75
<u>Results</u>	75
Human mutation Orai1 L138F on TM2 opens the pore through steric clash with TM1	75
Double mutants demonstrate interaction between L138 and T92	78
Mutations at T92 phenocopy GOF L138 mutations	80
STIM1-independent inactivation of L138X and T92X channels	82

<u>Discussion</u>	9
	85
<b>CHAPTER 5: A TM1-TM3 HYDROPHOBIC INTERACTION ACTS AS GATE LATCH TO FACILITATE ORAI1 CHANNEL ACTIVATION</b>	<b>89</b>
<u>Introduction</u>	89
<u>Results</u>	89
Molecular dynamics simulations and cysteine accessibility analysis reveal water crevices behind the pore helices	89
Mutational analysis suggests a distinct functional role of M101 in the TM1-TM3 hydrophobic cluster	92
A Cd <sup>2+</sup> bridge between M101 and F99 enhances Orai1 channel activity	95
A Cd <sup>2+</sup> bridge between M101 and F187 abrogates Orai1 currents	96
<u>Discussion</u>	98
<b>MATERIALS AND METHODS</b>	<b>100</b>
<b>REFERENCES</b>	<b>106</b>

**LIST OF FIGURES AND TABLES****Figures****CHAPTER 1**

- Figure 1.1 Schematic of CRAC channel activation 15
- Figure 1.2 Architecture of Orai channels 17

**CHAPTER 2**

- Figure 2.1 Schematic of inner pore dilation gating model 20
- Figure 2.2 Differential Cd<sup>2+</sup> accessibility of G98C and F99C 24
- Figure 2.3 Mutations at F99 produce constitutively permeant Orai1 channels 25
- Figure 2.4 Membrane expression and CAD-recruitment of LOF F99I/L/V channels 26
- Figure 2.5 V102A mutation restores ion conduction in F99I/L/V channels 26

**CHAPTER 3**

- Figure 3.1 Cysteine screen of Orai1 transmembrane helices 31
- Figure 3.2 Channel properties of Orai1 GOF cysteine mutants 32
- Figure 3.3 Cysteine mutants are open independently of disulfide bonds or STIM1 binding 33
- Figure 3.4 Orai1 N-terminal mutations abolish activity of open cysteine mutants 34
- Figure 3.5 Differential modulation of GOF cysteine mutants by STIM1 36
- Figure 3.6 Activity of H134X mutants depends on the size of the introduced residue 39
- Figure 3.7 Analysis of H134X mutants in the absence and presence of STIM1 40
- Figure 3.8 Pore conformation of H134S Orai1 is similar to that of STIM1-gated channels 43
- Figure 3.9 Snapshots of MD simulations of WT and H206C dOrai channels 44

Figure 3.10 MD simulations show increased pore helix rotation and hydration in H206S/C	45
Figure 3.11 Analysis of TM1 dilation, hydration, and rotation from MD simulations	47
Figure 3.12 Atomic packing analysis of all transmembrane residues in dOrai	49
Figure 3.13 Atomic packing analysis and hydrophobicity mapping of dOrai	50
Figure 3.14 The TM3-TM1 hydrophobic cluster is essential for Orai1 gating by STIM1	52
Figure 3.15 Hydrophobic substitutions at S97 evoke constitutive channel activity	54
Figure 3.16 Ca <sup>2+</sup> selectivity of S97M and S97I mutants is not enhanced by STIM1	55
Figure 3.17 H206 and H206N may interact with TM2 backbone carbonyl	58
Figure 3.18 Summary of Orai1 gating models	60
Figure 3.19 Schematics of genetically encoded cross-linkers	63
Figure 3.20 F187 is crucial for regulating Ca <sup>2+</sup> selectivity	66
Figure 3.21 Packing density and hydrophobicity map of the TM2/3 ring to TM4 interface	69
Figure 3.22 Conformational differences between WT dOrai and the H206C open mutant	72
Figure 3.23 The small size of A235 is required for maintaining the closed and open states	74

## CHAPTER 4

Figure 4.1 Activity of L138X mutants depends on the size of the introduced side chain	76
Figure 4.2 L138-TM1 double mutants suggest that L138 interacts with T92	79
Figure 4.3 Large substitutions at T92, but not S93 or A94, cause Orai1 activation	81
Figure 4.4 GOF L138X and T92X exhibit STIM1-independent inactivation	83
Figure 4.5 Schematic of H134-L138 brace of TM1	86

**CHAPTER 5**

Figure 5.1 Water crevices behind the pore helices revealed by MD simulations.	90
Figure 5.2 Modification of residues by Ag <sup>+</sup> confirms water crevices behind the pore helix	91
Figure 5.3 Mutational analysis of M101 reveals predominantly LOF channels	93
Figure 5.4 The F99-M101-F187 locus in MD simulations of WT and H206S dOrai	94
Figure 5.5 A Cd <sup>2+</sup> bridge between F99C and M101C potentiates Orai1 current	95
Figure 5.6 A Cd <sup>2+</sup> bridge between M101C and F187C abrogates Orai1 current	97

**Tables****CHAPTER 3**

Table 3.1 Current densities and reversal potentials of GOF cysteine mutations in TMs 1-4	37
Table 3.2 Current densities and reversal potentials of H134X mutations	41
Table 3.3 Current densities and reversal potentials of S97X mutations	56

## CHAPTER 1: INTRODUCTION

This chapter is adapted from:

1. Reference (3) – Priscilla S.-W. Yeung, Megumi Yamashita, and Murali Prakriya, “Pore opening mechanism of CRAC channels.” Review article. *Cell Calcium* (2018).

### **Store-operated calcium entry**

$\text{Ca}^{2+}$  is a versatile secondary messenger ion that is essential for a variety of biological processes. Under resting conditions, intracellular  $\text{Ca}^{2+}$  concentration is tightly regulated at  $\approx 100$  nM, while extracellular  $\text{Ca}^{2+}$  concentration is four orders of magnitude higher at 1-2 mM (5). Given the importance of  $\text{Ca}^{2+}$  in eliciting physiological signals, cells use a variety of receptors, pumps, and channels to regulate where, when, and how much  $\text{Ca}^{2+}$  enters the cell (5). Of the several known mechanisms for eliciting  $\text{Ca}^{2+}$  signals in cells, store-operated calcium entry (SOCE) is one of the most widespread pathways. James W. Putney Jr. first described the idea of SOCE in 1986, noting that intracellular inositol triphosphate ( $\text{IP}_3$ ) triggers a biphasic mobilization of  $\text{Ca}^{2+}$  in rat salivary and lacrimal glands that involves an initial release of  $\text{Ca}^{2+}$  from intracellular endoplasmic reticulum (ER) stores followed by a more sustained  $\text{Ca}^{2+}$  influx from the extracellular compartment (6). He hypothesized that intracellular  $\text{Ca}^{2+}$  store depletion in these exocrine glands triggers activation of a plasma membrane  $\text{Ca}^{2+}$  influx pathway which refills depleted stores, naming it capacitative calcium entry (CCE) (6). Later studies showed that this  $\text{Ca}^{2+}$  influx pathway elevates cytosolic  $[\text{Ca}^{2+}]$  in many cells and was renamed SOCE to designate its dependence on the ER  $\text{Ca}^{2+}$  store content (7).

The best-studied SOCE channel is the “calcium release-activated calcium” (CRAC) channel, a highly  $\text{Ca}^{2+}$  selective channel with a very low unitary conductance (8). CRAC channels are widespread, perhaps universally expressed among all animal cells, and are typically activated following stimulation of G-protein coupled receptors or receptor tyrosine kinases that produce  $\text{IP}_3$  to deplete ER  $\text{Ca}^{2+}$  stores (8). Activation of the  $\text{IP}_3$  receptor on the ER membrane triggers release of  $\text{Ca}^{2+}$  from ER stores (resting  $[\text{Ca}^{2+}]$  of 400-600  $\mu\text{M}$ ) down its concentration gradient into the cytosol (5). This reduction in ER  $\text{Ca}^{2+}$  concentration drives SOCE (9) (**Figure 1.1**). Apart from refilling ER  $\text{Ca}^{2+}$  stores, the opening of CRAC channels also causes a rise in intracellular  $\text{Ca}^{2+}$  that regulates a variety of effector cell responses including gene expression, cytoskeletal reorganization, cell proliferation, exocytosis, and motility (8). Human studies have shown that loss of CRAC channel function leads to a devastating immunodeficiency along with additional symptoms of autoimmunity, ectodermal dysplasia, and muscle defects, highlighting the vital importance of CRAC channels for human health (10-12). Conversely, constitutive channel activation from gain-of-function mutations in CRAC channel proteins are linked to pathologies such as tubular aggregate myopathy and thrombocytopenia (13-16). Therefore, CRAC channels have gained traction in the recent years as a potential new drug target for these and other pathologies.

### **Molecular components of CRAC channels**

In the initial years after SOCE was discovered, the quest to identify the molecules that mediate CRAC current was on. Along the way, numerous molecules, including various members of the TRP family channels, were thought to participate in SOCE (7, 8). However, it was not until 2005 that three laboratories independently discovered stromal interaction molecules (STIM) proteins as the ER  $\text{Ca}^{2+}$  sensor through RNAi screens in *Drosophila* S2 cells and HeLa cells (17-19). The

following year, Orai was discovered through linkage analysis of a family with severe combined immunodeficiency (SCID) and genome-wide RNAi screens which found that knockdown of Orai mRNA eliminated SOCE (11, 20, 21). Soon after, it was shown that mutation of a conserved glutamate (E106) of Orai1 significantly alters the  $\text{Ca}^{2+}$  selectivity and  $\text{Ca}^{2+}$ -dependent block of the channel, providing definitive evidence for Orai as the pore-forming subunit (22). *In vitro* studies subsequently demonstrated that STIM and Orai are both necessary and sufficient for CRAC current (23), thereby securing the positions of these two proteins as the molecular components of CRAC channels.

Although there are three human homologs of Orai (Orai1, Orai2, and Orai3) and two homologs of STIM (STIM1 and STIM2) each with their own tissue expression patterns, the most extensively studied CRAC channel to date is the Orai1 channel activated by STIM1 (8, 24). Orai1 is a 301-residue plasma membrane protein with four transmembrane domains (TMs) and two cytosolic N- and C-termini that interact with intracellular proteins such as STIM1 (8, 25) (**Figure 1.1**). STIM1 makes a single pass through the ER membrane and contains several functional domains including a luminal EF-hand motif that acts as the ER  $\text{Ca}^{2+}$  sensor and two coiled-coil domains in the cytoplasmic side that comprise the CRAC-activation domain (CAD) or STIM1-

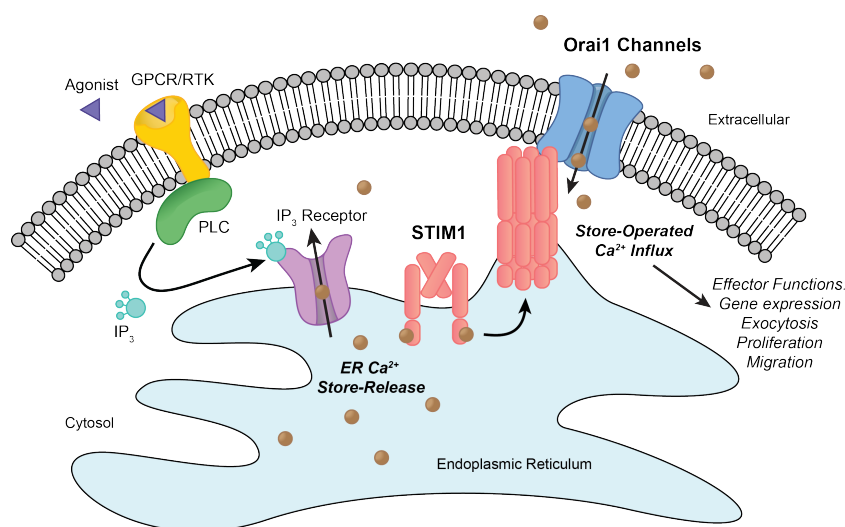


**Figure 1.1 Schematic of CRAC channel activation.** Stimulation of specific cell surface receptors including G-protein coupled receptors and receptor tyrosine kinases increases cytosolic IP<sub>3</sub>, which causes ER Ca<sup>2+</sup> store depletion. STIM1 senses the decrease ER Ca<sup>2+</sup> concentration and migrates to ER-PM junctions, where it gates Orai1 channels. The ensuing SOCE mediates numerous downstream cellular effector functions.

Orai1 activating region (SOAR) (26, 27). CAD is the catalytic region of STIM1 that binds to and activates Orai1 channels (26). Under resting conditions, Orai1 is located diffusely in the plasma membrane and STIM1 is situated at the membrane of the bulk ER (8, 28). When ER  $\text{Ca}^{2+}$  stores are depleted, dissociation of  $\text{Ca}^{2+}$  from the luminal EF-hand  $\text{Ca}^{2+}$  sensing domain of STIM1 initiates a complex molecular choreography that results in STIM1 oligomerization and migration to ER-plasma membrane junctions (28). During this activation process, CAD, which is hidden in the resting state, becomes exposed and physically binds to Orai1 to gate the channel (8, 25). This interaction causes the two previously diffusely localized proteins to accumulate into distinct puncta at ER-PM junctions to form active CRAC channels (25).

### **Permeation, selectivity, and pore architecture of Orai1 channels**

CRAC channels are characterized by two biophysical features which provide a relatively easy way to identify them in native cells: high  $\text{Ca}^{2+}$  selectivity and low unitary conductance. As measured by the proportion of current carried by  $\text{Ca}^{2+}$  in a physiological mix of  $\text{Na}^+$  and  $\text{Ca}^{2+}$  ions, CRAC channels select for  $\text{Ca}^{2+}$  over the more prevalent  $\text{Na}^+$  ions by a ratio  $> 1000$  ( $P_{\text{Ca}}/P_{\text{Na}} > 1000$ ) (9, 22, 29, 30), making them amongst the most  $\text{Ca}^{2+}$ -selective channels known. Early studies using mutational analysis and measurements of binding kinetics and voltage-dependence revealed that a ring of glutamates (E106) at the external mouth of the pore function as the selectivity filter (20-22, 31). These glutamates form a  $\text{Ca}^{2+}$  binding site to block permeation of  $\text{Na}^+$  ions through the pore ( $K_i \approx 20 \mu\text{M}$  (31-33)), analogous to the mechanism of  $\text{Ca}^{2+}$  selectivity described for voltage-gated  $\text{Ca}^{2+}$  ( $\text{Ca}_v$ ) channels (34). More recently, this explanation for the CRAC channel's high  $\text{Ca}^{2+}$  selectivity has been modified based on the observation that  $\text{Ca}^{2+}$  selectivity in Orai3 channels is controlled not only by the binding of  $\text{Ca}^{2+}$  ions to the selectivity filter (formed by E81), but also

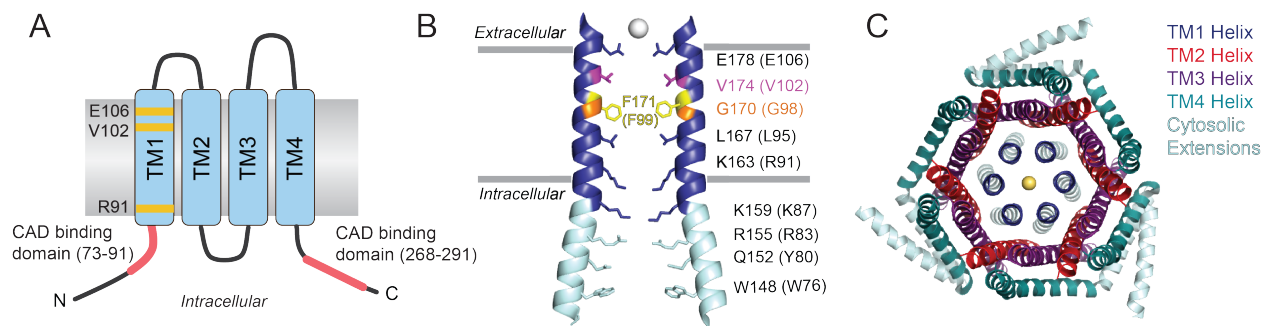


**Figure 1.2 Architecture of Orai channels.** **(A)** Topology diagram of Orai1 showing four transmembrane domains and cytosolic N- and C- termini that serve as interaction sites for STIM1. TM1 lines the channel pore with the selectivity filter formed by E106. Potential inner and outer channel gates are proposed to be near V102 and R91, respectively. Residue numbering corresponds to human Orai1. **(B)** Two diagonally facing subunits in the crystal structure of *Drosophila* Orai (PDB: 4HKR) showing predicted pore-lining TM1 residues. dOrai residue numbering is indicated with equivalent hOrai1 residues shown in parentheses. **(C)** Top-down view of the complete crystal structure of dOrai. Each channel is formed by six Orai proteins arranged in concentric rings surrounding the narrow pore flanked by TM1.

by the overall rates of ion entry and exit from the selectivity filter, with slower ion flux rates yielding higher selectivity (35). This latter feature likely explains why CRAC channels exhibit comparable levels of  $\text{Ca}^{2+}$  selectivity as  $\text{Ca}_v$  channels despite 20-fold weaker  $\text{Ca}^{2+}$  binding in the pore ( $K_i < 1 \mu\text{M}$  in  $\text{Ca}_v$  channels (34) vs.  $20 \mu\text{M}$  in CRAC channels (31-33)). In effect, a slow ionic flux rate in CRAC channels essentially eliminates the need for tight  $\text{Ca}^{2+}$  binding to achieve high  $\text{Ca}^{2+}$  selectivity.

Interestingly, studies in constitutively active Orai1 channels indicate that the  $\text{Ca}^{2+}$  selectivity of CRAC channels is strongly regulated by STIM1 binding, suggesting that the selectivity of the CRAC channel is not a fixed property of the open state structure, but a dynamic property coupled to channel gating (36). The details of how this occurs remain to be formally determined. But as discussed below, one possibility is that  $\text{Ca}^{2+}$  binding to the selectivity filter is altered by the conformational motions triggered by STIM1 binding (2, 36). The second functional characteristic of CRAC channels, their low unitary conductance, is less well understood. Estimates from analysis of the whole-cell current noise indicate that the unitary conductance is only 10-30

fS in 2-110 mM  $\text{Ca}^{2+}$  containing solutions (32, 35, 37), which suggests the pore contains significant energy barriers for ion conduction in the active state.

An important breakthrough in our understanding of the molecular basis of ion conduction in CRAC channels came from identification of the pore-lining residues (38, 39). In one approach, the substituted cysteine accessibility method (SCAM) was used to examine the extent of current inhibition after thiol-reactive reagents were applied to the extracellular side of Orai1 channels bearing cysteine mutations (38). In a second approach, the fraction of inter-subunit disulfide cross-linking of Orai1 cysteine mutants was quantified based on the prediction that cysteine residues introduced at pore-lining positions should be able to form disulfide bonds across the pore upon protein oxidation (39). The results of these two studies indicated that residues in TM1 flank the pore and ruled out a contribution for TM3 and, specifically, E190, a residue in TM3 that was previously thought to regulate  $\text{Ca}^{2+}$  selectivity (20, 22). In the TM1 domain, the key pore-lining residues found from these studies included E106, V102, G98, L95 and R91 (**Figure 1B**). The SCAM study used  $\text{Cd}^{2+}$  ions to form metal ion bridges between introduced cysteine residues across the pore (38). Because the length of  $\text{Cd}^{2+}$ -S bridges is short ( $\sim 2.5$  Å) (40), the strong reactivity to  $\text{Cd}^{2+}$  at several pore-lining residues indicated that TM1 helices are close to one another and therefore line a narrow pore, a feature that has been proposed to account for the CRAC channel's low permeability to large cations ( $>3.8$  Å) and its low unitary conductance (30). Moreover, differences in the accessibility of probes of different sizes showed that the pore narrows sharply at the base of the outer pore vestibule, near E106 (38). These results provided the first step toward building a structural model of the open pore.

## Structure of Orai channels

Although there currently is no available structure of human Orai1, the crystal structure of the homologous *Drosophila melanogaster* Orai (dOrai) revealed hexameric channels with six-fold symmetry in the pore and three-fold symmetry at the outer C-terminal regions (41). Recent functional studies using engineered concatemers have solidified the notion that human Orai1 channels are composed of a trimer of dimers (42, 43). Within the channel, the four transmembrane domains (TMs) of each dOrai subunit are arranged in concentric rings, with TMs 2-4 surrounding a central pore lined by TM1 (41). The structure of a narrow central pore flanked by TM1 helices is consistent with previous studies probing the functional architecture of the pore using electrophysiological and biochemical methods (38, 39). Among the many interesting features of the dOrai channel complex revealed by this structure, one unanticipated finding was that the N-terminus, which was previously thought to lack a secondary structure, instead forms a cytosolic helix continuous with the TM1 pore (**Figure 1B**). While the crystal structure has provided a detailed view of the closed Orai channel, the specific structural changes that lead to gating are unknown. In addition, the molecular mechanisms by which most of the disease-causing loss-of-function (LOF) and gain-of-function (GOF) mutations disrupt CRAC channel function remain unclear (10, 12-16), presenting a significant hurdle to current efforts at mechanism-based drug design targeting CRAC channels.

## CHAPTER 2: PORE OPENING MECHANISM OF ORAI1 CHANNELS

This chapter is adapted from:

1. Reference (2) – Megumi Yamashita, Priscilla S.-W. Yeung, Christopher E. Ing, Beth A. McNally, Régis Pomès and Murali Prakriya, “STIM1 activates CRAC channels through rotation of the pore helix to open a hydrophobic gate.” *Nature Communications* (2017).
2. Reference (3) – Priscilla S.-W. Yeung, Megumi Yamashita, and Murali Prakriya, “Pore opening mechanism of CRAC channels.” Review article. *Cell Calcium* (2018).

### Introduction

The identification of pore-lining residues provided the structural and functional framework to next address the pore opening mechanism of CRAC channels. Where is the location of the channel gate and what is its nature? And what conformational changes in the pore underlie the activation of the gate? Two models have been proposed.

One model has postulated that the gate is in the inner pore (44, 45) (**Figure 2.1**). The first study to propose this viewpoint is based on the loss-of-function phenotype of R91W human mutation (11) and the ability of R91C to be cross-linked across the pore in the STIM1-activated channel (44). R91 was suggested to constitute at least a part of the gate, with G98 functioning as a hinge to kink the lower portion

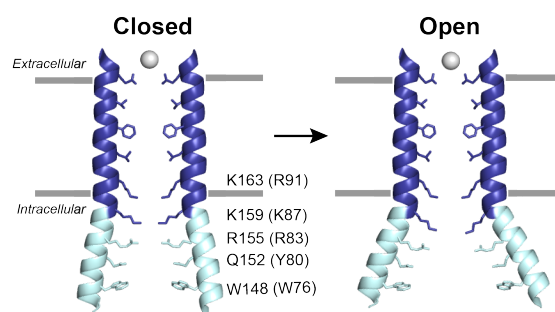


**Figure 2.1 Schematic of the inner pore dilation gating model based on the dOrai crystal structure.** In this model, STIM1 binding to Orai1 causes the inner pore formed by the cytoplasmic N-terminal extension helix to widen, relieving steric and electro- static barriers formed by the basic residues (R91, K87, R83) to allow ion conduction. The left and right panels represent the closed and open states, respectively. Pore lining residues in the inner pore correspond to those in dOrai with hOrai1 residue numbering shown in parentheses. Figure adapted from reference (3).

of the TM1 segment and induce dilation in the region encompassing R91 to open the gate (44) (**Figure 2**). Moreover, based on the presence of anions detected in the crystal structure bound to the basic residues (K163, K159, R155) in the cytoplasmic portion of the N-terminus that is contiguous with TM1 (the TM1 extension helix), the crystal structure study went further and suggested that these positively charged residues may function as a part of an inner gate to block ion conduction either via steric occlusion or electrostatic repulsion (41). Gating was hypothesized to occur through widening of the inner pore to release the anions or decrease the electrostatic barrier (41, 44) (**Figure 2.1**). Further, a recent study used Western blotting to demonstrate a difference between the closed WT and H134A open mutant in the propensity for inter-subunit cross-linking across the pore at R91 (45). Based on this result, along with molecular dynamics (MD) simulations showing hydrogen bonding between R91 and S90 which stabilize R91 side chains away from the pore in the H134A mutant, this group concluded that R91 forms part of the gate (45). However, there have been no functional studies determining whether the N-terminal extension constitutes part of the conduction pathway, and the idea of an inner pore gate has been challenged by recent studies showing that a channel with a truncated N-terminal helix still retains a barrier to ion conduction (46), presumably a gate that lies elsewhere in the channel pore.

In an alternative model has argued that the channel gate is located near the outer pore at V102 (36, 46), a pore-lining residue that is one  $\alpha$ -helical turn below E106, the selectivity filter (**Figure 1.2B**). An important clue for a role of this residue in Orai1 gating came from attempts to localize the channel gate from analysis of state-dependent blockade of a cysteine introduced at G98, located near the midpoint of the membrane. 2-Aminoethyl methanethiosulfonate (MTSEA), a thiol reagent that covalently modifies the side-chains of cysteine residues, blocked G98C in open, but not closed Orai1 channels when administered externally (36). This result indicated that there

exists a barrier to ion flow located extracellular to G98 in a region which includes the pore residue V102 (**Figure 1.2B**). Subsequent mutational analysis revealed that substitutions of V102 to more polar amino acids yield constitutively permeant channels that allow ion conduction to occur in the absence of STIM1 (36). Further study of these mutations strongly pointed to a model wherein V102 likely presents a hydrophobic free energy barrier to prevent water and ions from entering the pore in the closed channel state. These ideas received support from MD simulations, which showed that the V102A mutant reduces the energetic cost of water entering the pore, especially in the hydrophobic region encompassing V102 and F99, potentially explaining its constitutive permeation phenotype (2, 47). In addition, lanthanide resonance energy transfer experiments using purified Orai1 in liposomes found that STIM1 binding at the cytosolic surface of Orai1 elicits a gating movement at the outer mouth of the pore in the region encompassing V102 (46). These investigators also found that a mutant lacking the N-terminal cytosolic helix, which presumably should also lack an inner gate, remained closed, yet could be opened by introducing a V102C mutation, leading them to conclude that a barrier to ion flux exists outside the inner pore, most likely in the hydrophobic zone (46). Collectively, the results from differing approaches converged towards a model wherein the hydrophobic V102 presents a free energy barrier that is substantive enough to occlude ion conduction in closed channels.

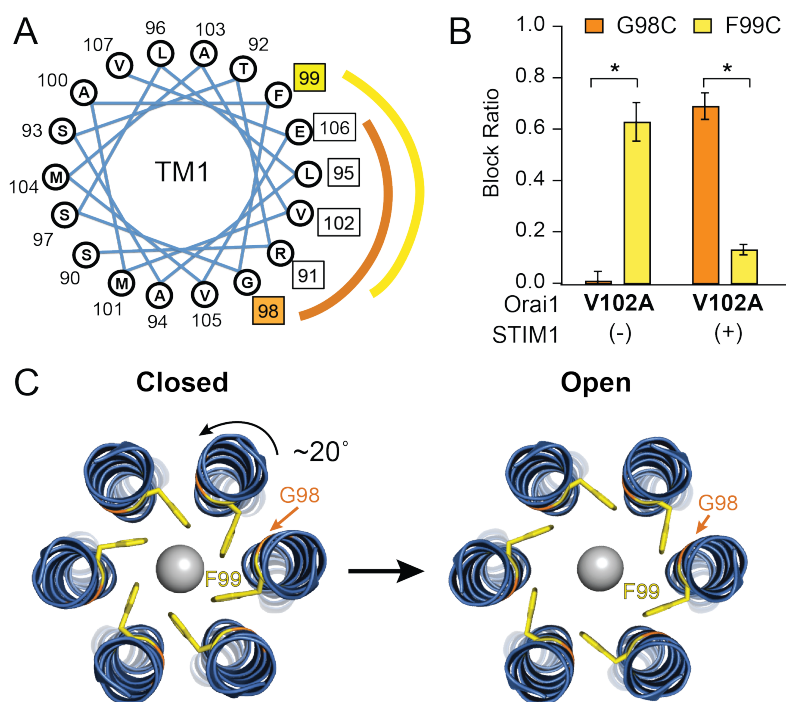
Although the studies described above imply that V102 functions as a hydrophobic barrier, exactly how this barrier is relieved upon channel opening was not explained. Ion sizing experiments in the constitutively conducting V102C mutant showed that STIM1 binding causes the Orai1 channel pore to narrow (36), which suggests that the gating mechanism in CRAC channels does not involve simple pore dilation to permit ion flow. Paradoxically, a direct examination of the conformational change during gating using the accessibility of pore-applied

thiol reagents revealed that access of the reagents  $\text{Cd}^{2+}$  and  $\text{Ag}^+$  to V102C is not altered by STIM1 binding (2), indicating that V102C remains pore-facing in both the resting and activated conformations. This surprising finding implies that although V102 likely forms part of the hydrophobic barrier to stabilize closed channels, it alone does not constitute the channel gate given its constant exposure into the pore.

## **Results**

What then is the identity of the gate and how does it dynamically regulate ion conduction? One clue came from the subtle distinction between the pore-lining residues in the hydrophobic region identified in the STIM1-activated channel by SCAM (38) versus those observed in the closed dOrai structure (41), which showed G98 and F99 respectively as the pore-lining residues (**Figure 2.2A**). This difference led us to hypothesize that STIM1 binding evokes a conformational change that alters the accessibility of these residues upon pore opening, thereby exposing G98 towards the pore and concealing F99 away from it. Indeed, analysis of the accessibility of cysteine mutants of key pore residues in the V102A background (to confer constitutive ion conduction in the absence of STIM1) indicated that F99C is blocked strongly by  $\text{Cd}^{2+}$ , but this block decreases dramatically when STIM1 is added (2) (**Figure 2.2B**). Conversely, the G98C/V102A current is weakly inhibited by  $\text{Cd}^{2+}$ , but the addition of STIM1 greatly increases its sensitivity to  $\text{Cd}^{2+}$  blockade (2) (**Figure 2.2B**). These functional results imply that STIM1 induces a modest ( $\sim 20^\circ$ ) counter-clockwise rotation of the pore helix that moves F99 away from the pore axis but which brings G98 towards a more pore-facing orientation (**Figure 2.2C**).

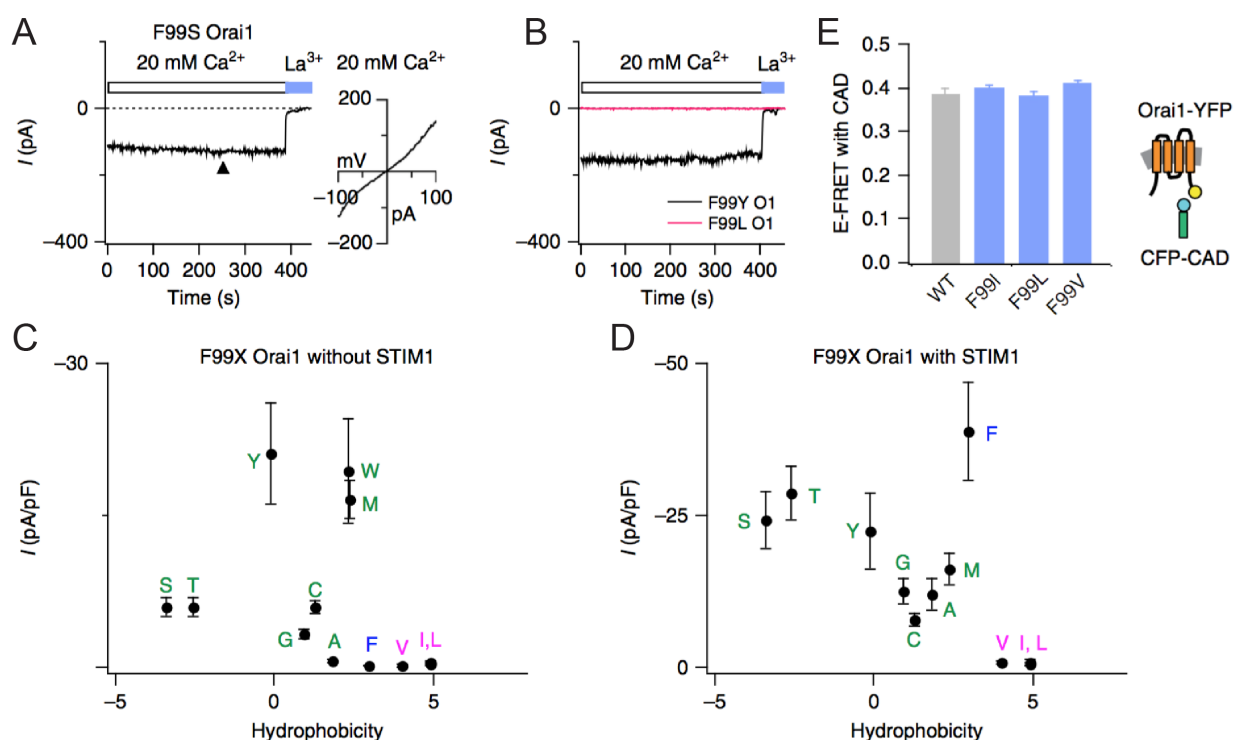
The finding that the bulky non-polar F99 rotates away from the pore axis following STIM1 binding raises the strong possibility that this residue may be the channel gate. In fact, examination



**Figure 2.2 Differential  $\text{Cd}^{2+}$  accessibility at G98C and F99C supports the pore helix rotation model of Orai1 gating.** (A) Top-down helical wheel representation of TM1, indicating pore-lining residues of hOrai1 identified in the open channel by SCAM (lined in orange) and those identified through the crystal structure of the closed dOrai channel (lined in yellow). (B) Addition of STIM1 decreases  $\text{Cd}^{2+}$  block in F99C/V102A channels and increases block in G98C/V102A channels, suggesting that the F99 residues move away from the pore axis while G98 becomes pore facing during gating. (Data collected by Megumi Yamashita.) (C) Schematic of the pore helix rotation model. Based on its orientation towards the pore in the closed state shown in the crystal structure, F99 is not expected to permit ion flow in this configuration. In pore helix rotation model, gating occurs through a slight rotation of TM1, which moves F99 away from the pore axis. This is predicted to decrease the free energy barrier in the V102/F99 hydrophobic region to allow ion permeation.

of the dOrai crystal structure suggests that the F99 side-chains as oriented in this structure, would not allow the passage of ions in this presumably closed channel state (**Figure 2.2C**). In line with this possibility, substitutions of F99 to more polar residues (Tyr, Ser, Thr, Cys, Met) yielded leaky channels with poor  $\text{Ca}^{2+}$  selectivity in the absence of STIM1 (**Figure 2.3A-C**) (2). Channels with substitutions to Ile, Leu, or Val, however, remained closed (**Figure 2.3C**) (2). This observation is consistent with a scenario wherein F99 functions as an energy barrier for water and ion occupancy, with manipulations that lower hydrophobicity at this position evoking leaky channels. Surprisingly, the Ile, Leu, and Val mutants remain closed even in the presence of STIM1 (2) (**Figure 2.3D**).

The LOF phenotype of these mutants were not due to defects in membrane expression nor CAD-recruitment (2) (**Figures 2.3E, 2.4**). Further, F99I/L/V channels can be opened by decreasing the hydrophobicity at the upstream Val through a V102A substitution (but not V102L) (2), implying that increasing hydrophobicity of this region produces an insurmountable energetic barrier for ion conduction even when STIM1 is bound to the channels, thereby stabilizing the closed state (**Figure 2.5**). Overall, these functional results signify that the energy barrier at F99 is finely tuned such that



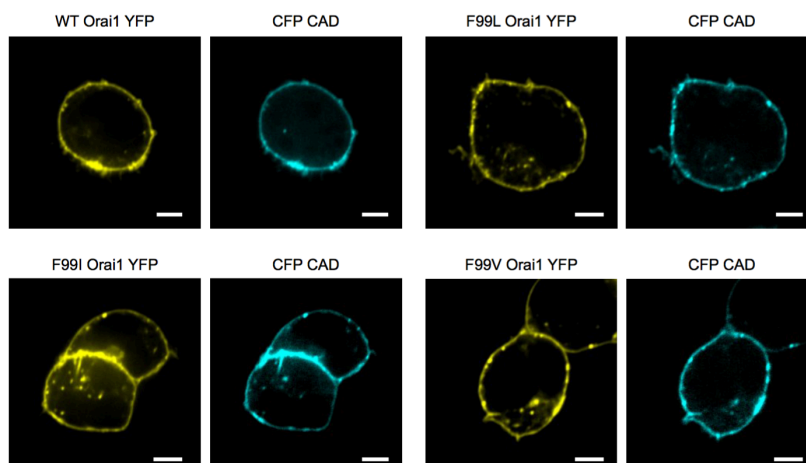


**Figure 2.4 Expression and CAD-recruitment of LOF F99I/L/V channels.** Confocal images showing Orail expression of various F99X mutants and co-localization of Orail and CAD at the plasma membrane. The indicated Orail-YFP constructs were expressed in HEK293 cells together with CFP-CAD. Scale bars: 5  $\mu\text{m}$ .

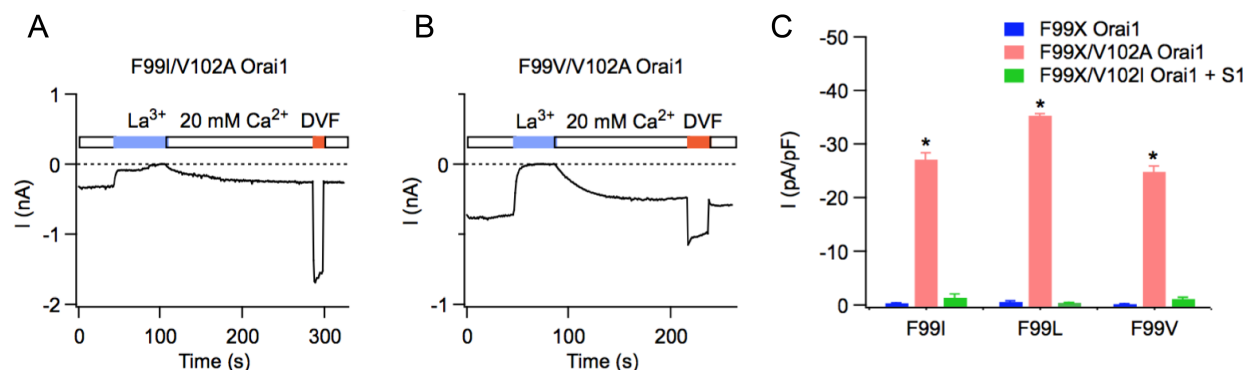


**Figure 2.5 Introduction of a V102A mutation restores ion conduction in the non-conducting F99I/L/V channels.** (A-B) Time course of the indicated Orail mutants following whole-cell break-in (at time zero). (C) Summary of the current densities of the indicated F99X mutants in the absence or presence of the V102A mutation. In contrast to the gain-of-function effect caused by V102A on the closed F99I/L/V mutants, introduction of a V102I mutation keeps these mutants non-functional even in the presence of STIM1. (Data collected in collaboration with Megumi Yamashita.) N=4-5 cells per condition. \*:  $p < 0.001$ . Values are mean  $\pm$  SEM.

mutations that decrease hydrophobicity lead to a leaky gate whereas increases in hydrophobicity abrogate STIM1-mediated gating.

Molecular dynamics (MD) simulations using models constructed from the crystal structure of the *Drosophila* Orail channel provide further support for these conclusions. The MD simulations showed a striking increase in pore hydration compared to WT Orail in the constitutively conducting

F171Y mutation (hOrai1 F99Y GOF mutation) [51]. By contrast, the more hydrophobic F171V mutation (hOrai1 F99V LOF mutation) lowered water occupancy in the pore. These opposing effects of the F171V and F171Y on water occupancy agree with the experimental findings of gain- and loss-of-function effects in the equivalent human Orai1 mutants and support the idea that two rings of closely spaced hydrophobic pore-lining residues (V102 and F99) contribute to a desolvation barrier that prevents ion conduction in closed channels.

## **Discussion**

In sum, the results of this study lead to a model in which STIM1-mediated opening of Orai1 channel pore occurs through a mechanism involving rotation of the pore helix, leading to displacement of the F99 side-chains away from the pore axis to increase water occupancy and allow ion flow through the hydrophobic barrier formed by V102 and F99 (**Figure 1.2B**). Such a mechanism potentially also explains why STIM1 binding alters the selectivity of the constitutively active V102X and F99X mutant channels, as rotation of the outer pore during gating would naturally be expected to reorient the E106 side chains of the selectivity filter thereby altering  $\text{Ca}^{2+}$  binding. The energetic cost of reorienting TM1, which would be expected to modify interactions of the pore helix with other parts of the channel, is unknown. One possibility is that water molecules around the pore helices could lower the free energy required for rotating the helices during channel opening (see Chapter 5). The hydrophobic gating mechanism that we propose for Orai1 is similar to the activation mechanisms of several other ion channel families, including the nicotinic acetylcholine receptor (48), the magnesium channel CorA (49), and the mechanosensitive channel MscL (50), which also involve a ring of hydrophobic residues forming an energetic barrier in the pore.

### CHAPTER 3: MAPPING THE FUNCTIONAL ANATOMY OF ORAI1 TRANSMEMBRANE DOMAINS FOR CRAC CHANNEL GATING

This chapter is adapted from:

1. Priscilla S.-W. Yeung, Megumi Yamashita, Christopher E. Ing, Régis Pomès, Douglas M. Freymann and Murali Prakriya, “Mapping the functional anatomy of Orai1 transmembrane domains for CRAC channel gating.” *Proceedings of the National Academy of Sciences* (2018).

#### **Introduction**

The results presented in Chapter 2 indicate that the channel gate is formed, at least in part, by the combination of two hydrophobic pore residues, F99 and V102, that regulate the closed-open transition. STIM1 binding is proposed to open this gate by inducing a modest rotation of the pore helix to move the bulky F99 side-chains away from the pore axis to lower the energy barrier for ion conduction (2). A major unresolved question in this process is the molecular mechanism by which the STIM1 gating signal is communicated to the Orai1 pore.

Early studies using purified Orai1 fragments have suggested that STIM1 directly binds to the Orai1 C-terminus and more weakly to the N-terminus, but not to the intracellular TM2-3 loop (23, 26, 51-53). Truncations or mutations in the C-terminal STIM1-binding region completely abolish the ability of STIM1 to interact with Orai1 (51, 52, 54-56), while disruptions in the putative N-terminal binding site reduce STIM1-Orai1 binding and abrogate channel function (51, 52, 55-57). These and other findings led to the development of a two-step gating model in which STIM1 first interacts with a high affinity site at the Orai1 C-terminus followed by a lower affinity interaction with the N-terminus (51-53, 55-57). Based on loss-of-function mutations in the N-terminus and its proximity to the pore-forming TM1 helix, it was thought that gating is

predominantly controlled by this N-terminal interaction site (51, 56, 57). However, several recent studies have shown that the process is likely more complex and that both the N- and C-termini contribute to STIM1 binding and gating (52, 53, 55). Along the other end of the spectrum, yet others have proposed that STIM1 binding to the C-terminus allosterically drives channel activation and that the Orai1 N-terminus does not bind to STIM1 at all (58).

Although not considered in most early studies, there is increasing evidence from human genetic disease association studies that the transmembrane domains of Orai1 may be critically involved in this process. In particular, several reports have described patients with tubular aggregate myopathy, thrombocytopenia, and congenital miosis caused by gain-of-function (GOF) Orai1 mutations located within the TM domains (13-16). In addition, recent structure-function analysis of several gain-of-function mutations including that of a putative “hinge” at the base of TM4 (58), a Pro residue in TM4 (55), and several residues cataloged in a cancer genomics database (45), provide more direct support for involvement of the non-pore lining TMs in Orai1 gating. These findings suggest that as seen in many ligand-gated channels (59), local conformational changes at the agonist binding site (55, 58) are allosterically relayed to the distally located channel gate in the pore (2, 36) through an unknown pathway.

The discovery of pathological human mutations, along with evidence from the structure-function studies described above, prompted us to examine the structural basis of how the non-pore lining TMs regulate channel activation. Using scanning mutagenesis, state-dependent accessibility analysis, molecular dynamics simulations, and atomic packing analysis, we generated a functional map of key interactions between the transmembrane domains of Orai1 that are critical for conveying the gating signal to the CRAC channel pore.

## **Results**

### **Scanning mutagenesis of Orai1 transmembrane helices reveals numerous constitutively active CRAC channels**

Several recent studies have described gain-of-function (GOF) missense Orai1 mutations in TMs 2-4, with some linked to tubular aggregate myopathy with additional symptoms including thrombocytopenia and miosis (13-16). The identification of GOF mutations in the non-pore lining segments suggests that these domains of Orai1 may play a greater role in channel activation than previously appreciated. To begin addressing this question, we started our study with an unbiased mutagenesis screen to identify residues in the TMs that could regulate Orai1 channel activation. There are 130 transmembrane residues in the human Orai1 sequence based on comparison to the crystal structure of highly homologous *Drosophila melanogaster* Orai (dOrai) protein (PDB: 4HKR (41)), with three endogenous Cys residues (C126, C145, C196) in TM2 and TM3. We sequentially mutated each of the non-Cys Orai1 transmembrane residues to generate 127 DNA constructs each containing a single Cys mutation. These mutants were transfected into HEK293 cells in the absence of STIM1 and tested by whole-cell mode patch clamping. Cys substitutions were used for this analysis because as a moderately hydrophobic residue, it is generally well-tolerated in TMs (60). Further, this approach allowed us to take advantage of some previously generated TM1 and TM3 Cys mutants (38) for this work.

To our surprise, this screen revealed numerous constitutively active GOF mutations in Orai1 with varying levels of current density and ion selectivity (**Figures 3.1 and 3.2, Table 3.1**). When mapped onto the crystal structure of dOrai (41) (**Figure 3.1B**), the mutations showed broad distribution in the membrane spanning regions of all four TM domains, including four in the TM4 segment that is farthest from the pore at a distance of 20-25 Å away. Many GOF mutants exhibited

current-voltage (I-V) relationships resembling that of WT Orai1 channels activated by STIM1 ( $V_{rev} > 35$  mV) (Figures 3.2 and Table 3.2). These included two loci which have been linked to tubular aggregate myopathy with congenital miosis – S97C on the non-pore lining face of TM1

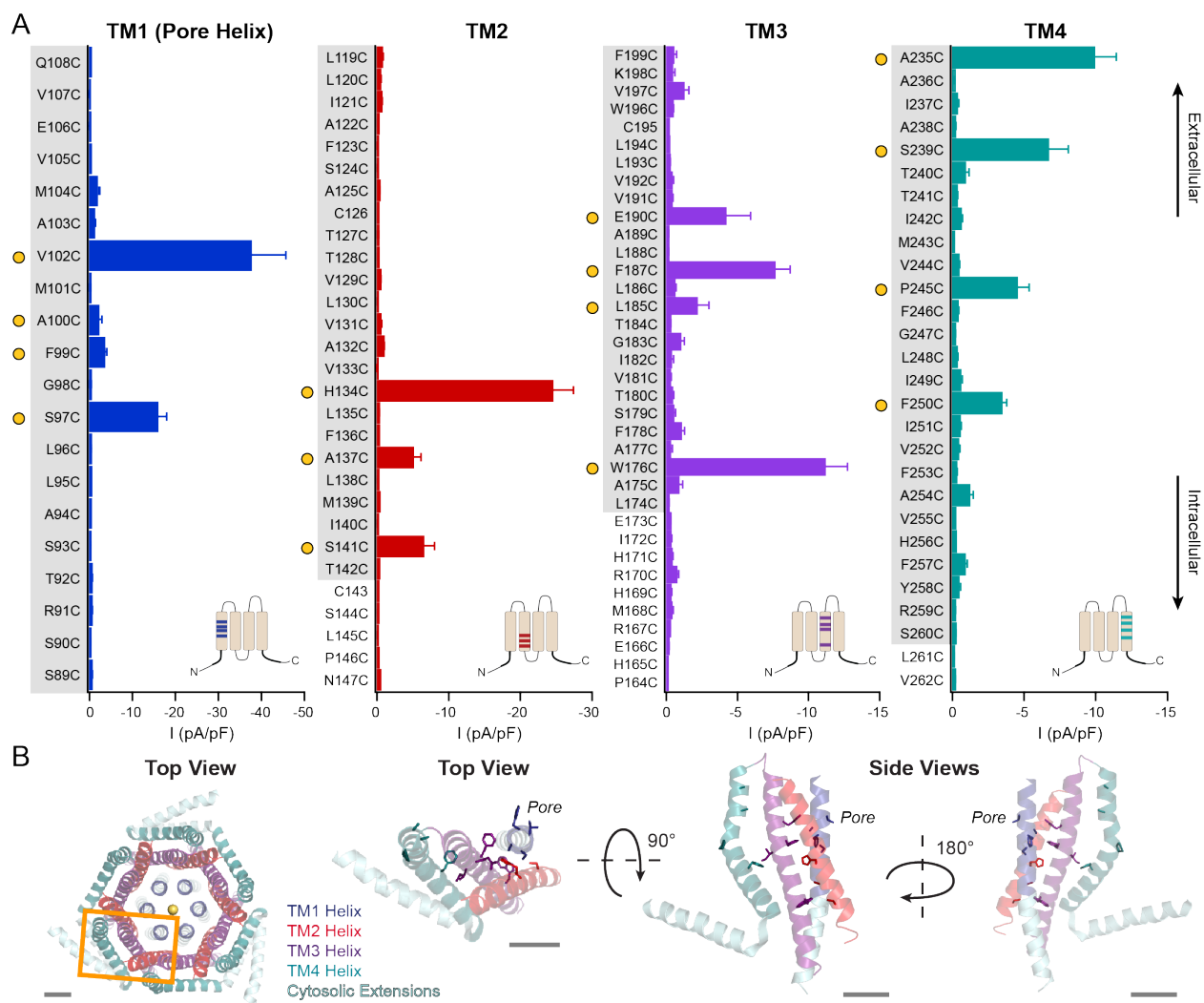


**Figure 3.1 A cysteine screen of Orai1 transmembrane helices reveals constitutively active mutants in all four TMs. (A)** Current densities of the indicated Orai1 cysteine mutants in the absence of STIM1. Current densities of WT Orai1 without and with STIM1 are  $-0.2 \pm 0.01$  pA/pF and  $-48 \pm 8$  pA/pF respectively. Constitutively active mutants (defined as  $>2$  pA/pF) are marked with filled yellow circles. Grey shaded areas on the labels indicate the boundaries of the membrane as represented in the dOrai crystal structure. Insets depict the approximate positions of the mutations on a topology diagram of Orai1. N = 4-16 cells. Values are mean  $\pm$  S.E.M. **(B)** Top down view of the crystal structure of dOrai with one subunit outlined in an orange box. A top down view and two side views of one dOrai subunit are also shown. TMs 1-4 are colored in blue, red, purple and teal respectively, with the positions of constitutively open cysteine mutants represented as sticks. Scale bars = 10 Å. (Data collected in collaboration with Megumi Yamashita.)

(15) and P245C in TM4 (55) – as well as H134C in TM2, F187C in TM3, and A235C in TM4 (**Figures 3.1 and 3.2, Table 3.1**). Others, such as W176C (61) and E190C on TM3, however, displayed substantial outward currents at positive potentials (**Figure 3.2D-E**). The wide variation in current amplitude and ion selectivity among the GOF mutants suggests that they stabilize Orai1 in different open conformations.

Because Orai1 has three endogenous Cys residues at positions 126, 143, and 195, it is possible that some of the GOF phenotypes arise from disulfide bond formation with the introduced Cys residues. However, replacing the native cysteines with serines (Cys3S construct) did not affect

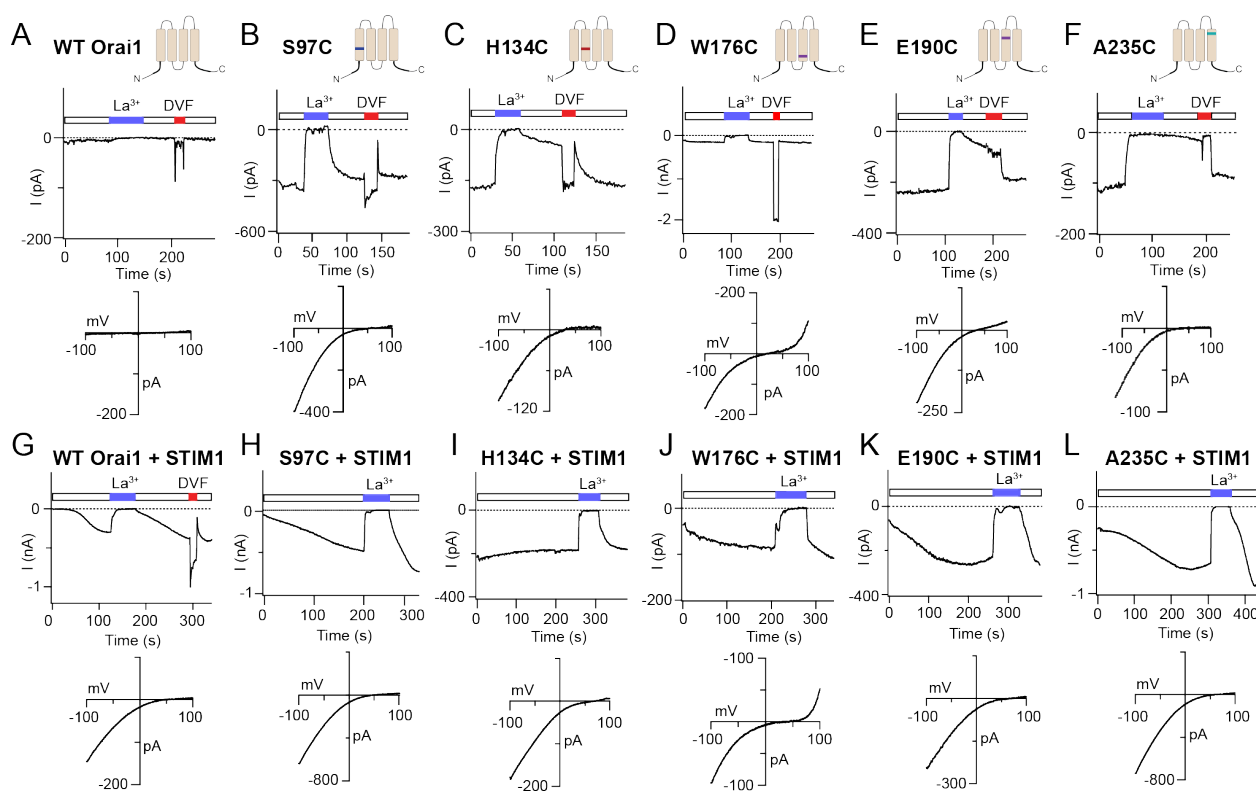


**Figure 3.2 Channel properties of Orai1 GOF cysteine mutants.** (A-F) Constitutive activity of the indicated Orai1 variants. The top traces show the time course of current in the absence of STIM1 following whole-cell break-in ( $t=0$ ). The lower graphs depict the current-voltage relationship (I-V) of the indicated mutants measured in 20 mM extracellular  $\text{Ca}^{2+}$  solution. (G-L) Store-operated activation of WT and mutant Orai1 channels in STIM1 co-expressing cells. In contrast to all other mutants, H134C does not show additional current increase following whole-cell break-in. The lower graphs show the I-V relations of the different mutants. Note that STIM1 co-expression shifts the reversal potential of the mutant channels in all cases (see also Table S1).

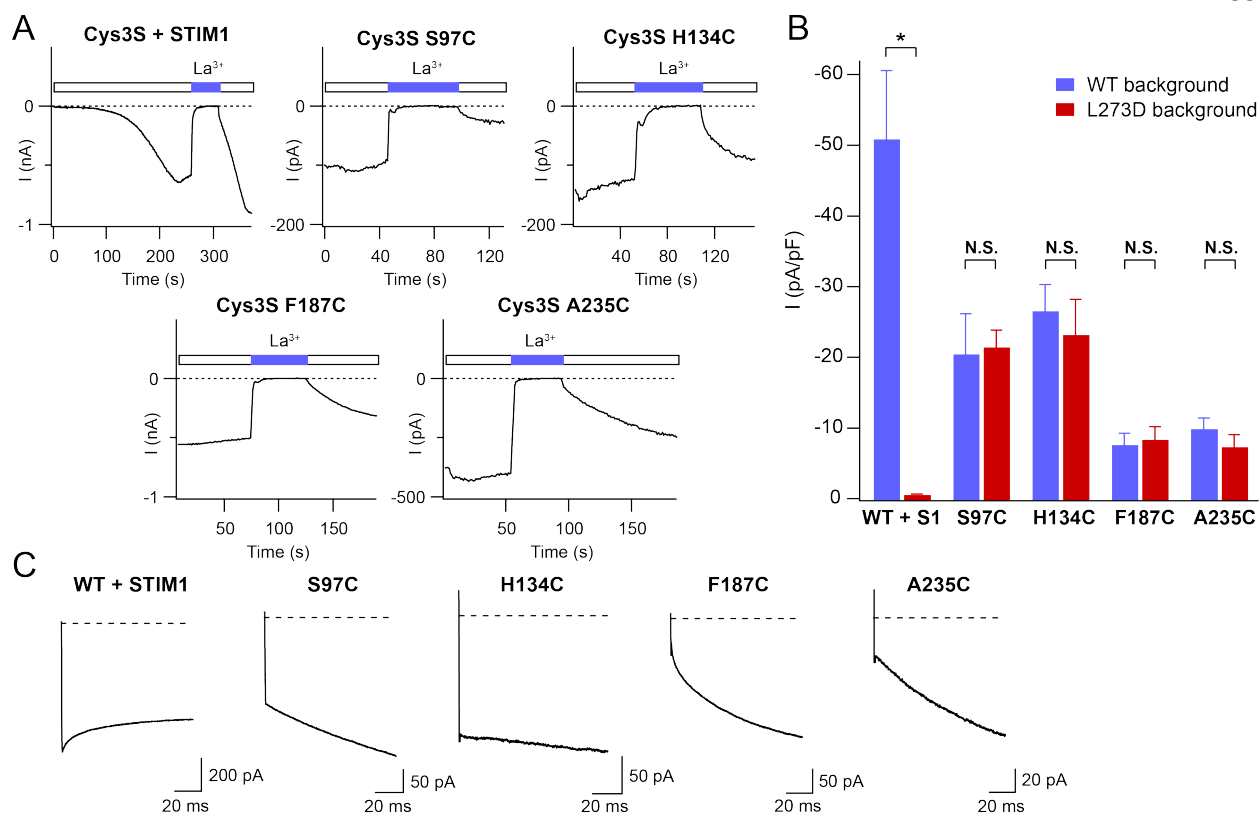


**Figure 3.3 GOF phenotypes of constitutively open cysteine mutants are independent of local disulfide bond formation or enhanced STIM1 binding. (A)** Cysteine mutants S97C, H134C, F187C, and A235C remain constitutively active in the Cys3S background in which the three endogenous Orai1 cysteine residues have been replaced by serines. **(B)** Current amplitudes of GOF cysteine mutants are unaffected in the L273D background which abrogates STIM1 binding to Orai1.  $N = 4-7$  cells. Values are mean  $\pm$  S.E.M. \* $P < 0.05$ . **(C)** Unlike WT Orai1 activated by STIM1, GOF cysteine mutants do not exhibit  $\text{Ca}^{2+}$ -dependent fast inactivation, consistent with the ability for these mutants to conduct current independently of STIM1 binding.

the GOF phenotype of the tested open mutants (**Figure 3.3A**), indicating that the constitutive activity is not dependent on the endogenous cysteines. Further, the open channel phenotype does not arise from enhanced binding to the endogenous pool of STIM1, because the introduction of an additional L273D mutation, which abrogates STIM1 binding (62), did not affect the constitutive activity of the tested mutants (**Figure 3.3B**). Finally, consistent with the well-established requirement of STIM1 for  $\text{Ca}^{2+}$ -dependent fast inactivation (CDI) in Orai1 (63-65), the constitutively open cysteine mutants did not exhibit CDI (**Figure 3.3C**). Taken together, these results indicate that the cysteine mutations described above activate Orai1 channels independently

of STIM1 binding, likely by disrupting endogenous interactions between amino acids that are involved keeping the channel closed.

Interestingly, adding a K85E mutation (52, 57, 66), which has been shown to be essential for Orai1 channel gating, or deleting the N-terminus of Orai1 (Orai1  $\Delta$ 2-85), which harbors a putative CAD binding site (23, 26, 52), eliminated the constitutive activity of the GOF mutations (Figure 3.4A). The loss of function of these mutants was not due to defects in channel expression or plasma membrane localization (Figure 3.4B). These findings are in line with recent studies that

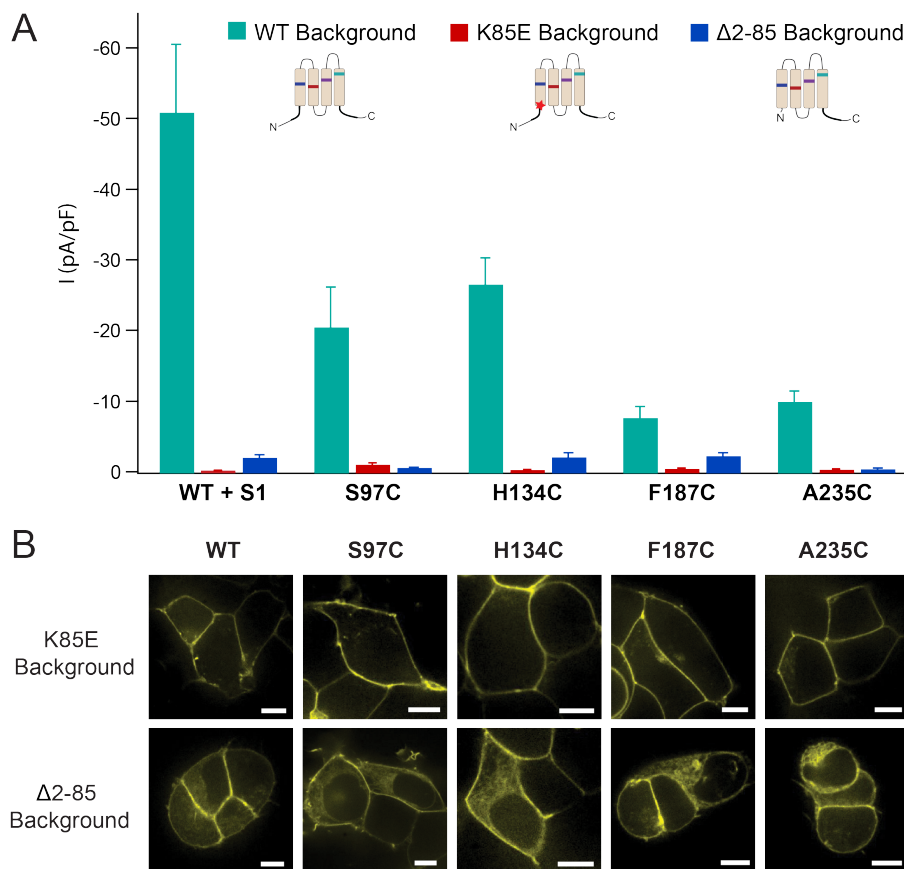


**Figure 3.4 Mutations of the Orai1 N-terminus abolish activity of the constitutively open TM1-4 mutants. (A)** Current densities of constitutively open cysteine mutants S97C, H134C, F187C, and A235C in WT, K85E, or N-terminal truncation  $\Delta$ 2-85 backgrounds. K85E and  $\Delta$ 2-85 both abrogate the activity of these GOF channels. **(B)** Confocal images of WT Orai1-YFP and cysteine mutants S97C, H134C, F187C, and A235C in the K85E and  $\Delta$ 2-85 backgrounds. K85E Orai1-YFP constructs are well expressed in the membrane. Some fluorescence is seen in a cytosolic compartment in the  $\Delta$ 2-85 channels, but good expression is still retained in the plasma membrane. Scale bar = 10  $\mu$ m.

have also observed that K85E and other N-terminal mutations abolish the constitutive activity of some GOF Orai1 mutations (58, 67) and suggest that the Orai1 N-terminus, and specifically, K85, are essential for maintaining channel function independently of interactions with STIM1.

### **Differential modulation of GOF Orai1 cysteine mutants by STIM1**

Although constitutively active in the absence of STIM1 co-expression, the majority of the open mutants described above displayed increases in current amplitude and became significantly more  $\text{Ca}^{2+}$ -selective when over-expressed with STIM1 (**Figure 3.2**). As a consequence, the macroscopic mutant channel properties in the presence of STIM1 including I-V relationship, reversal potentials, and CDI were in most cases indistinguishable from those of WT Orai1 channels activated by STIM1 (**Figure 3.2 and Table 3.1**). For example, E190C, which was only moderately  $\text{Ca}^{2+}$  selective in the absence of STIM1 (**Figure 3.2E and Table 3.1**), became significantly more  $\text{Ca}^{2+}$  selective when co-expressed with STIM1 (**Figure 3.2K**). Even W176C, which displayed an outwardly rectifying I-V relationship at positive potentials similar to 2-APB-gated Orai3 currents (35, 68, 69) (**Figure 3.2D**), showed a robust rightward shift in  $V_{\text{rev}}$  in the presence of STIM1 (**Figure 3.2J**). This modulation of ion selectivity is consistent with previous findings indicating that STIM1 not only activates Orai1 channels, but also concomitantly boosts its  $\text{Ca}^{2+}$  selectivity in a dose-dependent manner (36). Overall, these findings demonstrate that the constitutively open mutant channels are not maximally active but instead adopt one or more open states that can be further activated by STIM1.

Modulation of channel activity and  $\text{Ca}^{2+}$  selectivity by STIM1, however, varied among the different mutants. Plots of the increase in current, or  $V_{\text{rev}}$ , showed an inverse relationship with the amount of constitutive activity (**Figure 3.5**), suggesting that the efficacy of STIM1 to further

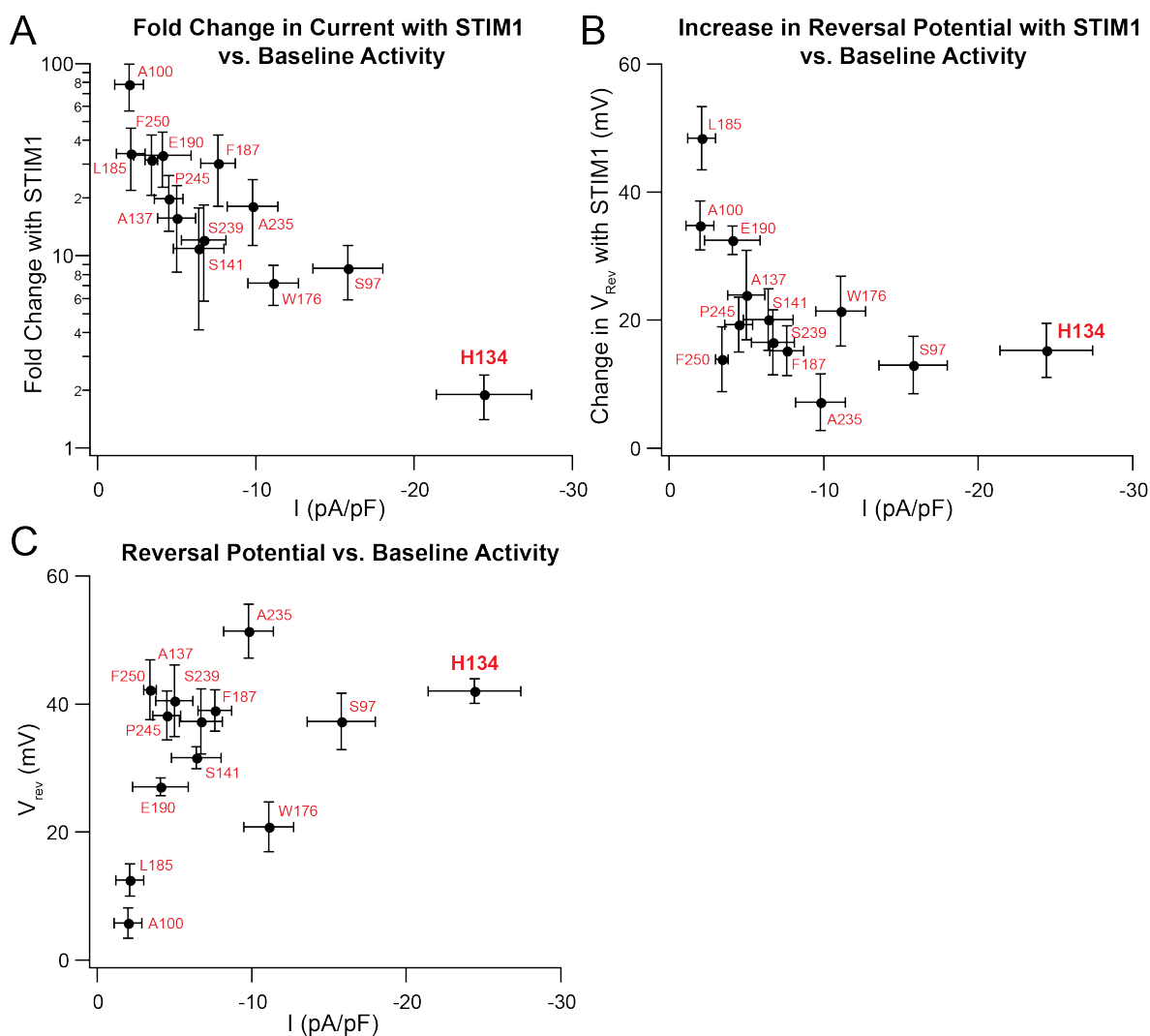


**Figure 3.5 Differential modulation of GOF cysteine mutants by STIM1.** (A) Plot of the fold change in current of GOF cysteine mutants in the presence of STIM1 versus current density in the absence of STIM1. The fold increase in current following whole-cell break-in was calculated by measuring the peak of the STIM1-gated current amplitude at 300 s or later divided by the amount of constitutive current seen at the time of whole-cell break-in ( $t=0$ ). ER  $Ca^{2+}$  stores were passively depleted by 8 mM BAPTA in the internal solution. Weakly active mutants can be further activated by STIM1, while mutants that are strongly open at baseline such as H134C are not significantly boosted. (B) STIM1 increases the  $Ca^{2+}$  selectivity of open mutants as reflected in the reversal potential. Increases in  $V_{rev}$  by STIM1 are inversely related to the baseline activity of GOF cysteine mutants. (C) H134C is the most strongly activating mutation based on the dual criteria of a large pre-activated current and very positive reversal potential at the time of whole-cell break-in relative to other GOF cysteine mutants. The leaky gate mutations, F99C and V102C, were excluded from these plots because they are constitutively permeant due to disruption of the gate itself in contrast to the activating mutations in TMs 2-4.

activate a mutant and enhance its  $Ca^{2+}$  selectivity diminishes with increasing baseline activity.

Notably, these plots showed that H134C, which has the largest constitutive current and a very

positive  $V_{rev}$ , exhibits the smallest STIM1-mediated increases in current and  $V_{rev}$  (**Figure 3.5**).

Based on these criteria, we conclude that among all the pre-activated mutants identified from the cysteine screen, H134C is the closest in its properties to physiological STIM1-gated Orai1 channels.

	Orai1 alone		Orai1 with STIM1		
	Current Density (pA/pF $\pm$ SEM)	Reversal Potential (mV $\pm$ SEM)	Fold Change in Current with STIM1 (Ratio $\pm$ SEM)	Reversal Potential (mV $\pm$ SEM)	
<b>WT</b>	-0.2 $\pm$ 0.02	*	1033 $\pm$ 568	52.3 $\pm$ 2.8	
<b>TM1</b>	<b>S97C</b>	-15.8 $\pm$ 2.2	37.3 $\pm$ 4.4	9 $\pm$ 3	50.3 $\pm$ 0.9
	<b>F99C</b>	-3.4 $\pm$ 0.7	11.9 $\pm$ 3.9	ND	ND
	<b>A100C</b>	-2.0 $\pm$ 0.9	5.8 $\pm$ 2.4	78 $\pm$ 21	40.5 $\pm$ 3.4
	<b>V102C</b>	-37.5 $\pm$ 8.2	27.2 $\pm$ 2.6	ND	ND
<b>TM2</b>	<b>H134C</b>	-24.4 $\pm$ 3.0	42.0 $\pm$ 1.9	2 $\pm$ 0.4	57.2 $\pm$ 3.7
	<b>A137C</b>	-5.0 $\pm$ 1.2	40.5 $\pm$ 5.6	16 $\pm$ 7	64.4 $\pm$ 4.1
	<b>S141C</b>	-6.4 $\pm$ 1.6	31.6 $\pm$ 1.7	11 $\pm$ 7	51.7 $\pm$ 4.6
<b>TM3</b>	<b>W176C</b>	-11.1 $\pm$ 1.6	20.8 $\pm$ 3.9	7 $\pm$ 2	42.2 $\pm$ 3.7
	<b>L185C</b>	-2.1 $\pm$ 0.9	12.5 $\pm$ 2.5	34 $\pm$ 12	60.9 $\pm$ 4.3
	<b>F187C</b>	-7.6 $\pm$ 1.1	39.0 $\pm$ 3.2	30 $\pm$ 12	54.1 $\pm$ 2.3
	<b>E190C</b>	-4.1 $\pm$ 1.8	27.1 $\pm$ 1.4	33 $\pm$ 11	59.6 $\pm$ 1.8
<b>TM4</b>	<b>A235C</b>	-9.8 $\pm$ 1.6	51.4 $\pm$ 4.2	18 $\pm$ 7	58.7 $\pm$ 1.2
	<b>S239C</b>	-6.7 $\pm$ 1.4	37.3 $\pm$ 5.1	12 $\pm$ 6	53.9 $\pm$ 3.1
	<b>P245C</b>	-4.5 $\pm$ 0.9	38.2 $\pm$ 3.8	20 $\pm$ 6	57.5 $\pm$ 2.2
	<b>F250C</b>	-3.4 $\pm$ 0.4	42.2 $\pm$ 4.7	32 $\pm$ 11	56.1 $\pm$ 1.9

**Table 3.1 Current densities and reversal potentials of GOF cysteine mutations in TMs 1-4.**

GOF cysteine mutations exhibit varying levels of current amplitudes and ion selectivity. Current amplitudes were measured during step pulses to -100 mV and reversal potentials were measured during ramps applied from -100 to 100 mV. In cells co-expressing STIM1, ER Ca<sup>2+</sup> stores were passively depleted by 8 mM BAPTA in the internal solution. The fold increase in current following whole-cell break-in was calculated by measuring the peak of the STIM1-gated current amplitude at 300 s or later divided by the amount of constitutive current seen at the time of whole-cell break-in (t=0). N = 4-16 cells. \*not measured due to small current amplitudes (<2 pA/pF). ND = not determined.

### **H134 regulates Orai1 gating through a steric mechanism**

The robust GOF phenotype of H134C on TM2 (**Figure 3.6A**) prompted us to further probe the mechanism by which this mutation induces constitutive channel activation. To address this question, we mutated H134 to all other amino acids and tested them in the absence and presence of STIM1. This analysis revealed that substitutions of H134 to smaller, or moderately sized but flexible residues (S/A/C/T/V/Q/E/M), produced GOF channels that were open without STIM1, while mutation to larger, more rigid residues failed to evoke constitutive activity (**Figure 3.6B**). A plot of the current density versus side-chain surface area revealed a trend towards spontaneous channel activation with diminishing side-chain size (**Figure 3.6B**). By contrast, no obvious dependence of constitutive channel activation with respect to hydrophobicity was observed (**Figure 3.6D**). A recent study proposed that H134 forms hydrogen bonds with two serine residues on the back of TM1 (S93 and S97) to maintain the closed channel state and that disrupting these hydrogen bonds evokes constitutive channel activity (45). However, our data argue against this hypothesis because H134S and H134T channels, which have hydroxyl groups presumably available for hydrogen bonding, are both robustly open without STIM1 (**Figures 3.6B, D and 3.7**).

When over-expressed with STIM1, the H134X channels exhibited several different types of phenotypes. Like H134C, H134A/S/T channels were also nearly maximally active at baseline, and did not display increases in current over time following whole-cell break-in (**Figure 3.7 and Table 3.2**). By contrast, H134V/E/M/Q channels were only partially active without STIM1 (**Figure 3.6B, D**), and STIM1 co-expression boosted both current amplitude and Ca<sup>2+</sup> selectivity of these mutants (**Figure 3.7**). H134N was the only mutant that was closed at rest and activated by STIM1 with kinetics indistinguishable from WT Orai1 (**Figure 3.7**). Several mutants additionally displayed loss-of-function (LOF) phenotypes with defects in STIM1-dependent gating. For

example, H134W and H134K channels showed very little current with STIM1 (**Figure 3.6**) despite seemingly normal membrane expression, suggesting that these bulky side-chains essentially block

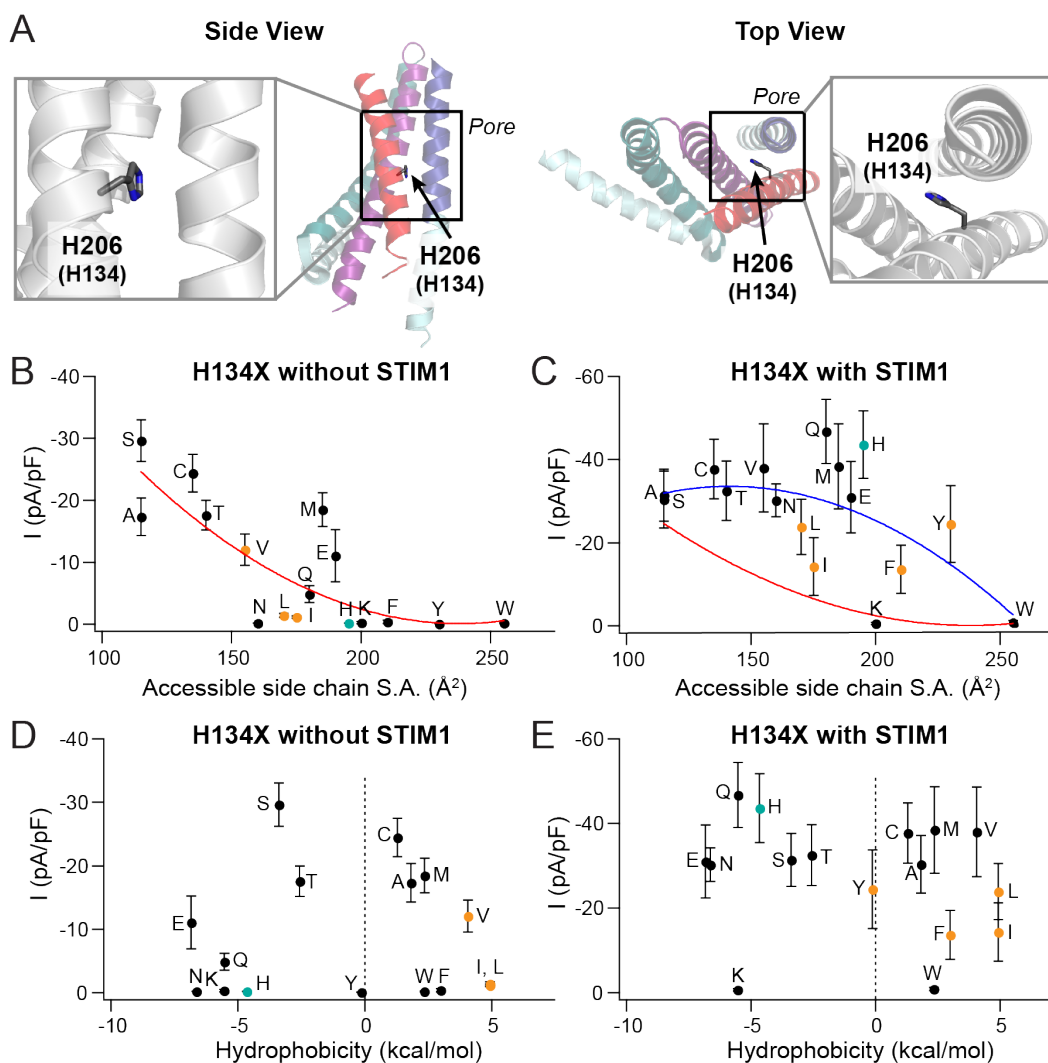


**Figure 3.6 Constitutive activity of H134X mutations depends on the size of the introduced residue.** (A) Top down and side views of H134 in the context of a dOrai monomer. H134 is located on TM2 and its imidazole ring faces the non-pore lining side of TM1. (B-C) Current densities of H134X mutants without and with STIM1 co-expression plotted against side-chain surface area. Red and blue lines represent polynomial fits to the data (without and with STIM1, respectively) to enable visualization of the overall trends. H134G and H134P were excluded from this analysis due to propensity of glycine and proline residues for breaking alpha helical secondary structure (4). H134R Orai1 did not express to the membrane and is not included. The native His residue is represented in teal. Orange points indicate mutants with nonselective currents ( $V_{rev} < 20$  mV). (D-E) Current density of H134X mutants versus the solvation energies (kcal/mol) of the substituted amino acid as a measure of its hydrophobicity. There is a strong inverse correlation between size and current amplitude in the absence of STIM1, but no clear dependence on hydrophobicity.  $N = 5-12$  cells. Values are mean  $\pm$  S.E.M.

channel activation by STIM1. On the other hand, H134L/I/F/Y exhibited “reluctant” gating in the presence of STIM1, with small, non-selective currents with reversal potentials of 8-14 mV compared to 50-60 mV of WT channels (**Figures 3.6 and 3.7, Table 3.2**).

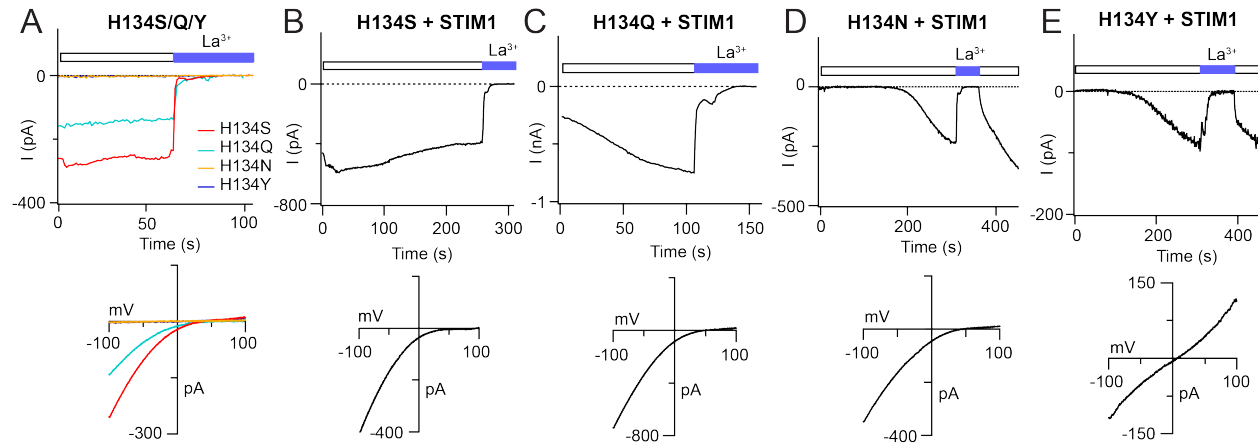


**Figure 3.7 Analysis of H134X mutants in the absence and presence of STIM1. (A)** H134S and H134Q Orai1 channels are constitutively active while H134N and H134Y channels are not open without STIM1. **(B)** Co-expression of STIM1 with H134S does not increase Orai1 current following whole-cell break-in. **(C)** Partially active H134Q mutant channels exhibit store-operated gating following whole-cell break-in indicating that they can be further activated by STIM1. **(D)** H134N channels are store-operated and  $\text{Ca}^{2+}$ -selective, similar to WT channels. **(E)** STIM1-mediated gating of H134Y channels is impaired as seen by the slow induction of a non-selective current following whole-cell break-in.

These results indicate that the constitutive activation of H134X channels arises from a reduction in the bulk of the native His at this position. We hypothesize that a decrease in the side-chain volume releases a “brake” at the TM1-TM2 domain interface, enabling the channel to open (see Discussion). Conversely, increasing the volume of the side-chain inhibits STIM1’s ability to gate the channel. Although no straightforward dependence of current density with respect to hydrophobicity of the introduced amino acid at H134 was observed (**Figure 3.6D**), non-polar substitutions tended to yield channels that were less selective for  $\text{Ca}^{2+}$  when activated by STIM1 in comparison to polar substitutions (**Figure 3.6E, Table 3.2**). This feature suggests that hydrophobicity at the TM1-TM2 interface may play a role in orienting TM1 helices into a  $\text{Ca}^{2+}$ -selective pore, a possibility meriting further study.

	Orai1 alone		Orai1 with STIM1	
	Current Density (pA/pF $\pm$ SEM)	Reversal Potential (mV $\pm$ SEM)	Fold Change in Current with STIM1 (Ratio $\pm$ SEM)	Reversal Potential (mV $\pm$ SEM)
<b>H134A</b>	-17.3 $\pm$ 3.0	49.1 $\pm$ 4.2	1 $\pm$ 0.1	59.9 $\pm$ 3.3
<b>H134C</b>	-24.4 $\pm$ 3.0	42.0 $\pm$ 1.9	2 $\pm$ 0.4	57.2 $\pm$ 3.7
<b>H134E</b>	-11.1 $\pm$ 4.2	52.4 $\pm$ 5.5	7 $\pm$ 3	61.0 $\pm$ 1.7
<b>H134F</b>	-0.4 $\pm$ 0.3	*	28 $\pm$ 11	12.4 $\pm$ 2.4
<b>H134G</b>	-1.5 $\pm$ 0.2	*	19 $\pm$ 6	59.7 $\pm$ 6.6
<b>H134I</b>	-1.2 $\pm$ 0.2	*	23 $\pm$ 7	13.6 $\pm$ 4.6
<b>H134K</b>	-0.3 $\pm$ 0.2	*	*	*
<b>H134L</b>	-1.4 $\pm$ 0.3	*	20 $\pm$ 11	8.8 $\pm$ 1.4
<b>H134M</b>	-18.5 $\pm$ 2.7	51.2 $\pm$ 4.3	15 $\pm$ 6	56.5 $\pm$ 3.9
<b>H134N</b>	-0.2 $\pm$ 0.02	*	268 $\pm$ 80	55.1 $\pm$ 4.2
<b>H134P</b>	-12.7 $\pm$ 3.7	48.0 $\pm$ 8.6	1 $\pm$ 0.1	52.4 $\pm$ 3.7
<b>H134Q</b>	-4.9 $\pm$ 1.3	53.1 $\pm$ 1.6	11 $\pm$ 3	54.3 $\pm$ 3.9
<b>H134S</b>	-29.7 $\pm$ 3.4	46.6 $\pm$ 4.3	1 $\pm$ 0.1	61.3 $\pm$ 2.9
<b>H134T</b>	-17.6 $\pm$ 2.4	51.9 $\pm$ 5.5	1 $\pm$ 0.1	53.6 $\pm$ 5.8
<b>H134V</b>	-12.1 $\pm$ 2.6	18.3 $\pm$ 2.0	13 $\pm$ 3	56.7 $\pm$ 8.1
<b>H134W</b>	-0.2 $\pm$ 0.1	*	*	*
<b>H134Y</b>	-0.1 $\pm$ 0.03	*	155 $\pm$ 44	8.3 $\pm$ 1.0

**Table 3.2 Current densities and reversal potentials of H134X mutations.** Different H134 substitutions give rise to currents with different degrees of constitutive activity and ion selectivity. Current amplitudes, reversal potentials, and fold change in current amplitude with STIM1 were determined as described in Table 3.1. N = 5-12 cells. \*not measured due to small current amplitudes (<2 pA/pF).

### The GOF H134S Orai1 pore configuration mimics STIM1-gated channels

Given that H134S strongly activates Orai1, we used this mutant as a tool to further dissect the mechanism of constitutive channel activation. Previous studies have shown that the outer region of the Orai1 pore harbors a hydrophobic gate that encompasses the residues V102 and F99 (2, 36, 46). STIM1 activates the channel, at least in part, by triggering rotation of the pore helix, to

displace F99 away from the pore axis and lower the energy barrier for ion conduction. One operational consequence of this displacement is that the coordination of metal ions such as  $\text{Cd}^{2+}$  and  $\text{Zn}^{2+}$  by a Cys introduced at F99 (F99C) sharply declines upon STIM1 binding (2). By contrast, G98, which is located on the opposite face of the pore helix (**Figure 3.8C**), becomes accessible to pore-applied divalent metal ions in the presence of STIM1, resulting in enhancement of  $\text{Cd}^{2+}$  coordination by G98C, and consequently, channel blockade (2). We hypothesized that if the GOF mutations represent a STIM1-like activated state of Orai1 with a rotated pore helix, there should also be weak  $\text{Cd}^{2+}$  accessibility at F99 but strong blockade at G98. By contrast, a “leaky” gate phenotype as in V102A or F99Y Orai1 mutants due to destruction of the channel gate should show strong coordination at F99, but not G98 (2). Consistent with the former scenario, we observed very little  $\text{Cd}^{2+}$  block at F99 ( $19 \pm 4\%$  blockade in F99C/H134S) but strong blockade at G98 ( $80 \pm 4\%$  blockade in G98C/H134S), indicating that F99C is positioned away from the pore axis in the H134S mutant (**Figure 3.8**). This pattern of  $\text{Cd}^{2+}$  blockade is akin to the pattern observed in V102A channels in the presence of STIM1 (2), indicating that the orientation of F99 and G98 is similar to that of STIM1-gated channels (**Figure 3.8C**).

In a second test to examine whether the H134S channel conformation resembles that evoked by STIM1, we asked whether this mutation increases the  $\text{Ca}^{2+}$  selectivity of the poorly  $\text{Ca}^{2+}$ -selective, constitutively conducting Orai1 variant V102C. We have previously shown that gating evoked by STIM1 enhances the  $\text{Ca}^{2+}$  selectivity of the V102C mutant channel (36, 57). In a similar fashion, introducing the H134S mutation boosted the  $\text{Ca}^{2+}$  selectivity of V102C Orai1, as evidenced by a significant rightward shift in the  $V_{\text{rev}}$  of V102C/H134S channels (**Figure 3.8D**). Taken together, these results indicate that the H134S activating mutation assumes a pore configuration close to that of STIM1-gated Orai1 channels.

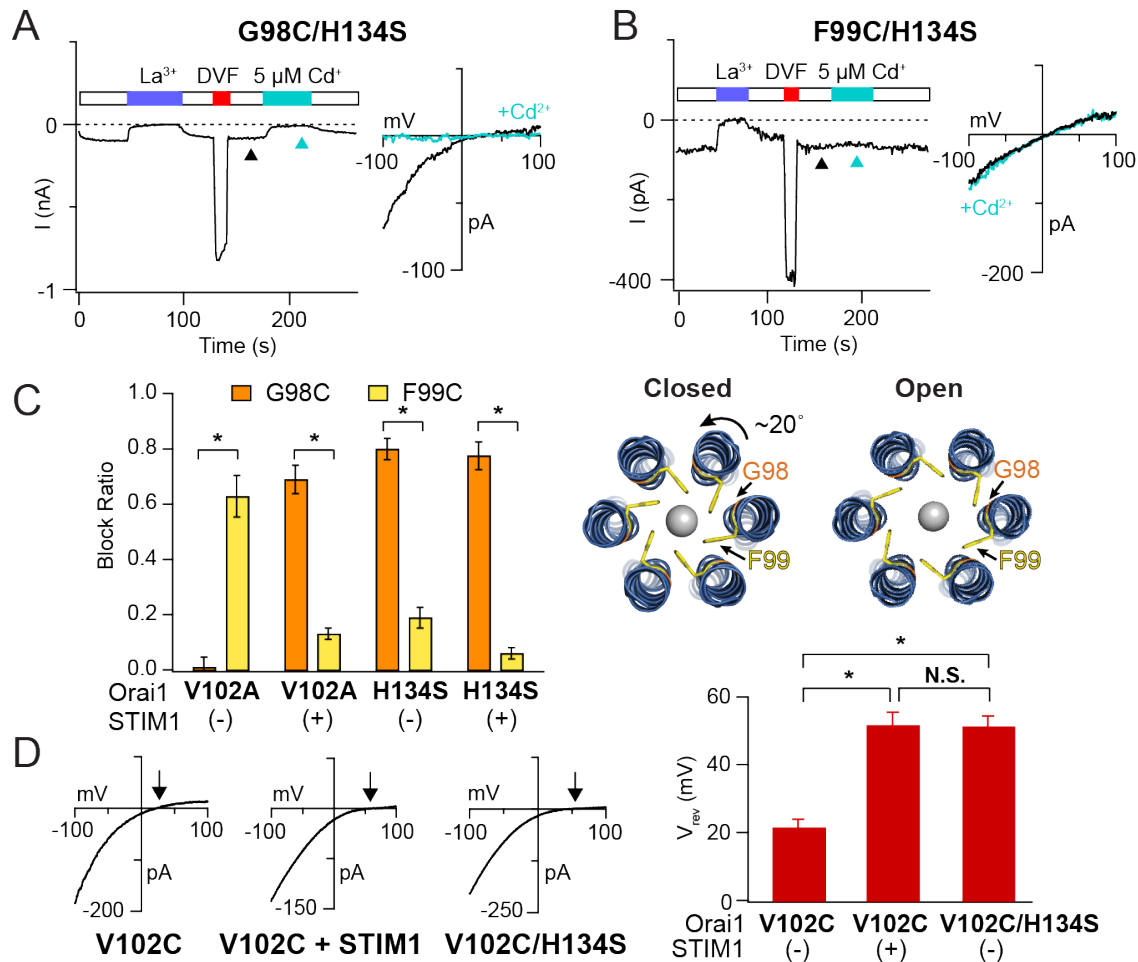


**Figure 3.8 Cd<sup>2+</sup> accessibility studies suggest that the pore conformation of H134S Orai1 is similar to that of STIM1-gated channels.** (A-B) Cd<sup>2+</sup> (5 μM) strongly blocks G98C, but not F99C residues in the H134S mutant. I-V relationships were measured at times indicated by the arrowheads. (C) Summary of Cd<sup>2+</sup> blockade at G98C or F99C in the H134S mutant. N = 4-6 cells. Values are mean ± S.E.M. (Data was collected by Megumi Yamashita.) For comparison, Cd<sup>2+</sup> blockade at these positions is also illustrated in the constitutively conducting V102A channels in the presence or absence of STIM1 (data from reference (2)). The pattern of blockade in the H134S mutant resembles that seen in STIM1-bound V102A channels, suggesting similar pore conformations. A schematic illustrating the open and closed states of the Orai1 pore showing rotation of the pore helix induced by STIM1 binding (adapted from reference (3)). (D) I-V relationships of V102C “leaky” mutant without and with the H134S activating mutation. As seen with STIM1, H134S confers Ca<sup>2+</sup> selectivity to V102C channels. Arrowheads indicate reversal potentials. N = 6-9 cells. Values are mean ± S.E.M. \*P < 0.05.

### Molecular simulations show that H134S rotates TM1 and enhances pore hydration

To understand how the H134S mutation alters the energetics of channel activation, we performed molecular dynamics (MD) simulations using models constructed from the *Drosophila* Orai

structure (**Figure 3.9**). We examined the degree of pore hydration and associated conformational fluctuations of WT, V174A, and H206S/C/Q/Y mutations corresponding to human Orai1 V102A and H134S/C/Q/Y. As previously observed (2), the pore helices of WT and V174A dOrai displayed spontaneous counter clockwise rotations, with the angular position of F171 shifted by  $17 \pm 1$  and  $22 \pm 1$  degrees respectively relative to the crystallographic dOrai structure (**Figure 3.10**). This spontaneous relaxation/rotation was strongly enhanced ( $P < 0.001$ ) in the dOrai H206S and H206C mutants, in which the average pore helix rotations were  $30 \pm 1$  and  $34 \pm 2$  degrees,

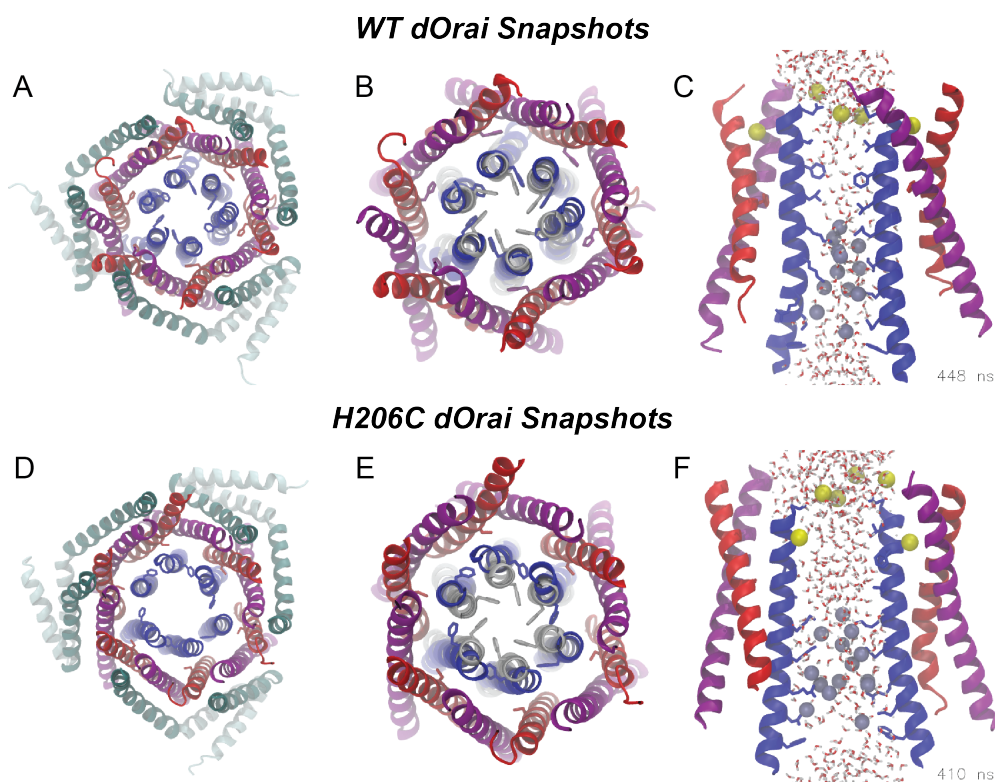


**Figure 3.9 Snapshots of MD simulations of WT and H206C dOrai channels.** (A-C) Snapshots of WT dOrai at 448 ns and (D-F) H206C dOrai at 410 ns. TMs 1-4 are colored in blue, red, purple and teal respectively, with the positions of residues F171 (blue) and H206 (red) shown as sticks. Intracellular and extracellular loops are not depicted. (A, D) Top views of the entire channel. (B, E) Top views of TMs 1-3. The crystallographic structure of dOrai TM1 and F171 sidechains are shown as a reference in white. (C, F) Side views of TM1 to TM3 for two diagonal subunits depicting water and ionic occupancy of the pore. All pore lining side-chains are depicted as sticks (from top to bottom; E178, V174, F171, L167, K163, R155, Q152, and W148). Na<sup>+</sup> and Cl<sup>-</sup> ions are rendered as yellow and dark blue spheres respectively. Water molecules are shown as grey/red sticks within a cylinder centered along the central pore axis. (Simulations were performed by Christopher Ing.)

respectively (**Figure 3.10A, E**). Further, the extent of helix rotation in H206S/C was accompanied by a striking increase in the number of water molecules in the hydrophobic stretch of the pore (**Figure 3.10C**). Notably, enhanced hydration was observed over a significantly larger stretch of

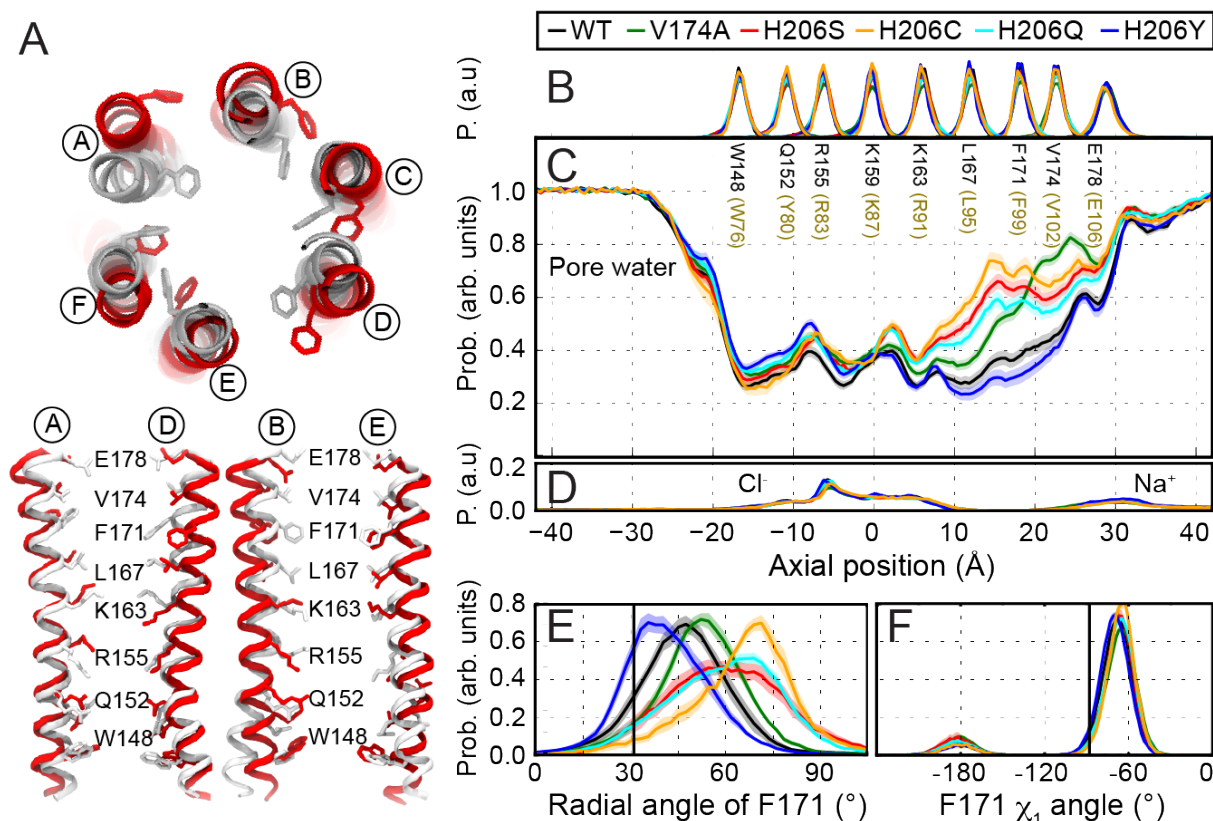


**Figure 3.10 Molecular dynamics simulations demonstrate increased pore helix rotation and pore hydration in GOF mutations H206S/C.** (A) Superposition of snapshots at t=350 ns from MD simulations of WT (grey) and H206S (red) as viewed from the top. The lower panels depict pairs of diagonal subunits viewed from the side. (B) Distributions of the axial position of C $\alpha$  atoms for all pore-lining residues. The residues corresponding to human Orai1 are shown in brown. Data in (A-F) were computed from simulations of WT (black) and of V174A (green), H206C (orange), H206S (red), H206Q (aqua), and H206Y (navy) mutant channels. Average distribution of (C) water oxygen atoms and (D) Na<sup>+</sup> and Cl<sup>-</sup> ions along the pore axis. The water occupancies of V174A and H206C/S/Q mutants deviate from those of WT and H206Y dOrai most significantly in the hydrophobic stretch of the pore. Bound Cl<sup>-</sup> and Na<sup>+</sup> counter-ions are found in the basic region of the inner pore and near E178 sidechains, respectively. (E) Average distribution of the radial angle of residue 171 defined as the angle between the pore axis, the center of mass of the two helical turns centered at residue 171, and the C $\alpha$  atom of residue 171. The means of these distributions over all simulation repeats in degrees are  $47 \pm 1$  for WT,  $53 \pm 1$  for V174A,  $61 \pm 1$  for H206S,  $65 \pm 2$  for H206C,  $59 \pm 1$  for H206Q, and  $42 \pm 1$  for H206Y. The radial angle in the crystallographic structure ( $31^\circ$ ) is shown as a black vertical bar for reference. (F) Average distribution of side-chain torsion  $\chi_1$  of residue 171 in WT, V174A and H206C/S/Q/Y mutants. The  $\chi_1$  of residue 171 in the crystallographic structure ( $-88^\circ$ ) is shown as a black vertical bar for reference. The traces depict values  $\pm$  S.E.M. (Data was collected by Christopher Ing.)

the pore encompassing more of the hydrophobic zone (L167-V174) than in the constitutively permeant V174A mutant.

To understand how these features compare to other mutants with differing levels of channel activity, we also modeled the H206Q (hOrai1 H134Q) mutant, which as described above yields partially active channels in the absence of STIM1 (**Figures 3.6, 3.7 and Table 3.2**). In line with this intermediate level of constitutive channel activity, MD simulations of H206Q showed slightly increased pore helix rotation ( $29 \pm 1$  degrees) and pore hydration (**Figure 3.10C, E**) compared to WT channels. By contrast, hOrai1 H134Y is not constitutively open and exhibits impaired STIM1-mediated gating with low  $\text{Ca}^{2+}$  selectivity (**Figure 3.7 and Table 3.2**). Consistent with this phenotype, MD simulations showed a lower extent of pore helix rotation as well as pore hydration in H206Y compared to WT ( $P < 0.001$ ), with an average F171 C $\alpha$  rotation of only  $11 \pm 1$  degrees, and a modest decrease in pore hydration compared to WT dOrai (**Figure 3.10C, E**). Thus, H206S/C and H206Y elicit opposite effects on pore helix rotation and pore hydration. The rotamer populations of F171 were comparable across all variants, indicating that lateral displacement of F171 occurred due to pore helix rotation rather than side-chain fluctuations. Interestingly, the simulations also showed that the activated mutants (H206S/C/Q and V174A) exhibit noticeable pore dilation compared to WT channels as measured by HOLE (70) analysis, especially in the hydrophobic stretch encompassing F99 (**Figure 3.11D-G**). Moreover, pore dilation at F99 was reduced in the loss-of-function H206Y mutant, suggesting that the extent of dilation is correlated with the “openness” of the mutants (**Figure 3.11C**).

Several interesting insights can be gleaned from this analysis. First, the close correlation between the constitutive activity of the variants as assessed by electrophysiology and pore hydration and pore helix rotation (**Figure 3.10C, E**) indicates that the molecular simulations are

able to recapitulate some key aspects of the experimentally detectable structural changes induced by the mutations. Second, the simulations reveal that changes in pore hydration are limited nearly exclusively to the hydrophobic section encompassing V102 and F99, with little to no change seen in the rest of the pore (**Figure 3.10C**), reaffirming the importance of the hydrophobic zone for Orai1 gating (2, 36, 46, 47). The simulations also revealed hitherto unappreciated pore dilation in

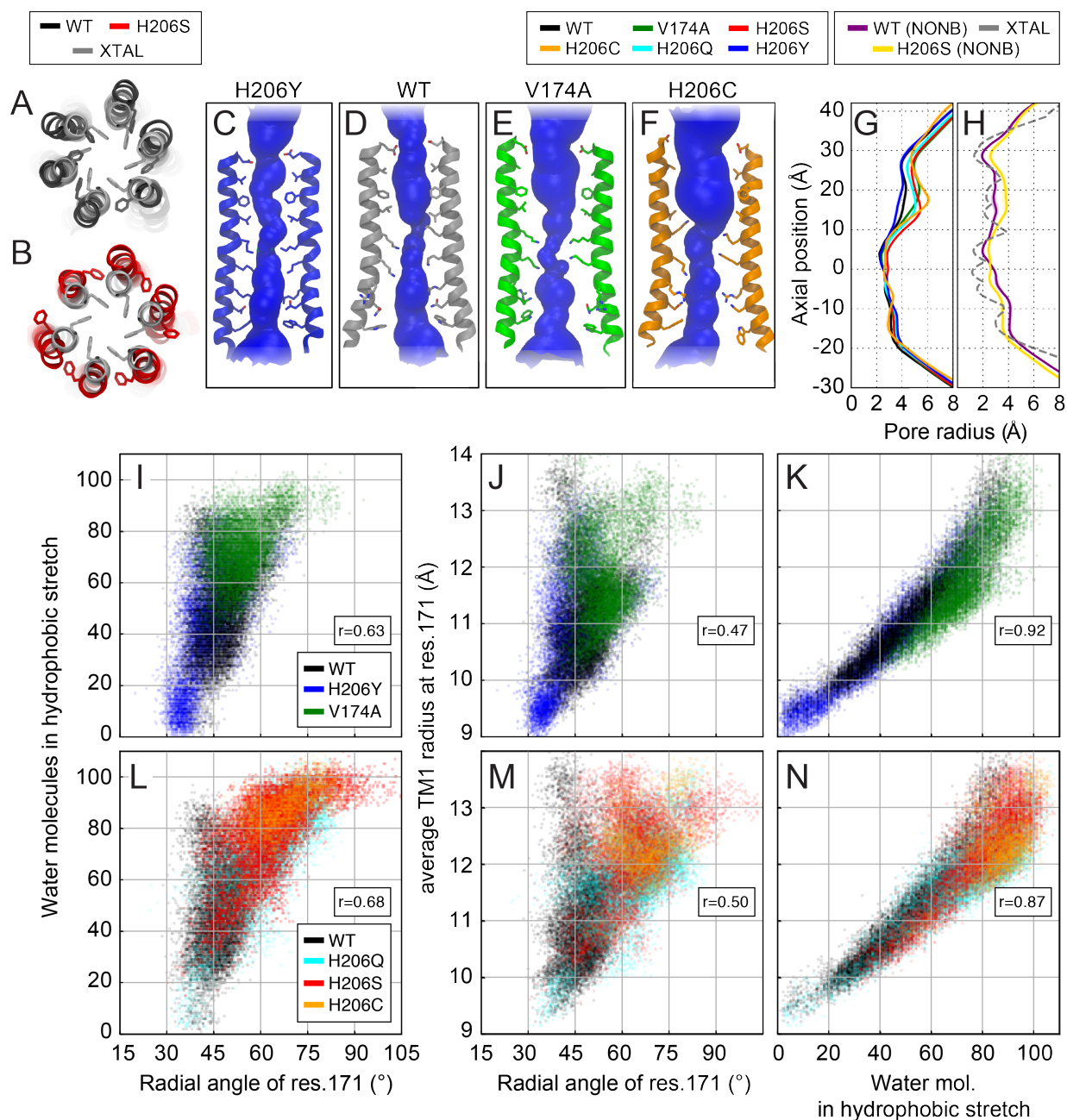


**Figure 3.11 Analysis of TM1 dilation, hydration, and rotation from molecular dynamics simulations.** (A-B) Comparison of simulation snapshots of WT (black) and H206S (red) models at  $t=350$  ns and the crystallographic structure of dOrai1 (white). (C-F) Pore profiles computed using HOLE from the H206Y, WT, V174A, and H206C models from snapshots taken at  $t=350$  ns. All water molecules and ions within the pore were removed for this analysis, and only two diagonal subunits are visualized. (G) Average pore radius for WT (black), V174A (green), and H206S/C/Q/Y (red, orange, aqua, blue) computed using HOLE for snapshots selected from  $\Delta t=20$  ns across all simulation repeats. Shaded regions depict values  $\pm$  S.E.M. (H) Average pore radius for WT (No NBFIX), H206S (No NBFIX), and the crystallographic structure of dOrai1. The axial coordinate system used for HOLE profiles of panels (G-H) is in agreement with those used for hydration profiles in Fig. 5C. (I, L) The relationship between the number of water molecules in the hydrophobic stretch (10-25 Å) and the mean radial angle of residue 171 (defined as the angle between the center of mass of the two helical turns centered at residue 171, and the  $C\alpha$  atom of residue 171) over all subunits. At small values of the residue 171 radial angle, the number of water molecules in the hydrophobic stretch is geometrically constrained, but with increased radial angle, the number of pore waters can vary significantly across a wide range. (J, M) The relationship between the average radius of the pore at residue 171 (defined as the distance in the X-Y plane from the pore center of mass to the center of mass of residues 167-175  $C\alpha$  atoms, averaged over all subunits) to the mean radial angle of residue 171. (K, N) The correlation between average radius of the pore at residue 171 and the number of water molecules in the hydrophobic stretch. For all scatter plots, each point corresponds to data taken at an individual simulation snapshot, from all snapshots spaced at  $\Delta t=1$  ns for WT (black), V174A (green), and H206S/C/Q/Y (red, orange, aqua, blue) models. Pearson correlation coefficient is shown as an in-set in panels I-M. (Data and figure were generated by Christopher Ing.)

the hydrophobic stretch that is well-correlated with the degree of helix rotation and especially with pore hydration (**Figure 3.11I-N**). This observation raises the possibility that along with the experimentally detectable displacement of the F99 residues, widening of the pore in the hydrophobic zone may also contribute to lowering of the free energy barrier for ion conduction. However, because current electrophysiological methods do not have the resolution needed to resolve the small changes in pore radius seen in the simulations, these predictions await experimental validation with alternative approaches.

### **Atomic packing and hydrophobicity analysis reveals distinct functional contacts between the TM1 and TM2/3 helices**

The results discussed thus far imply that the non-pore lining TMs play crucial roles in Orail channel gating by STIM1. To understand the structural basis of how the individual TM amino

acids mediate these effects, we next mapped the packing densities of inter-helical surfaces using a small-probe contact dots protocol (71, 72), which provides a rapid and computationally facile means to evaluate packing interactions on a residue-by-residue basis. We complemented this analysis with maps of the hydrophobicity of the residues at the TM1-TM2/3 interface to assess the contribution of hydrophobic interactions to this interface. As the enthalpic contribution to the stabilization of packing interactions should be proportional to the atomic surface areas in contact, residues exhibiting extensive interactions likely contribute more to the stability of an interface, and to the coupling between structural elements, than residues with less interaction surface. As a consequence, tightly packed regions in proteins are generally more rigid, while loosely packed regions more readily undergo conformational change (71, 72).

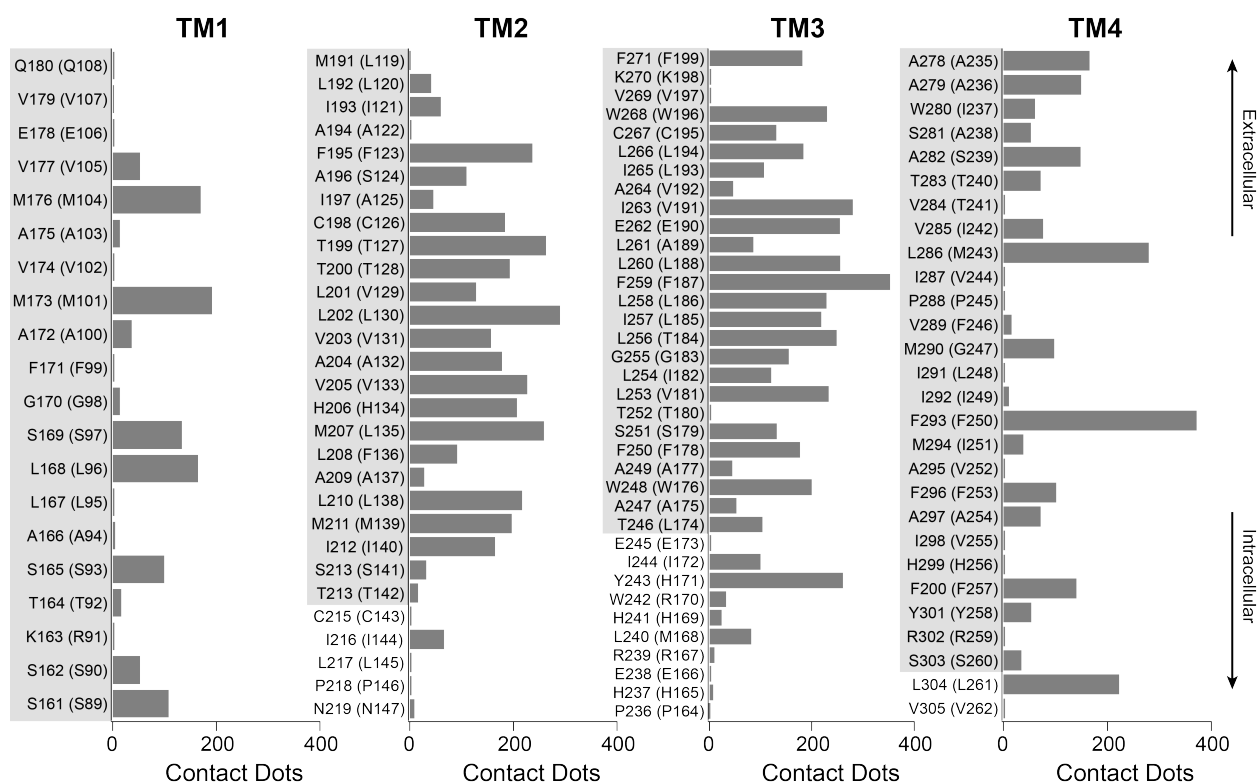


**Figure 3.12 Atomic packing analysis of all transmembrane residues in dOrai.** The total number of contact dots per residue measured for each transmembrane amino acid in the hexameric dOrai crystal structure including intramolecular and intermolecular neighbors. Residues in TMs 2 and 3 make more contacts with their neighbors compared to those in TMs 1 or 4, suggesting that they are more tightly packed. (Data was collected by Douglas Freymann.)

Applying this analysis to the residues in direct contact with the pore helix revealed several intriguing structural features. First, the contact dots analysis of dOrai shows that the atomic packing density varies significantly across and within the TM1-TM4 bundle of helices (**Figure 3.12**). Interestingly, the TM2/3 helix pair displays substantially more contacts and a more uniform packing density across its interfaces than do either TM1 or TM4 (**Figure 3.12**). With both intra- and inter-subunit surfaces lined mostly by large hydrophobic residues, TMs 2 and 3 have the appearance of an interlocked ring situated between TMs 1 and 4. Second, the analysis reveals a prominent cluster of interdigitating hydrophobic residues lining the interface between TM1 and the TM2/3 ring near the extracellular region that forms a hydrophobic stack (**Figures 3.13, 3.14**).

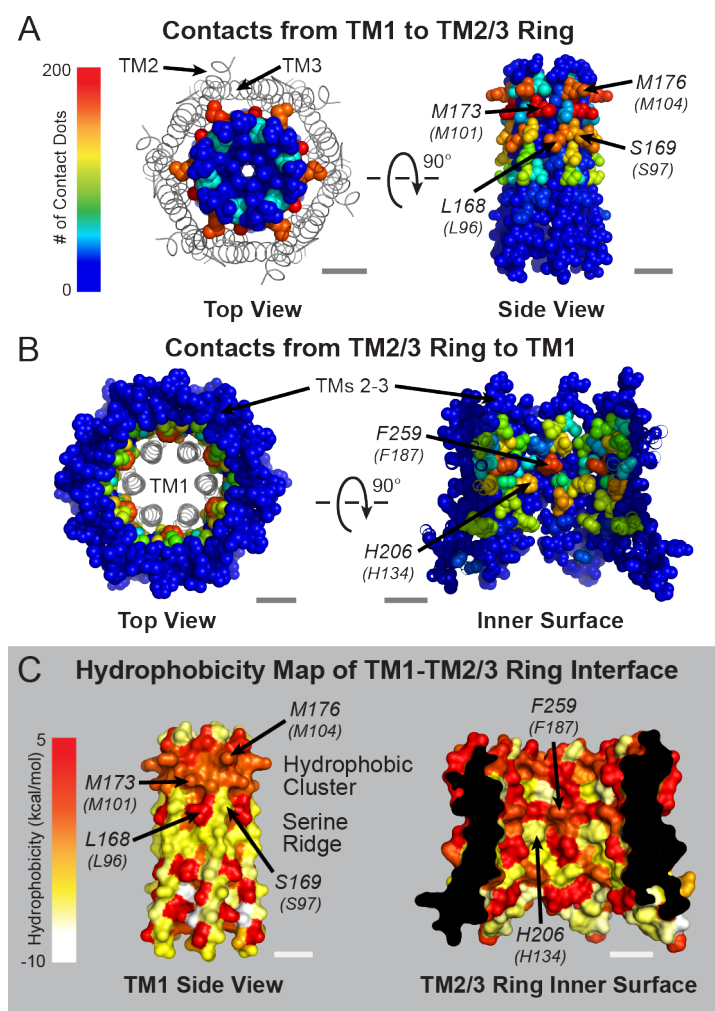


**Figure 3.13 Atomic packing analysis and hydrophobicity mapping of dOrai reveals two distinct interfaces between the TM2/3 and TM1 segments. (A, B) Top view and side view of space-filling representations of the interface between TM1 and the TM 2/3 ring colored by the number of contacts per residue measured using small-probe contact analysis. TM4 is hidden for clarity. In panel A, TMs 2 and 3 are shown as ribbons. (Data was collected by Douglas Freymann.) (C) Surface representation of the non-pore lining residues of TM1 and residues of the TM2/3 ring facing TM1 colored according to hydrophobicity as defined by cyclohexane to water transfer energies (47). The hydrophobic cluster towards the external surface of the helix and the serine ridge towards the cytosolic side of the protein are labelled. Scale bars = 10 Å.**

And third, moving towards the cytoplasmic side, there are alternating ridges of hydrophobic and polar residues on the back of TM1 that appear to interact with complementary hydrophobic and polar stripes on the inner interface of the TM2/3 ring (**Figures 3.13C, 3.15**). Below, we address the functional roles of these structural elements for relaying the gating signal to the central pore.

### **A cluster of TM3-TM1 hydrophobic contacts is critical for STIM1-mediated Orai1 gating**

The stack of interdigitating hydrophobic residues on the extracellular region of the channel is the locus of highest packing density at the TM1 to TM2/3 ring interface (**Figure 3.13A, B**). This hydrophobic cluster is comprised of TM1 residues L168, M173, M176 and V177 (hOrai1 L96, M101, M104, V105) closely packed against the TM2/3 residues F195, F259, I263, L266 (hOrai1 F123, F187, V191, L194) (**Figure 3.14A**). Intriguingly, this cluster of hydrophobic residues is located at the same depth as the selectivity filter (E106) and the hydrophobic gate (V102/F99), raising the tempting possibility that this structural transition zone between the pore domain and the TM2/3 ring is a natural site of communication for regulating pore opening and ion selectivity.

We examined this possibility by substituting each of the residues of the hydrophobic cluster to Ala, a small, less hydrophobic amino acid that is not expected to destabilize the local helical structure. Consistent with our prediction, the alanine scan revealed that decreasing the number of contacts and the hydrophobicity in this region resulted in channels that could no longer be gated by STIM1 (**Figure 3.14B, C**). The L96A, M101A, M104A, F187A, and L194A mutations all abrogated STIM1-mediated Orai1 activation (**Figure 3.14B, C**). The one exception to this trend was V191A, which retained store-operated gating (**Figure 3.14C**), possibly reflecting the similar size and non-polar nature of Val and Ala residues, and potentially a lesser role for V191 in the

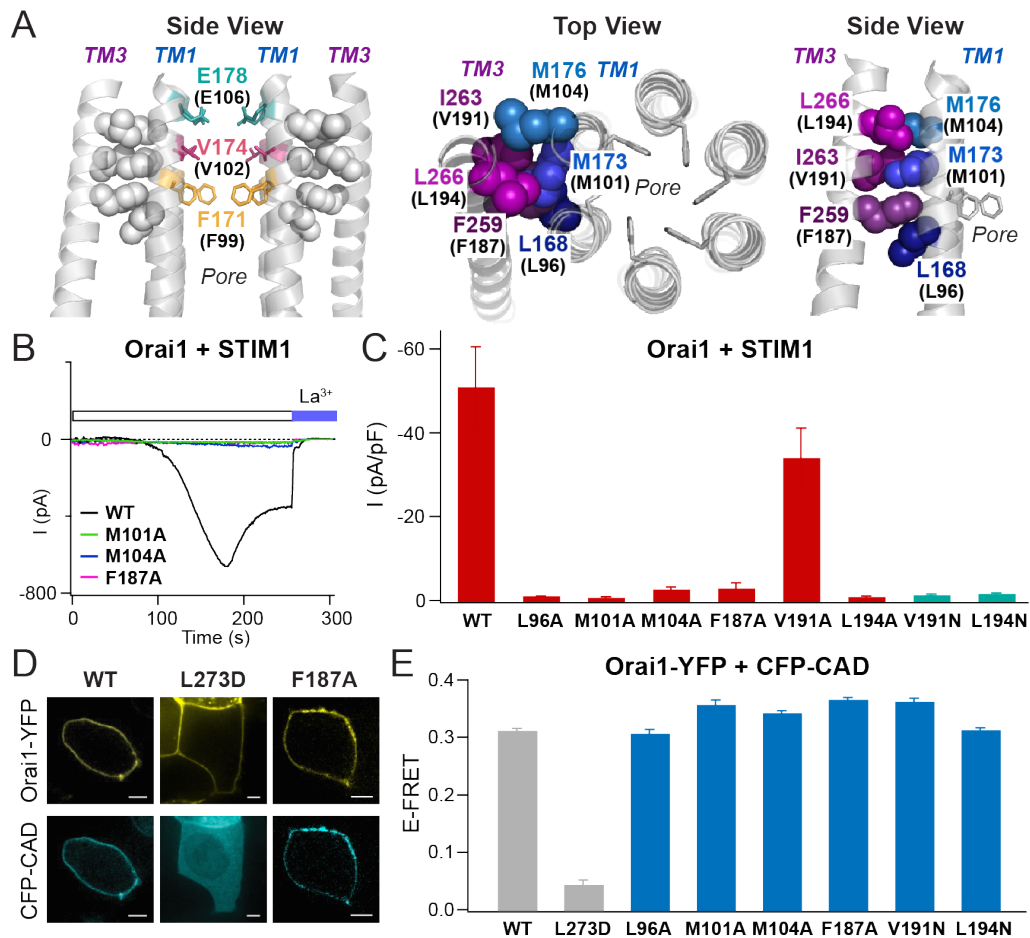


**Figure 3.14 The TM3-TM1 hydrophobic cluster is essential for Orai1 gating by STIM1.** (A) Left panel shows a side view of the hydrophobic contacts (grey spheres) between the TM1 pore helices with the TM3 segment. The selectivity filter (E106, teal) and hydrophobic gate residues (V102, magenta and F99, yellow) are also shown. Four TM1 helices and two TM3 helices are shown for simplicity. Middle and right panels are top down and side views of the six residues forming the hydrophobic stack. Amino acids are labeled with dOrai numbering and hOrai1 numbering in parentheses. (B) Single mutations of the hydrophobic stack abrogate Orai1 activation by STIM1. Representative traces of WT Orai1 and M101A, M104A and F187A Orai1 mutants co-expressed with STIM1 are shown following whole-cell break-in. (C) Current densities of the indicated Orai1 mutations in the TM3-TM1 hydrophobic cluster co-expressed with STIM1. N = 4-6 cells. Values are mean  $\pm$  S.E.M. With the exception of V191A, these mutations abrogate Orai1 activation by STIM1. (D) Confocal images of WT, L273D, and F187A Orai1-YFP constructs co-expressed with CFP-CAD showing normal CAD binding in F187A mutant. Scale bars = 5  $\mu$ m. (E) E-FRET between the indicated Orai1-YFP channels and CFP-CAD, showing that the hydrophobic cluster LOF mutations do not impair Orai1-STIM1 binding. N = 53-88 cells for each mutant. Values are mean  $\pm$  S.E.M.

middle of the hydrophobic stack compared to its larger, more hydrophobic Met and Leu neighbors (Figure 3.14A). Yet, even at this position, a V191N substitution impaired STIM1 gating (Figure 3.14C). The loss of functional activity of the above mutants is not due to deficiencies in expression

in the plasma membrane or STIM1 binding as indicated by unaltered levels of FRET between CFP-CAD and Orai1-YFP, and the recruitment of CFP-CAD to the plasma membrane (**Figure 3.14D, E**). Taken together, mutational analysis of the hydrophobic clamp indicates that disrupting hydrophobic interactions between TM3 and TM1 abolishes communication between the TM1 pore segment with the other helices and the ability of STIM1 to open the pore.

### **The disease mutation S97C activates Orai1 through a hydrophobic switching mechanism**

In striking contrast to the tight packing in the hydrophobic cluster towards the extracellular region, the cytoplasmic region of the non-pore facing TM1 surface exhibits relatively low packing density with the TM2/3 ring (**Figure 3.13A**). This is because the central residues at the interface arise from a ridge of serine side-chains S154, S161, S162, S165, and S169 (hOrai1 S82, S89, S90, S93, S97) (73), which in addition to being more loosely packed than the hydrophobic clamp, are also polar (**Figure 3.13A, C**). A band of alternating hydrophobic and polar residues formed by L96 and S97 features prominently in this zone (**Figure 3.13C**). This pattern of polar-hydrophobic regions on TM1 appear to pair with complementary polar-hydrophobic stripes on the surface of the TM2/3 ring (**Figure 3.13C**), suggesting that mutations that increase the hydrophobicity of the serine ridge may force an interaction with a hydrophobic region on TM2/3 ring instead of its usual polar interaction partners. This possibility is intriguing since a recent report has described a GOF human Orai1 mutation S97C that causes a Stormorken-like syndrome with tubular aggregate myopathy and congenital miosis (15). The molecular basis of the GOF phenotype of this mutant is currently not understood, but such a switching mechanism could potentially explain its constitutive activity.

Consistent with this scenario, hydrophobic substitutions at S97 including Cys, Val, Leu, Ile, and Met yielded Orai1 channels that were partially open in the absence of STIM1 (**Figure**

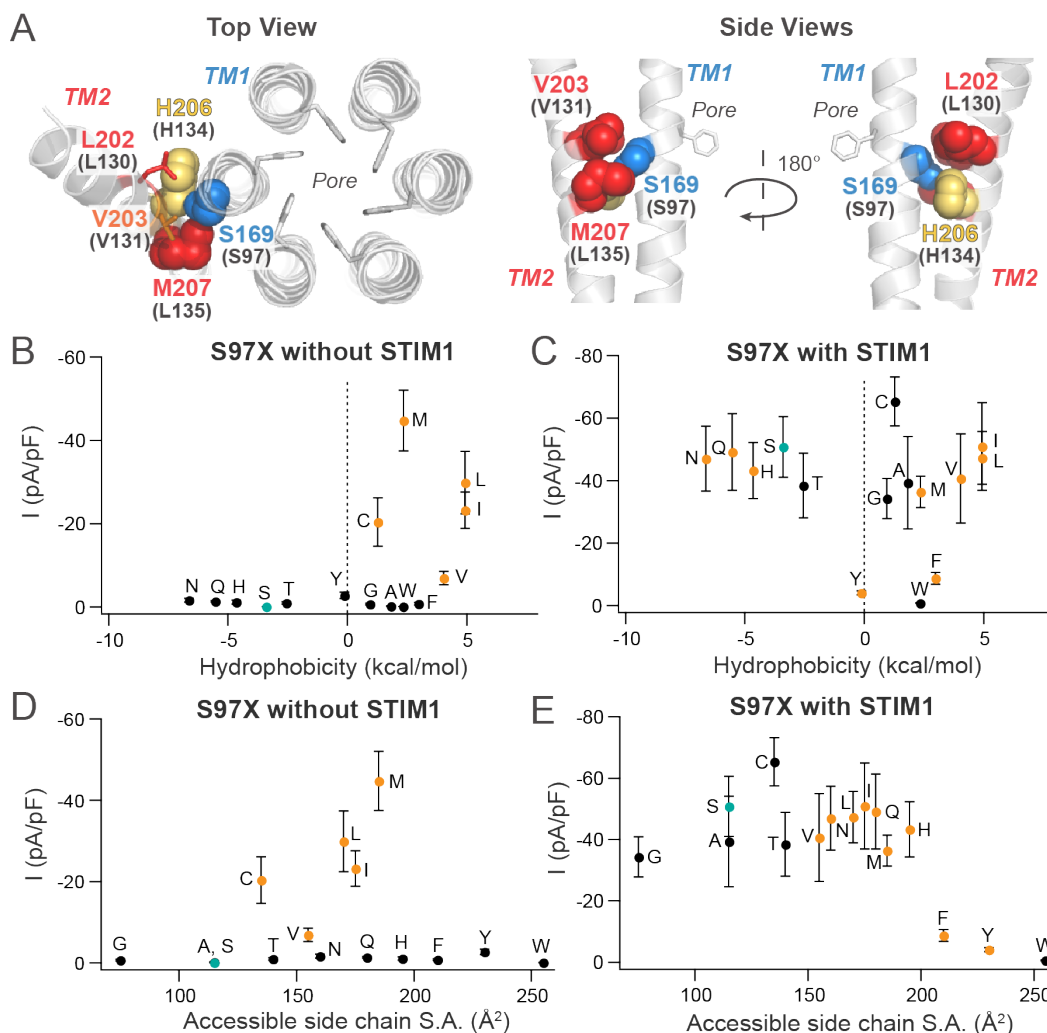


**Figure 3.15 Hydrophobic substitutions at S97 evoke constitutive channel activity.** (A) Top down and side views of TMs 1 and 2 in the dOrai structure showing S169 (hOrai1 S97, blue) with H206 (hOrai1 H134, yellow), and the non-polar residues L202 (hOrai1 L130, red), V203 (hOrai1 V131, orange sticks) and M207 (hOrai1 L135, red). F99 side-chains are shown as grey sticks. (B-C) The current densities of S97X mutants in the absence and presence of STIM1 co-expression are plotted against the solvation energies (kcal/mol) of the substituted amino acid as a measure of its hydrophobicity (47). The native Ser is depicted in teal. Substitutions that give rise to non-selective channels ( $V_{rev} < 35$  mV) are shown as orange points. (D-E) Current densities of S97X mutants plotted against the accessible side-chain surface area of the introduced amino acid without and with STIM1. Mutant channels with small substitutions retain store-operated,  $Ca^{2+}$  selective WT behavior, while non-polar or large substitutions cause the channel to become non-selective or unable to be activated by STIM1.  $N = 4-11$  cells. Values are mean  $\pm$  S.E.M.

**3.15B).** By contrast, mutation of S97 to similarly-sized, polar residues such as Asn, Gln, and Thr did not produce constitutively open channels (Figure 3.15D) but instead remained store-operated.

In the dOrai crystal structure, S97 is located on the non-pore lining face of TM1 surrounded by

three hydrophobic TM2 residues L130, V131, L135, and the bulky, polar H134 (**Figure 3.15A**). Although speculative, this structural feature raises the possibility that non-polar substitutions at S97 promote hydrophobic interactions with residues V131 and L135 on the TM2/3 ring, thereby moving this residue away from the polar H134 (**Figure 3.15A**). The net effect is predicted to induce a slight counter-clockwise rotation of the TM1 helix, which should lower the free energy barrier at the V102/F99 region in the pore to allow ion conduction.

Interestingly, with the exception of S97G/A/T mutants, which exhibited WT store-operated behavior, introduction of hydrophobic or large amino acids at position 97 yielded non-selective currents when gated by STIM1 (**Figures 3.15 and 3.16, Table 3.3**). We postulate that hydrophobic substitutions disrupt the alternating polar/non-polar interface with the TM2/3 ring, thereby creating a “sticky” hydrophobic patch that constrains the motions of the TM1 segment and traps the channel

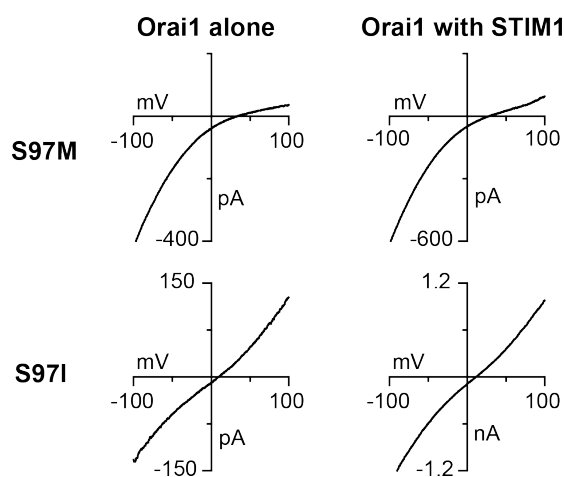


**Figure 3.16** The  $\text{Ca}^{2+}$  selectivity of the constitutively conducting S97M and S97I mutants is not enhanced by STIM1. I-V relationships of S97M and S97I mutants in the absence and presence of STIM1. Unlike most other GOF mutants, STIM1 does not significantly enhance the reversal potential of these mutant channel I-Vs.

in a non-selective open state. Large amino acid substitutions (S97F/Y/W) likely reduce the conformational flexibility of the TM1 segment through steric effects (**Figure 3.15E**), much like the LOF phenotypes of bulky H134X mutants (**Figure 3.6C**). Overall, these data suggest that the small, polar nature of S97 as part of the serine ridge provides a degree of conformational flexibility at the TM1-TM2/3 ring interface that is essential for STIM1 gating and ion selectivity.

	Orai1 alone		Orai1 with STIM1	
	Current Density (pA/pF $\pm$ SEM)	Reversal Potential (mV $\pm$ SEM)	Fold Change in Current with STIM1 (Ratio $\pm$ SEM)	Reversal Potential (mV $\pm$ SEM)
<b>S97A</b>	-0.2 $\pm$ 0.1	*	107 $\pm$ 46	51.8 $\pm$ 3.6
<b>S97C</b>	-20.4 $\pm$ 5.7	38.4 $\pm$ 5.7	8 $\pm$ 3	50.3 $\pm$ 0.9
<b>S97F</b>	-0.8 $\pm$ 0.3	*	12 $\pm$ 4	30.0 $\pm$ 3.3
<b>S97G</b>	-0.7 $\pm$ 0.2	*	79 $\pm$ 58	61.2 $\pm$ 3.2
<b>S97H</b>	-1.1 $\pm$ 0.4	*	32 $\pm$ 18	18.3 $\pm$ 2.6
<b>S97I</b>	-23.2 $\pm$ 4.4	7.3 $\pm$ 0.7	6 $\pm$ 1	9.8 $\pm$ 2.1
<b>S97L</b>	-29.9 $\pm$ 7.5	31.7 $\pm$ 5.3	2 $\pm$ 1	32.9 $\pm$ 3.1
<b>S97M</b>	-44.7 $\pm$ 7.3	27.9 $\pm$ 4.1	1 $\pm$ 0.1	33.3 $\pm$ 6.3
<b>S97N</b>	-1.7 $\pm$ 0.5	*	37 $\pm$ 18	19.0 $\pm$ 3.2
<b>S97Q</b>	-1.4 $\pm$ 0.1	*	53 $\pm$ 14	28.6 $\pm$ 3.4
<b>S97T</b>	-0.9 $\pm$ 0.3	*	112 $\pm$ 27	46.8 $\pm$ 5.1
<b>S97V</b>	-6.9 $\pm$ 1.6	8.9 $\pm$ 0.8	20 $\pm$ 7	11.9 $\pm$ 1.3
<b>S97W</b>	-0.1 $\pm$ 0.03	*	*	*
<b>S97Y</b>	-2.7 $\pm$ 0.7	14.3 $\pm$ 3.8	2 $\pm$ 1	16.3 $\pm$ 4.4

**Table 3.3 Current densities and reversal potentials of S97X mutations.** S97X mutants display varying levels of constitutive activity and ion selectivity. Current amplitudes, reversal potentials, and fold change in current amplitude with STIM1 were determined as described in Table 3.1. N = 4-8 cells. \*not measured due to small current amplitudes (<2 pA/pF).

## **Discussion**

While prior studies have identified individual GOF and LOF mutations within the Orai1 transmembrane helices (11, 13-16, 58, 61), our study is the first one to systematically examine the roles of all four TMs in gating. The identification of GOF mutations encompassing all regions of Orai1 strongly suggests a concerted, global gating mechanism that involves the entire protein rather than a localized motion at the N-terminus and TM1, consistent with a gating signal being transmitted through the lipid-spanning regions of the TMs. Notably, the large number of GOF

mutations identified through the cysteine screen implies that the energy barrier to Orai1 pore opening is likely not large. We postulate that the constitutively open cysteine mutations activate the channel by removing inter-TM constraints that maintain the closed conformation. Since the mutants have varying degrees of current density and ion selectivity and almost all can be further gated by STIM1, several of the mutants likely represent trapped intermediate states along the STIM1 gating pathway. These mutants could serve as a critical resource for future drug discovery studies aimed at manipulating the function of Orai1 channels and for x-ray crystallography or cryo-EM studies aimed at elucidating the structure of the open channel.

A note-worthy feature of the constitutively active mutants is that their function is abrogated by mutations in the Orai1 N-terminus (K85E and  $\Delta$ 2-85) that are known to impair STIM1-mediated gating (51, 52, 55-57, 66). Although residues 73-85 in this region of the N-terminus are also thought to directly bind STIM1 (26), this result suggests that the loss of channel function in the Orai1 N-terminal mutations may not be directly related to lack of STIM1 binding to this site. This conclusion is consistent with other recent studies that have examined the contribution of the membrane proximal N-terminus for Orai1 gating (58, 67). We do not yet know how the Orai1 N-terminus contributes to channel function, but possible explanations could include an interaction with another part of Orai1 in the open state (74) or a role in ion permeation (75).

Our results also suggest a potential mechanism by which H134 orchestrates Orai1 gating. The position and orientation of histidine side-chains are defined by two torsion angles,  $\chi_1$  and  $\chi_2$ . However, at the 3.35Å resolution of the electron density map of 4HKR (41), the  $\chi_2$  angle cannot be determined directly and must be inferred from the availability of potential hydrogen bonding partners and known rotameric positions available to histidine side-chains in alpha helices (76, 77). For H206 (hOrai1 H134) in 4HKR, the assigned  $\chi_1$ ,  $\chi_2$  angles of  $-82^\circ$ ,  $-60^\circ$  orient the ND1 nitrogen

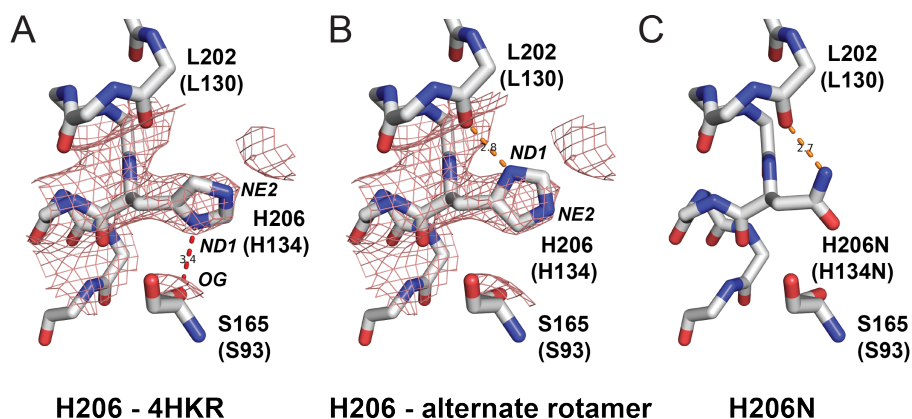


**Figure 3.17 Alternate rotamer of H206 and H206N may interact with the TM2 backbone carbonyl to stabilize its conformation at the TM1-TM2 interface. (A)** Electron density of 4HKR superimposed with the H206 side chain as built in the 4HKR structure with the assigned  $\chi_1$ ,  $\chi_2$  angles of  $-82^\circ$ ,  $-60^\circ$ . In this rotamer, the ND1 nitrogen of the imidazole ring may interact with S165 (3.4 Å). The map is contoured at  $1.5\sigma$ . **(B)** Alternate rotamer of H206 with  $\chi_1$ ,  $\chi_2$  angles of  $-82^\circ$ ,  $80^\circ$  is also consistent with the electron density of 4HKR and allows hydrogen bonding (2.8 Å) between the ND1 nitrogen with the backbone carbonyl of L202 one turn preceding it. **(C)** In an H206N substitution, the side chain can also adopt a rotameric configuration allowing hydrogen bonding between the ND2 nitrogen and the carbonyl oxygen (2.8 Å) of L202, thereby possibly stabilizing it in a similar configuration towards the TM1-TM2 interface. hOrai1 numbering is indicated in parentheses. (Figure generated by Douglas Freymann.)

towards the side-chain OH of S165 (hOrai1 S93) (**Figure 3.17A**), raising the possibility that a hydrogen bond between these residues plays a significant functional role (45, 73). However, a different side-chain rotamer is also fully consistent with the crystallographic electron density. This rotamer, which adopts  $\chi_1$ ,  $\chi_2$  angles of  $-82^\circ$ ,  $80^\circ$  (i.e. a  $\sim 140^\circ$  rotation about the  $C_\beta$ - $C_\gamma$  bond) is found to be selectively enriched in transmembrane helices (76) because it allows for intra-helical hydrogen bonding between the ND1 nitrogen of the imidazole ring and the carbonyl oxygen of the *i*-4 residue preceding it in the alpha helix (**Figure 3.17B**). We can propose then, with equal validity based on the crystallographic evidence, that the potentially significant interaction of H206 (hOrai1 H134) side-chain is not with S165 of TM1 (hOrai1 S93), but instead with the backbone carbonyl of L202 (hOrai1 L130). This intra-helical interaction could stabilize the orientation of the histidine side-chain such that it functions as a steric “brake” at the nexus of the interface between helices TM1, TM2, and TM3 that can be released through the substitution of the endogenous His with

small and flexible amino acids. Intriguingly, an asparagine substitution at position 206 is isosteric for the four overlapping atoms with the His, predicting that this side-chain should also readily adopt a rotameric position that allows formation of an intra-helical hydrogen bond of its ND2 nitrogen with the carbonyl oxygen of L202 (77) (**Figure 3.17C**). Indeed, the hOrai1 H134N substitution is the one mutant that behaves like WT Orai1. Overall, these results suggest that the loss of the privileged intrahelical stabilization available for His and Asn side-chains by small and flexible substitutions destabilizes the interface to release the “brake”. By contrast, larger substitutions at H134 would be expected to hinder the flexibility between the TM1 and TM2 segments needed for gating, leading to LOF phenotypes.

Based on our results, there are two possible ways in which Orai1 can conduct ions in the absence of STIM1: i) because of a “leaky” gate caused by mutations of V102/F99 residues that comprise a hydrophobic channel gate (2, 36), or ii) due to activation gating which would involve displacement the F99 side-chains away from the pore axis (2). Albeit through different mechanisms, both would be expected to diminish the free energy barrier for water and ions, thereby permitting ion conduction. In the Ca<sup>2+</sup>-selective H134S mutant channels where the hydrophobic gate itself is intact, our results indicate that this mutation mimics the activated state of Orai1 by configuring the pore analogous to STIM1-activated channels. We believe that a similar mechanism involving activation of the hydrophobic channel gate underlies the GOF phenotypes of S97C and P245L, given the similarity of permeation properties of H134S with these disease-linked mutations (13, 15). It is also notable that in the MD simulations, the hydrophobic stretch is the only region undergoing changes in hydration between closed vs. open channel variants, reaffirming that this region is likely the primary regulator of channel gating.

The non-pore lining surface of TM1 contains two qualitatively distinct functional interfaces identifiable on the basis of packing density and hydrophobic or hydrophilic character. Towards the extracellular side of the channel is a hydrophobic stack formed by TM1 with the TM2/3 ring, located close to the selectivity filter and the hydrophobic gate in the pore. This interdigitating stack of hydrophobic residues is positioned optimally to relay structural rearrangements to the channel gate and selectivity filter, a prediction borne out in the STIM1-mediated gating defects seen in mutants of this stack. On the other hand, the cytoplasmic side of the TM1 helix is lined by a serine ridge that is polar, flexible, and loosely packed at the interface, suggesting that this segment is allowed considerable conformational freedom in relation to the surrounding helical ring. Taken together, the functional map generated by this analysis provides a framework for understanding allosteric interactions between topologically distant domains and the global conformational changes that underlie Orai1 channel gating.

Although the study in this chapter outlines the functional importance of the TM domains in Orai1 gating, it is important to note, however, that the data in this study does not explicitly test how the STIM1 binding signal is relayed to the pore. There are several different possible mechanisms. First, as proposed by the traditional Orai1 gating model, STIM1 may be recruited to the channel via a high-affinity site at the C-terminus which allows it to interact with the N-terminus to change the pore directly (**Figure 3.18A**). In this context, the non-pore lining TMs would be passive in the gating process but needed in providing the proper environment at the TM2/3 ring interface to allow pore helix conformational changes.

Conversely, it is possible that STIM1 does not bind to the N-terminus at all as some groups have started to propose (58). The STIM1 binding site on the Orai1 N-terminus was first identified using in vitro protein fragments (26), and although the N-terminus is critical for gating (52, 55-57,

67), it is becoming increasingly uncertain whether it can interact with STIM1 in the context of an intact channel given that N-terminal region is shielded by surrounding TMs in the crystal structure. Under this model, the Orai1 C-terminal site would be the primary initiator of channel activation and this gating signal could be transmitted allosterically through the protein to the channel pore.

One possibility is the transmission of the gating signal through the intra- and extracellular loops (**Figure 3.21B**). A recent study in support of this model showed that the N-terminal cytoplasmic domain interacts with the TM2-3 loop to regulate gating (74). Since it cannot be visualized in the crystal structure of dOrai, the TM2-3 loop is presumed to be quite flexible in the

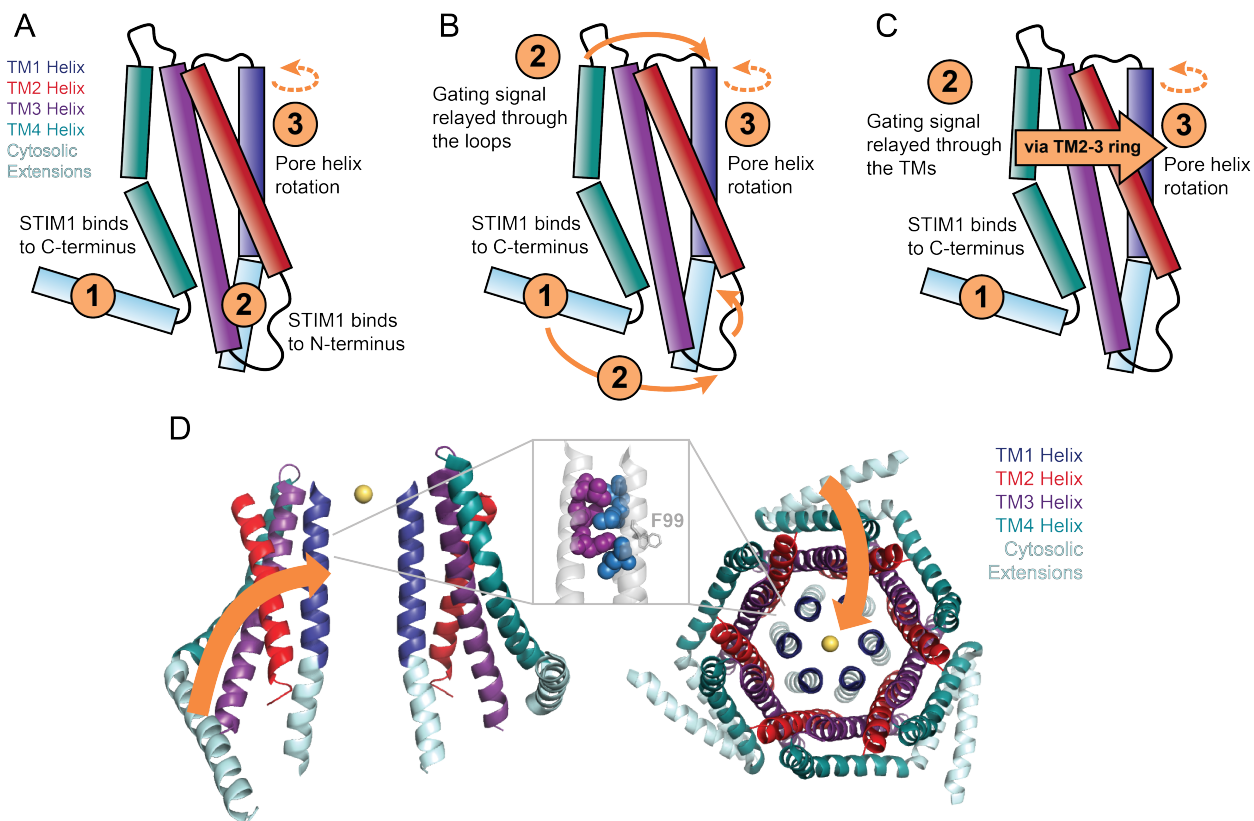


**Figure 3.18 Summary of Orai1 gating models.** (A) In model 1, STIM1 binding to the C-terminus allows for its interaction with the Orai1 N-terminus that is situated directly below the pore helix. STIM1 binding N-terminus opens the gate on TM1, while the non-pore lining helices provide the structural framework for the gating motion on the pore helix to occur. (B) In model 2, STIM1 bindings to the Orai1 C-terminus and the gating signal is transmitted through the loops to ultimately rotate the pore helix and open the channel gate. (C) In model 3, a conformational wave from the C-terminus is allosterically relayed through the TMs, from the most external TM4 through the TM2/3 ring and to the pore helix. (D) Schematic of model 3 in the context of the dOrai crystal structure.

absence of STIM1. We postulate that STIM1 would need to impart some structure to this region in order for it to play an active role in stabilizing the channel in the energetic minima corresponding to closed and open states. Another way for STIM1 binding at the C-terminus to open the pore is via a conformational wave through the TMs. One recent study has shown that a “nexus” at the base of TM3/4 can allosterically control gating (58). Moreover, the large number of GOF and LOF mutations within the TMs discussed in this chapter lead us to favor this model. Although our data does not exclude the presence of a N-terminal STIM1 interaction site, we hypothesize that a conformational wave that is initiated near the C-terminus can be transmitted through the relatively rigid TM2/3 ring to TM1 to open the channel gate (**Figure 3.21C, D**). A more specific set of conformational changes is explored later this chapter (see Future Directions).

## **Future Directions**

### **Manipulation of Orai1 activity by cross-linking TM residues**

In the early phases of this study, we attempted to manipulate interactions between residues in the TM domains via disulfide bond formation. We introduced cysteines at 12-15 different pairs of two neighboring residues that are within 2-3 Å in the crystal structure that we postulated to be cross-linkable. These include S97C/H134C, S97C/W176C, S89C/W176C, L185C/F250C, A137C/W176C, S141C/W176C, A100C/F187C, A132C/F250C, and I121C/A235C. However, attempts to modulate channel activity through disulfide cross-linking using traditional oxidizing/coordinating agents (diamide, copper phenanthroline, cadmium, t-butyl hydroperoxide, iodine, and MTSEA) and reducing agents (BMS), which have been successful in cross-linking pore residues and double cysteine mutants on the cytoplasmic surface of Orai1, have not worked for intra-TM residues thus far. It is currently not clear whether the pairs of amino acids were not

close enough to be cross-linked or if cross-linking had no effects on channel function. However, given the large number of different pairs of mutants explored and the close packing between the TMs, it is highly likely that the applied cross-linking reagents are unable to permeate into the inter-TM spaces and thus cannot modify the introduced cysteine residues.

Therefore, future attempts at cross-linking the TMs should focus on small reagents that are more likely to be able to access the TM residues of interest. Potential new strategies include the incorporation of genetically-encoded cross-linkers directly into the protein, such as mini singlet oxygen generator (mini-SOG) and photo-activated unnatural amino acids. Mini-SOG is a 106 amino-acid tag that generates singlet oxygen ( $^1\text{O}_2$ ) when illuminated by blue-light, thereby regulating the local redox environment (78, 79) (**Figure 3.19A**). Although its main applications to date are in electron microscopy sample preparation and targeted cell ablation (79), mini-SOG can in theory be used for generating reactive oxygen species to facilitate disulfide bond formation. Because  $^1\text{O}_2$  is converted to other forms of oxygen within microseconds, the effects of mini-SOG are tightly confined to its immediate surrounding locale. This provides significant benefit over bath perfusion of  $\text{H}_2\text{O}_2$  because it allows for spatial and temporal control of reactive oxygen species to limit cytotoxicity while achieving effective concentrations at the target site. Assuming that these constructs form functional Orai1 channels, cysteine mutations can be introduced to at targeted positions to attempt channel modulation via disulfide bonding.

Our collaborators (Yubin Zhou and Lian He) have created several constructs with mini-SOG inserted in the extracellular TM1-2 and TM3-4 loops (**Figure 3.19B**). Before introducing double cysteine mutants for cross-linking, we will need to confirm that these constructs express to the membrane and are able to recapitulate all the core properties of CRAC channels. One group has previously shown that WT Orai1 is sensitive to oxidation by high concentrations (1 mM) of

$\text{H}_2\text{O}_2$  at position C195 on TM3 (80, 81) and that oxidation is thought to change its interaction with S239 on TM4 to inhibit channel activity (81). Because this channel inhibition was observed in the presence of very high  $\text{H}_2\text{O}_2$  concentrations, it is unclear whether local production of  $^1\text{O}_2$  will have the same effect. However, since we currently have mini-SOG inserted into both WT and Cys3S backgrounds (all Cys residues mutated to Ser), we will be able to differentiate any effects due to oxidation of residue C195 versus introduced cysteines of interest.

Another approach is to use the photo-activated artificial amino acid p-benzoyl-L-phenylalanine (BzF or Bpa) (82), which has been shown to successfully modulate TM interactions in glutamate receptors (83). In this method, cells are transfected with several plasmids to reprogram one of the stop codons in the genetic code to incorporate BzF (82). Because of its large size, BzF (**Figure 3.19C**) is typically better tolerated at positions with endogenous Trp or Tyr

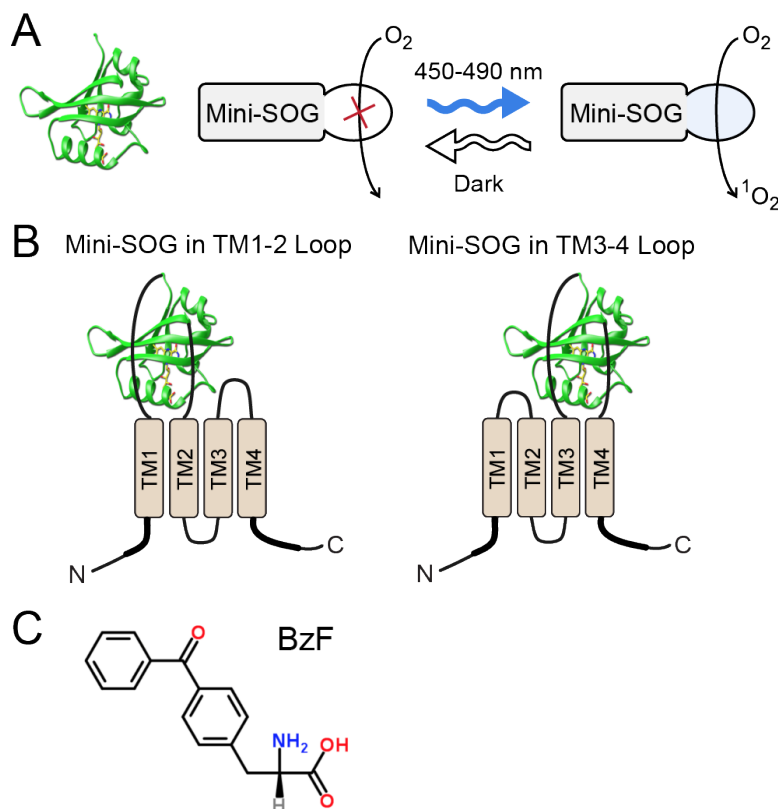


**Figure 3.19 Schematics of genetically encoded cross-linkers. (A)** Mini-SOG is a modified-LOV protein that generates singlet oxygen when illuminated by blue light. Cartoon was modified from OptoBase. **(B)** Topology diagram of Orai1 with mini-SOG inserted into the TM1-2 loop (left) or TM3-4 loop (right). **(C)** Chemical structure of artificial amino acid BzF that becomes reactive when activated by UV light. Structural diagram was taken from ChemSpider.

residues. When exposed to UV light, BzF becomes reactive and cross-links with neighboring atoms. One drawback of this approach that unlike disulfide bonding in double cysteine mutants, the interaction partner of BzF can only be narrowed into a 3-4 Å radius. Given this relative non-specificity, any gating effects observed with BzF introduced at a certain location must be validated by incorporating it at neighboring residues. On the other hand, this method only involves a single substitution and does not require the insertion of a long peptide in the middle of the channel.

### **Regulation of gating and Ca<sup>2+</sup> selectivity by the F187 Locus**

Earlier in this chapter, we showed the importance of the TM1-TM3 hydrophobic clamp in Orai1 activation. F187 on TM3 is a key component of this structural motif and is the residue that makes the most number of contacts from the TM2/3 ring to the back of TM1 (**Figure 3.13B, 3.20A**). In addition to the Ala mutation (**Figure 3.14**), we have also tested other substitutions at F187 and found that this is a crucial residue for regulating ion selectivity as well as gating. Interestingly, apart from F187I and F187W which, like F187, are large and hydrophobic, many substitutions lead to channels that are either constitutively open or display defects in gating by STIM1 (**Figure 3.20B**).

F187A/G/C channels showed inward rectifying currents with positive reversal potentials without STIM1, but exhibited different behaviors in response to STIM1. F187C displayed the most typical GOF mutant behavior, where its baseline activity can be further boosted by STIM1 to yield currents indistinguishable from WT Orai1 channels gated by STIM1 (**Table 3.1**). Despite being constitutively open at baseline, F187A channels are not significantly activated by STIM1 (**Figure 3.20B, C**). Intriguingly, F187G channels, which are relatively Ca<sup>2+</sup> selective without STIM1, become non-selective when STIM1 binds to the channel. This is reflected in its leftward

shift in  $V_{rev}$  as the current amplitude increases over time as BAPTA depletes ER  $Ca^{2+}$  stores in cells co-expressing STIM1 (**Figure 3.20B, D**). In WT channels, STIM1 boosts both channel activity and ion selectivity in a dose-dependent manner (36), implying one concerted

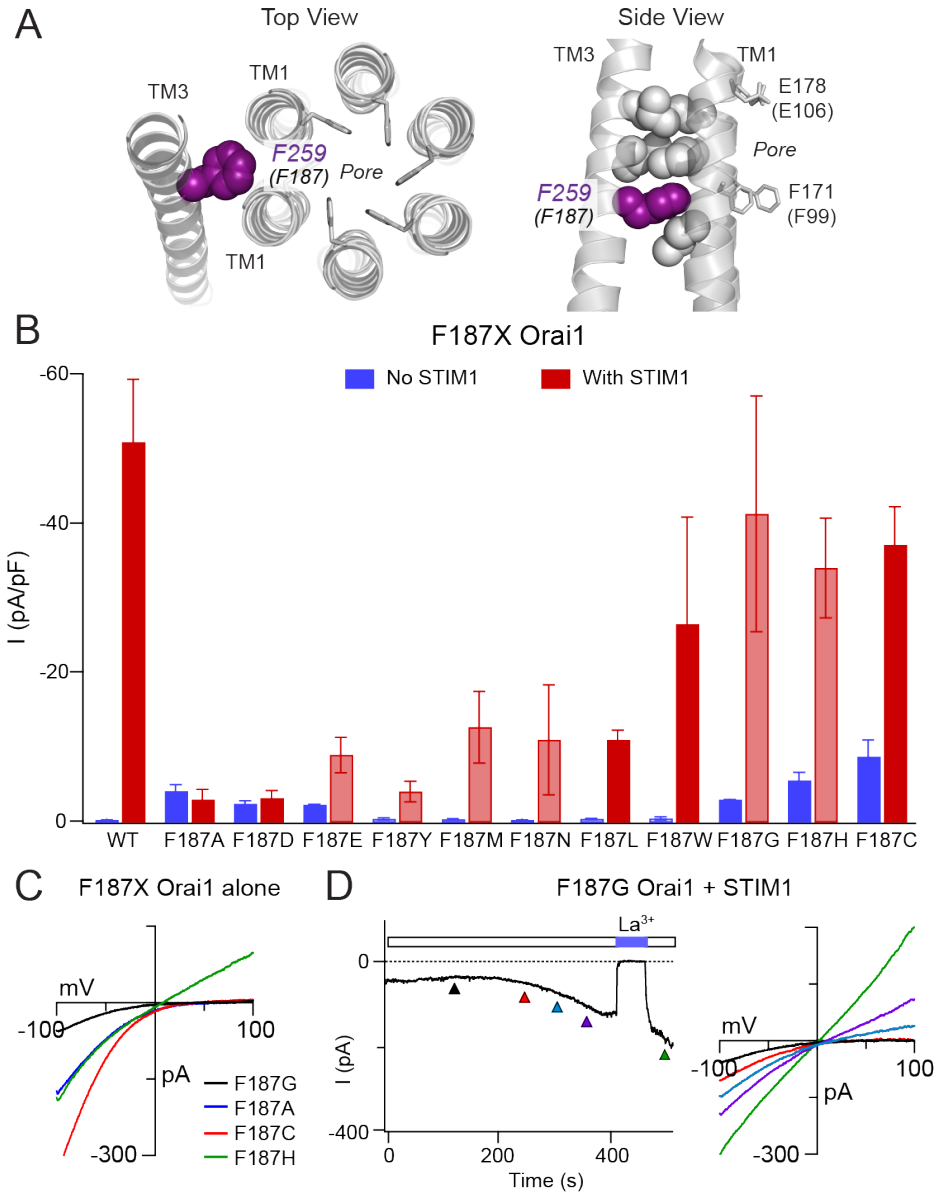


**Figure 3.20 Mutational analysis of F187 shows that it is crucial for regulating  $Ca^{2+}$  selectivity.**

**(A)** Top and side views of F259 (hOrai1 F187, purple) as part of the hydrophobic stack at the TM1-TM2/3 ring interface. **(B)** F187X mutants with and without STIM1 co-expression. Except F187L/W, all other substitutions lead to GOF or LOF channels. Values are mean  $\pm$  S.E.M. Faded bars represent mutants that yield non-selective currents in the presence of STIM1. **(C)** I-V relationships of GOF F187X mutants. F187C/A/C channels are  $Ca^{2+}$  selective, while F187H is non-selective. **(D)** Time course of F187G mutant activated by STIM1. I-V relationships at time points indicated by the colored arrowheads, showing a leftward shift in  $V_{rev}$  as the current develops.

conformational change, counter-clockwise rotation of three helical turns of TM1 (2), that underlies both opening of the F99 gate and reorientation of the selectivity filter at E106. The de-coupling between channel activation and Ca<sup>2+</sup> selectivity in the F187G mutant is unusual and suggests that in this mutant, STIM1 binding causes F99 to move away from the pore but with simultaneous loss of tight Ca<sup>2+</sup> coordination at E106. This could occur either through twisting of this region of the pore helix such that F99 moves counter-clockwise yet E106 moves in the opposite direction (helical unraveling), or pore dilation to produce a leaky channel as STIM1 binds. In addition to F187G, F187E/Y/M/N/H channels were also non-selective when activated by STIM1 (**Figure 3.20B**), further underscoring the importance of F187 for conferring Ca<sup>2+</sup> to the pore.

### **Comprehensive analysis of the serine ridge**

The serine ridge which lines the cytoplasmic portion of the TM1-TM2/3 ring interface is postulated to allow conformational flexibility in this region. Earlier in this chapter, we studied S97 in detail and found that bulky substitutions (F/Y/W) impede STIM1's ability to activate Orai1. Whether this holds true for the rest of the serine ridge (S93, S90, S89 and S82) remains to be tested. However, some promising preliminary data indicates that in line with this hypothesis, S93F/Y mutations also lead to LOF phenotypes (data shown in Chapter 4). In addition to its role in allowing conformational flexibility and its interaction with the polar regions of the TM2/3 ring, the serine ridge may also contribute to the presence of water in crevices behind the pore helix (described further in Chapter 5).

### **Functional significance of the TM2/3 ring and its interface with TM4**

In this chapter, the roles of the hydrophobic cluster and serine ridge at the TM1-TM2/3 ring interface were experimentally validated. However, the packing interfaces between intra- and inter-subunit TM2 and TM3 neighbors forming the TM2/3 ring its interface with TM4 were not examined. Because the STIM1 binding site at the Orai1 C-terminus contributes to gating, all of the TMs, including the most distally-located TM4, are likely to be active participants in the allosteric relay of conformational changes from the C-terminus to the central pore.

The TM2/3 ring is formed by six TM2 helices intertwined with six TM3 helices from neighboring subunits, and the TM2/3 helices display substantially more contacts and a more uniform packing density across their interfaces than do either TM1 or TM4. Each helix of the TM2/3 interface packs against two neighbors. The packing of the TM2 to the TM3 of the same polypeptide chain has characteristics of a coiled helix pair; the residues of TM2 involved in the contact are almost entirely hydrophobic, and the leucine-rich packing interactions along the face are characteristic of the classic “knobs into holes” motif. Interestingly, residues of TM3 involved in the contact include a “GAS” dimerization motif formed by A247, S251, and G255 (hOrai1 A175, S179, and G183) that is common in membrane proteins, with G255 forming the central residue of the interface, thus allowing an unusually close helix axis to axis distance of 8.5 Å. We can infer that this intramolecular TM2/TM3 interface, in which 21 out of 23 packing interactions are hydrophobic, is relatively rigid. On the other hand, although the intermolecular adjacent TM2/TM3 helix to helix interface is less closely packed than the intramolecular pair, this interface is also leucine-rich and almost completely hydrophobic. The side chains exhibit classic 4/3 “ridges into grooves” packing, in which hydrophobic  $n/n+4$  ridges of TM3 rest in grooves defined by residues related by  $n/n+3$  on TM2. Overall, the extensive hydrophobic contacts extending across

the majority of TM3 on either side of TM2 revealed by the contact dots analysis thus suggests that the TM2/TM3 helices are tightly packed against each other. To examine the functional significance of this unique packing of the TM2/3 ring, we have made Ala and Trp mutants of all the residues lining the TM2/3 interfaces that currently await testing. We predict that some of these will lead to GOF or LOF channels by disrupting the structural integrity of the TM2/3 ring.

Likewise, the interface between the TM2/3 ring and TM4 is also mostly lined by interdigitating hydrophobic amino acids making numerous contacts (**Figure 3.21**). The residues with the most number of contacts forming the “anchors” at this interface are Y243 and W268 (hOrai1 H171 and W196) on TM3 and L286 and F293 (hOrai1 M243 and F250) on TM4. With the arrangement of TMs 2 and 3 in the dOrai structure as an interlocked ring wedged between TM4 and TM1, we postulate that the TM2/3 ring functions as a rigid unit to relay gating information from the outer surface

of Orai1 to the central TM1 pore helix bundle. We have also made various large and small substitutions at these positions to test their contributions to gating (see next section regarding testing of gating model derived from MD simulations).

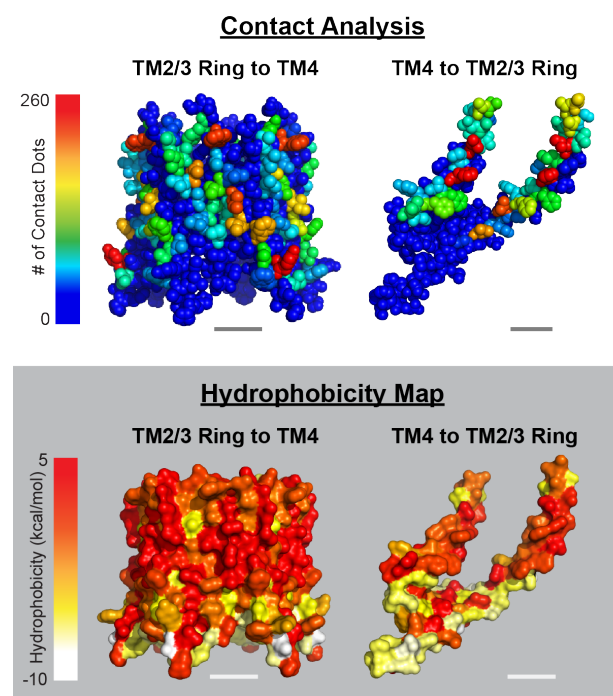


**Figure 3.21 Atomic packing analysis and hydrophobicity map of the TM2/3 ring to TM4 interface.** The majority of this interface is lined by large, hydrophobic residues that are tightly packed against each other. (Atomic packing analysis was performed by Douglas Freymann).

### **Experimental validation of the conformational changes detected in MD simulations**

The study described earlier in this chapter was focused on the mapping the regions within the TMs that mediate Orai1 channel activation. However, the global conformational changes that occur during gating remain elusive. One potential clue arises from the MD simulations of the GOF H206S/C channels, which currently represent the closest surrogates for the STIM1-activated state. As described above, the MD simulations are able to recapitulate several core features of H206S/C mutants such as pore helix rotation and the increased pore hydration allowing for ion conduction, providing confidence that the conformational changes in TMs 2-4 in these simulations are likely to be relevant and informative. As highly dynamic molecules, proteins exhibit countless high-frequency fluctuations over nanosecond time scales, resulting in a tremendous amount of data, and while these granular motions are important, extensive analysis of the entire dataset requires a substantial amount of computational power. Thus, to get a simplified picture of how the positions of the TMs differ among the various mutants, we performed atom-by-atom averaging of 60 dOrai monomers of each mutant sampled from ten different independent simulation runs. Because the positions of the atoms are averaged, information about the relative distributions of different conformations and the rotameric orientations of the side chains cannot be retained. Nevertheless, this method provides useful preliminary information about the conformational changes in the helical backbones of Orai in WT, GOF and LOF mutants.

On a macroscopic level, the entire GOF H206C hexameric channel is expanded 3-4 Å in diameter compared to WT (**Figure 3.22A**), suggesting that H206 at the TM1-TM2 interface locks a channel in a constrained resting state that relaxes in the H206C activated channel. The finding that a single point mutation has such drastic effects on the global conformation of Orai1 further

bolsters the idea that H206 acts as a brake at the intersection of TMs 1-3 and supports the idea of a highly allosteric mechanism for channel gating as proposed earlier in this chapter.

In order to identify conformational differences in between WT and H206C on a monomeric level, we aligned the averaged WT monomer structure with H206C by minimizing RMSDs over the TM2 helices (**Figure 3.22B**). Alignment was performed across this region because it is the most rigid portion of the channel as part of the TM2/3 ring (as noted earlier in this chapter) and undergoes relatively small fluctuations, allowing us to observe relative intra-subunit changes in the TM1 and TM4. This analysis revealed several noteworthy differences between the two structures. There appears to be a 1-2 Å “drop” of TM1 relative to TM2 that is caused by a slight shearing motion at the TM1-TM2 interface (**Figure 3.22B**). This motion is associated with dilation of the pore near the external mouth of the channel. In the context of STIM1-mediated gating, STIM1 binding to the distal TM4 regions may be responsible for shifting the TM4 helices outwards. Next, because TM4 is packed tightly against the TM2/3 ring (**Figure 3.21**), this shift in TM4 could in turn expand the TM2/3 ring to allow for pore helix rotation and external pore dilation (**Figure 3.22D**). These ideas remain to be validated by mutational analysis. For example, mutations that disrupt the TM4 to TM2/3 ring interface would be expected to abrogate Orai1 gating by STIM1 (e.g. see A235 mutants below). Alternatively, in addition to structure-function analysis using patch clamping, use of other biophysical approaches to monitor conformational changes in these regions (e.g. smFRET, LRET, DEER) during gating could also be potentially informative.

Our lab previously identified pore helix rotation as part of the Orai1 gating mechanism (2). Because STIM1 binding causes F99 side chains to move away from the pore and imparts Ca<sup>2+</sup> selectivity to Orai1, pore helix rotation is presumed to at least involve the region encompassing the three turns from F99 to E106 (2). However, it is not known whether the entire TM1 helix

rotates as a rigid body or if the rotation is localized to the hydrophobic stretch. We examined this by aligning TM1 in WT vs. H206C structures to eliminate confounding effects from the TM1-TM2 shearing. Based on the averaged structures of WT vs. H206C simulations, counter-clockwise rotation of the pore helix appears to be limited to the external region, with the inner pore remaining

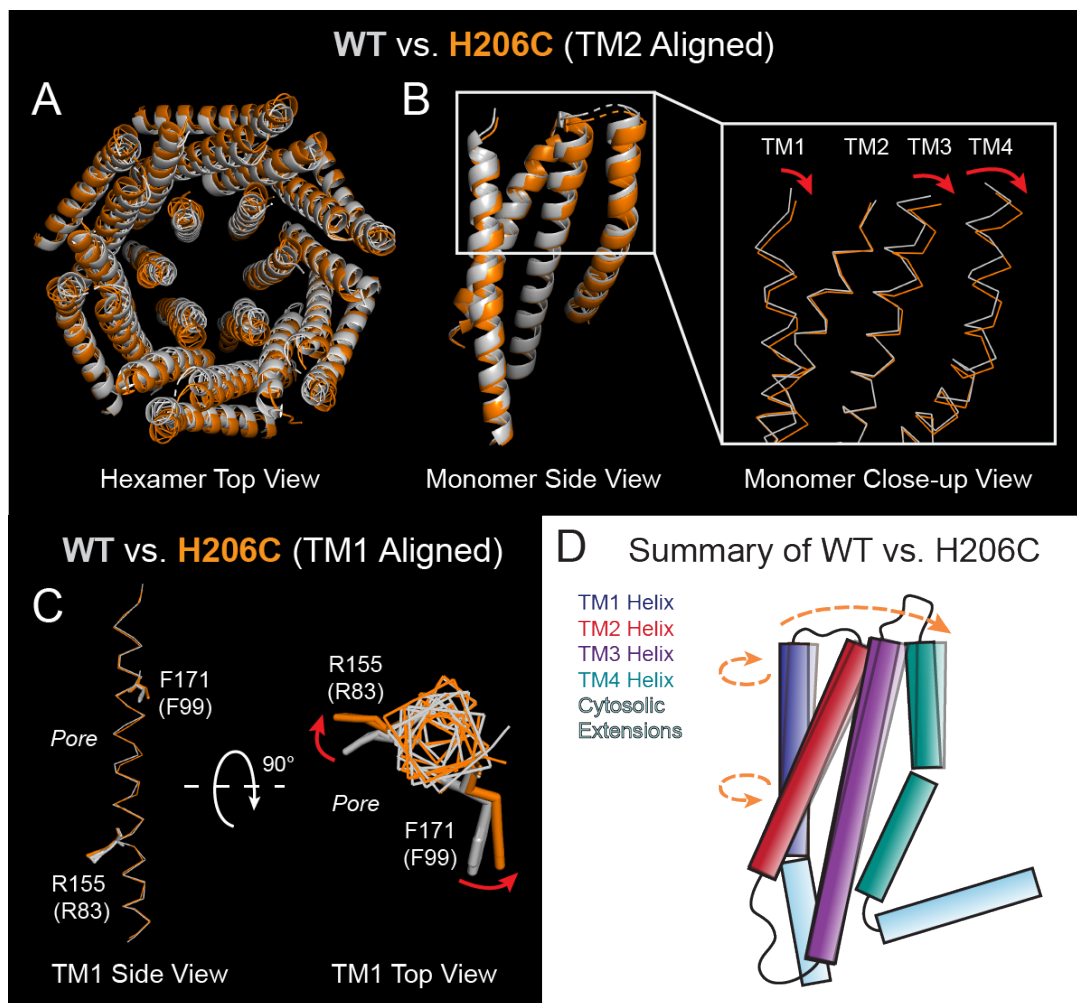


**Figure 3.22 Averaged structures of MD simulations reveal conformational differences between WT dOrai and the H206C activated mutant. (A)** Compared to the WT channel (grey), the H206C (orange; hOrai1 H134C) channel is expanded towards the extracellular side. The hexamer is aligned at the center of the pore. **(B)** Monomer view aligned at TM2 to reveal the relative motions within the TMs of each monomer. Relative to TM2, TMs 1, 3, and 4 shift outward and downwards, which is predicted to expand the outer mouth of the pore. **(C)** TM1 aligned between WT and H206C averaged structures. The extracellular region of TM1 (near F99) is rotated counter-clockwise, while the intracellular portion (near R83) rotates slightly clockwise, suggesting a twisting motion of the pore helix. **(D)** Cartoon of conformational changes in H206C MD simulations relative to WT. (MD simulations performed by Christopher Ing, and atom-by-atom averages were generated by Douglas Freymann.)

mostly unchanged or perhaps even rotated slightly clockwise (**Figure 3.22C**). This unanticipated twisting motion in the pore helix could potentially implicate G98 in the middle of the helix acting as a pivot point. Further, it is likely that differences in packing and hydrophobicity of the hydrophobic cluster and serine ridge at the TM1-TM2/3 ring interface mediates these differences in rotation of the extracellular and intracellular regions of TM1.

### **Mutational analysis of the A235 locus at the TM4-TM2/3 ring interface**

A235 was identified as a potentially important region for gating based on the constitutive activation of A235C identified from the cysteine screen (**Figures 3.1, 3.2**). From the H206C MD simulations, we hypothesize that STIM1 binding at the C-terminus could cause outward tilting of TM4 which gets translated through the TM2/3 ring to dilation of the outer pore in TM1. Given its position at the top of the TM4-TM2/3 ring interface and small size (**Figure 3.23A**), we wondered if mutating Ala to larger residues would prevent the channel from “expanding”. Indeed, A235W and to some extent, A235H/Y channels inhibit channel gating (**Figure 3.23B, D**), which supports the idea that flexibility at the top of TM4 is important for STIM1-mediated activation. We also attempted to acutely modulate channel activity by applying MTS reagents onto A235C channels, with the expectation that increasing the size of the side chain will inhibit the current. Unfortunately, application of MTS reagent did not alter the current amplitude, potentially due to shielding by the extracellular loops that prevents reagents from accessing this area.

Of note, like Cys, Asn and Met substitutions also lead to GOF channels (**Figure 3.23C**). It is not clear, however, how these mutations lead to constitutive activity, given that A235S, which only has one atom different from A235C, retains store-operated behavior (**Figure 3.23B**). It

appears that both the maintenance of the closed resting state as well as transition to the open state, are dependent on the small size of A235.

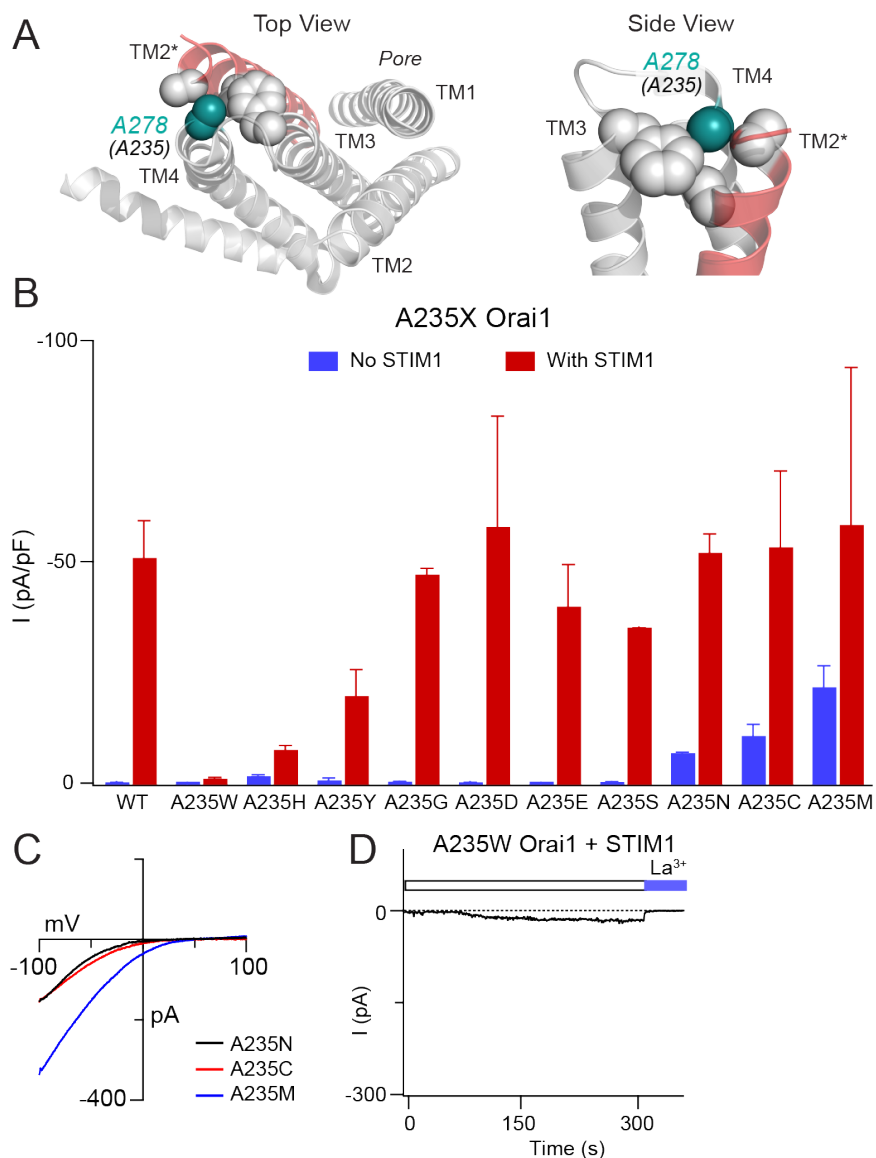


**Figure 3.23 The small size of A235 is required for maintaining the closed and open states.**

**(A)** Top and side views of A278 (hOrai1 A235, teal) at the TM4-TM2/3 ring interface. Top view of the dOrai monomer with TM2 from a neighboring indicated as TM2\* in red. Side view of A235 with TM4, TM3 from the same subunit, and TM2\* shown for clarity. Note: the side chain of I121 at the top of TM2\* is not fully resolved in the 4HKR structure. **(B)** A235X mutants with and without STIM1 co-expression. A235N/C/M mutations lead to GOF channels, while A235W cannot be activated by STIM1. Values are mean  $\pm$  S.E.M. Error bars not shown for samples with fewer than three cells. **(C)** GOF mutants A235N/C/M show inward rectifying I-V relationships. **(D)** Lack of current development over time by BAPTA in Orai1 A235W in the presence of STIM1.

## CHAPTER 4: ACTIVATION OF THE ORAI1 CHANNEL GATE IS REGULATED BY A PORE HELIX BRACE FORMED BY TM2

*(Manuscript in preparation)*

### **Introduction**

To date, there have been reports of several different gain-of-function (GOF) mutations in Orai1 that lead to elevated  $[Ca^{2+}]_i$  levels in unstimulated cells due to the constitutive activation of SOCE (13-16). The chronic  $Ca^{2+}$  entry resulting from these mutations causes tubular aggregate myopathy with additional accompanying symptoms dependent on the specific mutation (13-16). Potential pore opening mechanisms of several of these GOF human mutations have been proposed (2, 44, 55) (including S97C in the previous chapter), but little is currently known about how L138F causes channel activation. In this study, we examined the mechanism by which this mutation leads to a constitutively open pore as well as broader implications for Orai1 activation and inactivation.

### **Results**

#### **Human mutation Orai1 L138F on TM2 opens the pore through steric clash with TM1**

Orai1 L138F was inferred as a GOF Orai1 mutation on the basis of constitutive  $Ca^{2+}$  influx observed using Fura-2  $Ca^{2+}$  imaging, but its properties have not been assessed by electrophysiology. To directly test whether the L138F mutation causes opening of CRAC channels, we overexpressed this mutant in HEK293 cells and analyzed the CRAC current by whole-cell mode patch-clamping. Indeed, unlike WT Orai1, the expression of L138F produces a constitutively active current in the absence of STIM1 (**Figure 4.1B**). This current was consistent with Orai1 channels (rather than an unrelated current) based on several criteria including blockade by  $\mu M$  concentrations of  $La^{3+}$ , an inwardly rectifying I-V relationship, and permeation of  $Na^+$  ions

in divalent-free solutions. Unlike many other constitutively open Orai1 mutants (**Figure 3.2**), Orai1 L138F conducts a much larger  $\text{Na}^+$  current compared to  $\text{Ca}^{2+}$  current (**Figure 4.1B**), possibly reflecting a difference in the conformation in the pore regions controlling ion permeation.

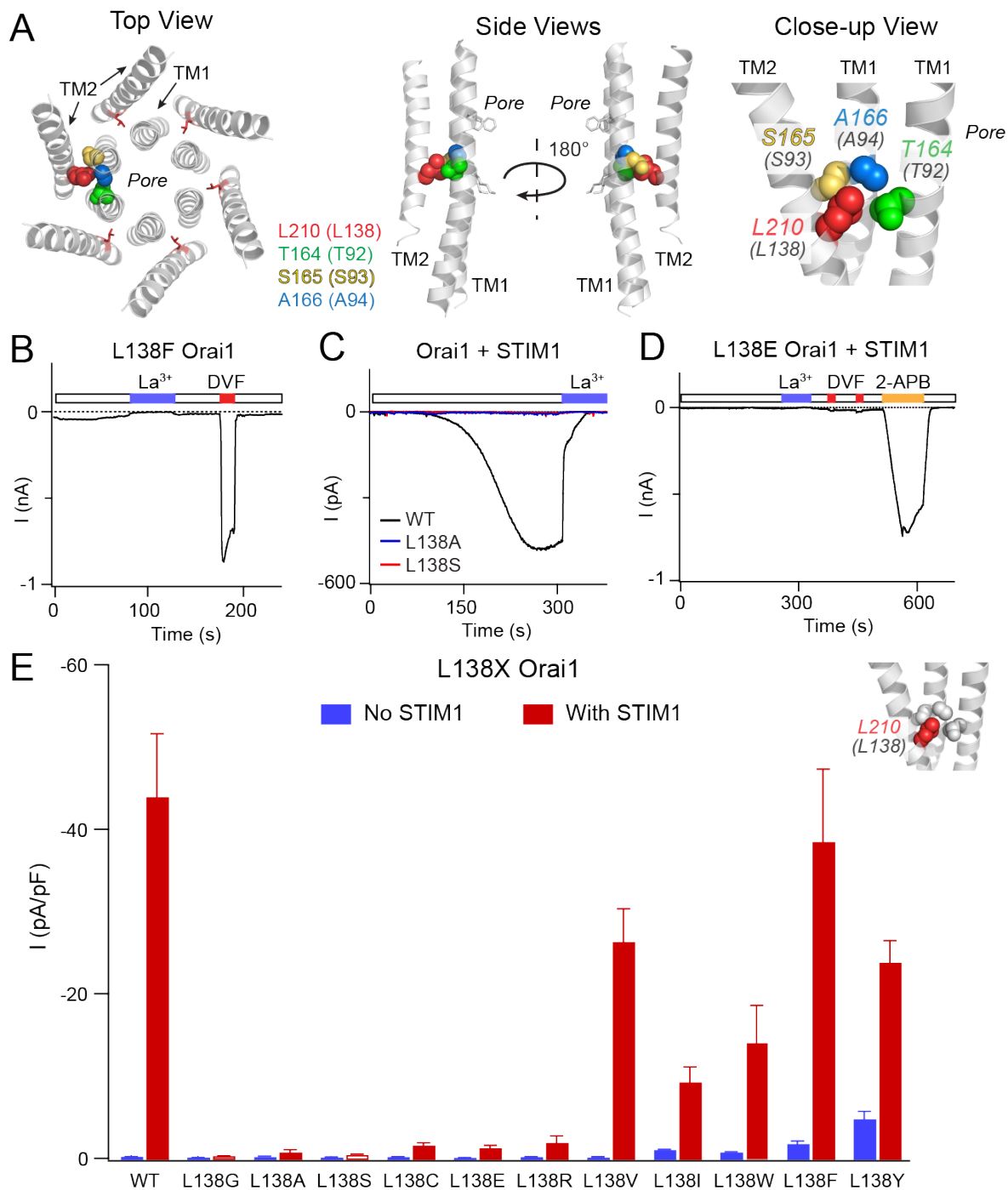


**Figure 4.1 Activity of L138 mutants depends on the size and shape of the introduced side chain.** (A) Top, side, and close-up views of L210 (hOrai1 L138, red) in the dOrai crystal structure surrounded by TM1 residues T164 (hOrai1 T92, green) from a neighboring subunit, and S165 (hOrai1 S93, yellow) and A166 (hOrai1 A94, blue) from the same subunit. For reference, F171 (hOrai1 F99) and K163 (hOrai1 R91) pore residues are shown as grey sticks. (B) Time course of L138F Orai1 showing constitutive current without STIM1. There is detectable current in 20 mM  $\text{Ca}^{2+}$  external solution at whole-cell break-in ( $t=0$ ) and a large  $\text{Na}^+$  in DVF solution. (C) Unlike WT Orai1, L138A and L138S mutants do not show current induction over time with STIM1 co-expression. (D) L138E LOF mutant is not gated by STIM1 but can be activated by 50  $\mu\text{M}$  2-APB. (E) The current densities of L138X mutants in the absence of STIM1 co-expression. Small and flexible substitutions produce LOF channels while L138F/Y channels are open without STIM1.  $N = 2-6$  cells. Values are mean  $\pm$  S.E.M. Inset shows position of L138 in 4HKR.

The dOrai crystal structure shows that L138 on TM2 protrudes towards the non-pore-lining surface of TM1 (**Figure 4.1A**), suggesting that replacing the leucine with the bulkier phenylalanine could distort the pore by pushing against TM1. To examine this possibility, we mutated L138 to other residues of different sizes and shapes to assess the contribution of steric effects at this residue (Fig. 5) by examining their phenotypes with and without STIM1. Mutation of L138 to large amino acids with benzene rings such as Phe and Tyr, produced constitutively open channels, but mutation of L138 to smaller amino acids did not cause gain-of-function (**Figure 4.1E**). These results suggest that the introduction of large side chains at L138 (F, Y) likely leads to steric clash of the exogenous side-chains with residues in TM1, causing channel activation. Of note, mutation of L138 to His or Trp (not shown), which are both larger than Leu, did not significantly increase baseline activity, suggesting that the channel is more sensitive to a benzene ring at this position than an imidazole ring.

Intriguingly, substitution of L138 to small amino acids such as Gly, Ala, Ser, and Cys were unable to be activated by STIM1, resulting in a LOF phenotype (**Figure 4.1C**). Mutations of L138 to Arg and Glu, which are long but flexible, also yield Orai1 channels with significantly diminished currents (**Figure 4.1D**). The loss of function in these channels is not due to protein misfolding or mistargeting, as confocal images reveal that they are able to recruit CAD to the

membrane. Further, L138E, which cannot be gated by STIM1, can be activated by the small molecule CRAC channel activator 2-APB, indicating that the mutation disrupts the STIM1-specific gating pathway as opposed to abrogating the channel's ability to open.

Overall, this data raises the possibility that this leucine residue acts as a “lever” pushing on the back of TM1 to relay gating information from TM2 to the TM1 pore. In the LOF mutants, STIM1 presumably activates the conformational switch at L138, yet due to the small side-chain, it is unable to reach its interaction partner to relay the gating information to the pore. Although Arg and Glu have large overall surface areas, their long flexible chains may hinder its action as an effective lever to relay the gating signal to TM1.

### **Double mutants demonstrate interaction between L138 and T92**

The crystal structure of dOrai shows three residues on the non-pore-facing side of TM1 within 2-3 Å of L138: T92, S93, and A94 (**Figure 4.1A**). Because L138F likely causes steric hindrance with one of these three residues to cause constitutive channel activation, we tested whether or not relieving this clash by introducing a Gly substitution at these positions could reverse its GOF phenotype. We found that while the addition of a A94G (and to a lesser extent, S93G) mutation to the L138F channel does not alter its GOF phenotype, T92G/L138F channels are not constitutively active (**Figure 4.2A, B**). This finding suggests that L138F is open due to steric clash with T92 on TM1 of a neighboring subunit.

Next, we aimed to test whether artificially enhancing the interaction between L138 with T92 could restore the channel activity of the LOF L138C mutant. To address this question, we generated double cysteine mutants in the L138C background by introducing T92C, S93C, or A94C. As described above, L138C channels cannot be activated by STIM1 due to its small side chain

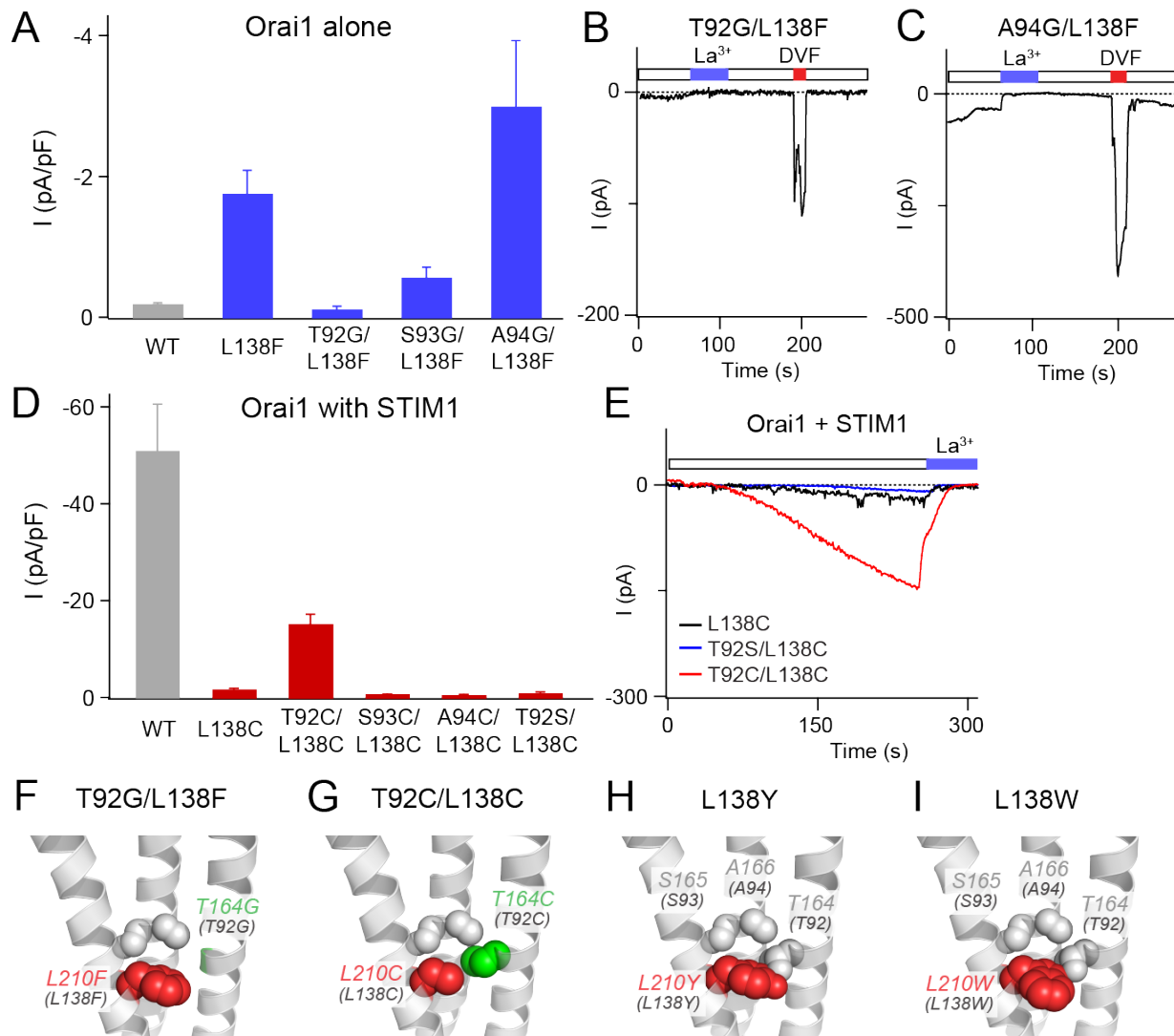


**Figure 4.2 L138-TM1 double mutants suggest that L138 interacts with T92.** (A) Orai1 L138F GOF phenotype is reversed by the addition of a T92G mutant, but not A94G. (B) Orai1 T92G/L138F is not constitutively open. (C) Like the L138F single mutant, A94G/L138F shows current without STIM1. (D) Orai1 L138C LOF phenotype can be partially reversed by the addition of a T92C mutation that can potentially form a disulfide bond with L138C. T92S/L138C channels remain unable to be activated by STIM1. (E) Store-operated gating by STIM1 in L138C can be partially rescued by the addition of T92C, but not T92S. (F) Cartoon of the T92G/L138F double mutant showing that T92G mutant relieves the steric clash caused by L138F. (G) Cartoon of the T92C/L138C mutant. (H, I) Cartoons of L138Y and L138W mutants. L138A decreases the contact between L138 and TM1. While the L138W side chain is larger than L138Y, L138Y has more steric clash with T92 due to the position of its phenol ring.

size. Intriguingly, however, while S93C/L138C and A94C/L138C channels remained unable to be gated by STIM1, T92C/L138C channels were store-operated (Figure 4.2C, D). This suggests that an interaction between T92C/L138C facilitates store-operated Orai1 activation. Consistent

with the notion that the formation of a disulfide bond between T92C and L138C enables channel gating, T92S/L138C channels, which only have one cysteine and cannot form a disulfide bond between these residues, cannot be activated by STIM1 (**Figure 4.2C**). Unfortunately, attempts at manipulating this disulfide bond through redox reagents were unsuccessful, potentially due to the inability of large reagents to access this region of the channel. (For a more detailed explanation, see Chapter 4 Future Directions.) However, because the potential interaction between T92 and L138 is between two neighboring subunits rather than an intra-subunit interaction, we can verify formation of an inter-subunit disulfide bond using Western blotting. If the rescue of gating is indeed dependent on this covalent bond, we would expect to see dimeric Orai1 bands in the T92C/L138C mutant and monomeric bands in T92S/L138C channels.

Finally, consistent with the idea that L138F/Y causes steric clash with T92, when the Leu side chain at position 210 (hOrai1 L138) is replaced with the most probable rotamer of Tyr in the crystal structure of dOrai, there is substantial steric clash of L210Y (hOrai1 L138Y) with residue T164 (hOrai1 T92) on the back of TM1 (**Figure 4.2G, H**). Interestingly, due to a difference in the position of the six-membered ring in Trp, L210W (hOrai1 L138W) exhibits less steric clash with T164 and is accordingly less constitutively active (**Figure 4.1E**).

### **Mutations at T92 phenocopy GOF L138 mutations**

Because L138F causes steric clash with T92, we asked whether substituting large amino acids at position T92 also produces GOF channels, perhaps in part through interference with L138. Consistent with this hypothesis, T92V/L/F/Y/W mutants were open in the absence of STIM1, while mutants with small, polar substitutions (G/A/S/C) retained store-operated behavior (**Figure 4.3A**). This suggests that steric clash between T92 on TM1 with neighboring residues, including

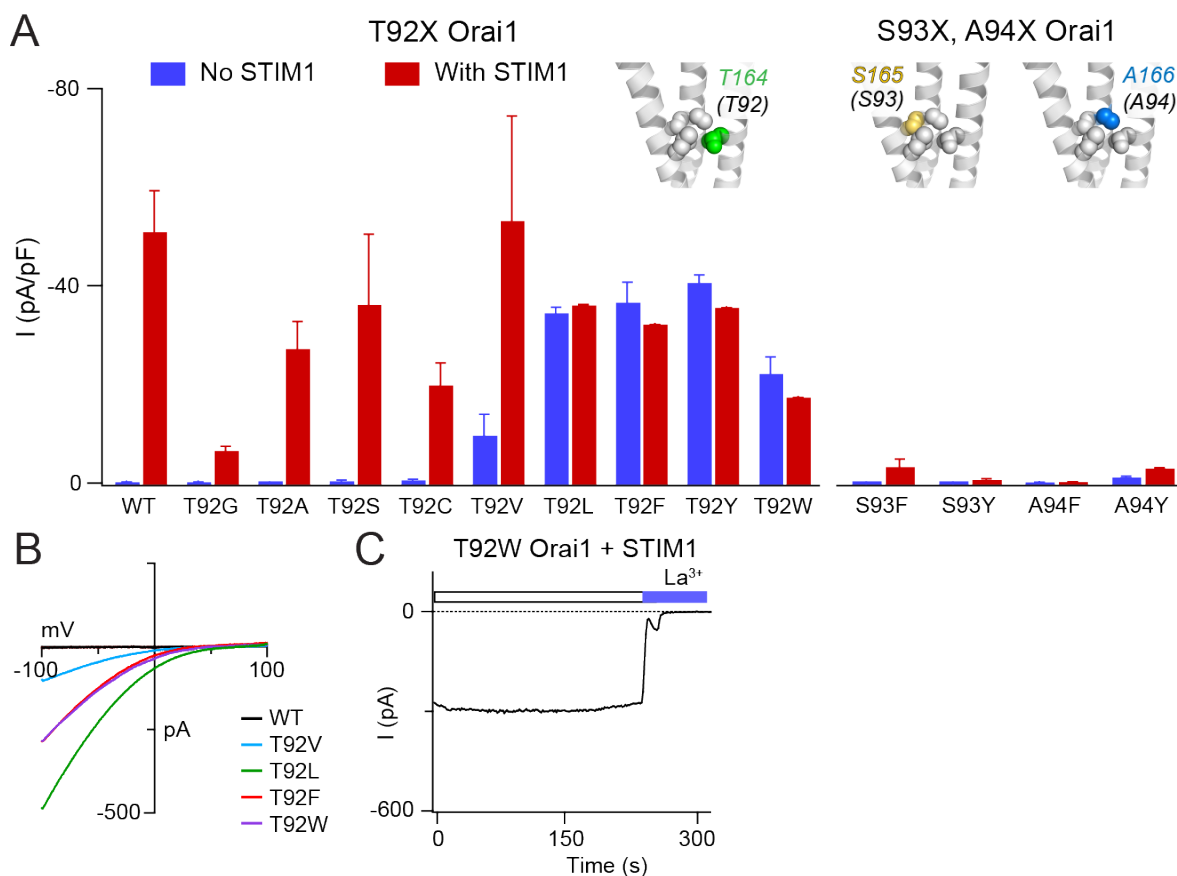


**Figure 4.3 Large substitutions at T92, but not S93 or A94, cause constitutive Orai1 activation.** (A) The current densities of T92X mutants in the absence of STIM1 co-expression. Bulky substitutions at T92 cause GOF channels, while large amino acids at positions S93 and A94 do not cause constitutive channel activation. Insets show positions of T92, S93, and A94 in the 4HKR structure. N = 2-6 cells. Values are mean  $\pm$  S.E.M. (No error bars are shown for mutants with less than 3 cells.) (B) I-V relationships of GOF T92X channels. T92V/L/F/W mutants show inward rectifying I-V curves with positive reversal potentials, similar to STIM1-activated WT Orai1 channels. (C) STIM1 does not significantly boost the current amplitude of GOF T92W Orai1 channels, suggesting that this mutant is nearly fully active at baseline.

L138, lead to GOF phenotypes. We can further test this idea using a T92F/L138G mutant, which would be predicted to relieve this strain and restore the closed resting state. In addition, the T92F/Y GOF channels displayed larger currents in 20 mM Ca<sup>2+</sup> external solution compared with L138F/Y channels. Because Thr is smaller than Leu (side chain surface areas of 140 Å<sup>2</sup> and 170 Å<sup>2</sup> respectively), replacing it with bulky residues is predicted to cause more steric clash at the TM1-TM2 interface. Consistent with this higher baseline activity, while STIM1 co-expression substantially activates L138F/Y channels, T92F/Y are not noticeably further activated following

whole-cell break-in, similar to H134A/C/S/T channels (**Figure 4.3C**). On the other hand, S93F/Y and A94F/Y channels are not constitutively open, further supporting the idea that the L138F GOF phenotype arises from its interaction with T92 and not S93 or A94 (**Figure 4.3A**). Instead, large substitutions at S93 and A94 lead to LOF phenotypes, potentially by disrupting the conformational flexibility of the TM2-TM1 interface needed at the serine ridge, a possibility warranting further exploration (**Figure 4.3A**).

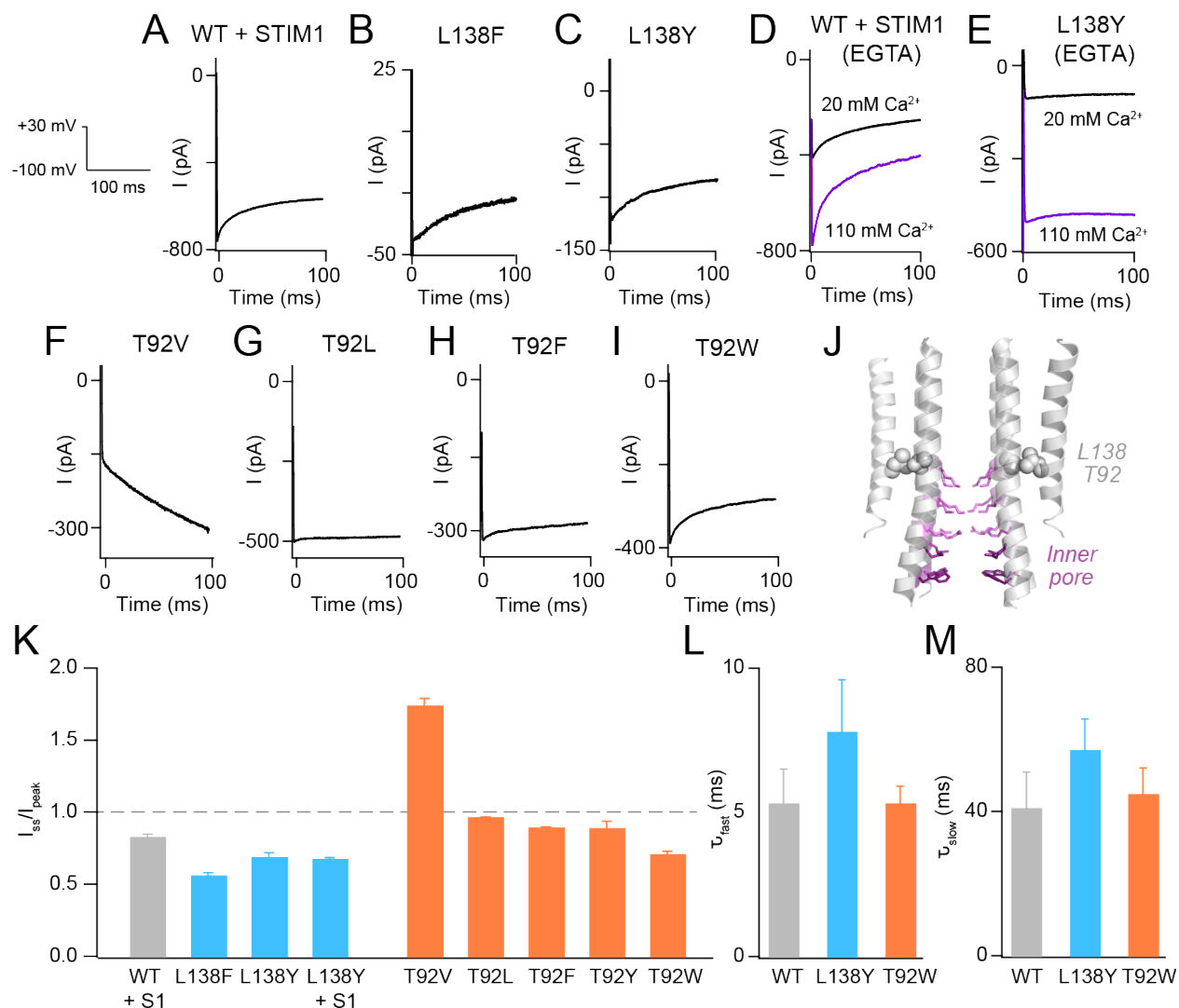
### **STIM1-independent inactivation of L138F/Y and T92F/Y/W channels**

Fast  $\text{Ca}^{2+}$ -dependent inactivation (CDI) is a unique feature of Orai1 channels in which  $\text{Ca}^{2+}$  flux driven through Orai1 at hyperpolarizing potentials (e.g. steps to -100 mV) causes a negative feedback mechanism to inactivate the channel on a timescale of tens to hundreds of milliseconds (8, 29, 84, 85) (**Figure 4.4A**). WT Orai1 channels inactivate with a fast component and a slow component with  $\tau$  of  $5 \pm 1$  ms and  $40 \pm 10$  ms respectively (**Figure 4.4L, M**). Fast CDI is thought to be regulated by a  $\text{Ca}^{2+}$  sensing site located nanometers away from the channel based on the varying degrees of inactivation in BAPTA- vs. EGTA-based internal solutions which chelate  $\text{Ca}^{2+}$  at different rates (85) (**Figure 4.4A, D**). Although the precise mechanism of CDI is not known, it is thought to involve coupling between the inactivation domain (residues 470-491) of STIM1 (65, 86, 87) with the inner pore (residues 76-91) of Orai1 (88) (**Figure 4.4J**). In line with the established requirement for STIM1 in CDI, GOF Orai1 mutants typically do not inactivate without STIM1, but instead show potentiation over the 100-ms step (**Figure 3.3**) (58).

In contrast to other GOF mutants, however, Orai1 L138F/Y and T92F/Y/W GOF mutants exhibit a time-dependent decline in current during hyperpolarizing steps. The extent and kinetics of this current decline appears to be macroscopically similar to fast CDI (**Figure 4.4**). As with

WT Orai1 channels gated by STIM1, L138F/Y and T92F/Y/W channels inactivate (10-30%)

during a hyperpolarizing 100-ms step from +30 mV to -100 mV (**Figure 4.4K**). Moreover, the



GOF mutants inactivate with comparable kinetics, with  $\tau_{\text{fast}}$  and  $\tau_{\text{slow}}$  not significantly different from STIM1-gated WT channels (**Figure 4.4L, M**).

Because the inactivation in L138 and T92 mutants develop over tens of milliseconds in response to hyperpolarization (**Figure 4.4**), it appears to be either  $\text{Ca}^{2+}$  and/or voltage-dependent. Consistent with the notion that the inactivation is  $\text{Ca}^{2+}$  dependent, these mutants do not show inactivation in DVF solutions (not shown). To confirm this, we exchanged the usual BAPTA-based internal solution to an EGTA one, which due to its slower chelating rate, is expected to increase the local  $[\text{Ca}^{2+}]$  at the mouth of the pore. However, it is puzzling that unlike STIM1-gated Orai1 channels (**Figure 4.4D**), L138Y channels did not inactivate more in the presence of EGTA compared with BAPTA (**Figure 4.4E**). Moreover, increasing the  $\text{Ca}^{2+}$  in the external solution from the usual 20 mM to 110 mM  $\text{Ca}^{2+}$  also did not increase the extent of inactivation (**Figure 4.4E**). This suggests that L138F/Y mimics some aspects of WT channels during CDI, but may not be as sensitive to changes in local intracellular  $\text{Ca}^{2+}$ .

Interestingly, in T92 GOF mutants, the extent of inactivation during the hyperpolarizing step is correlated with the size of the introduced side chain. T92V shows potentiation similar to other GOF mutations (**Figure 4.4F**), while T92L (5%), T92F/Y (10-12%), and T92W (28-30%) exhibit increasing amounts of inactivation (**Figure 4.4G-I, K**), implying that like activation, Orai1 inactivation may also be induced through steric clash between L138 and T92. The presence of STIM1-independent inactivation of L138X and T92X mutants implies the L138-T92 locus may be an important node for regulating fast CDI in STIM1-gated Orai1 channels (see Discussion).

## **Discussion**

A recent report demonstrated that human mutation Orai1 L138F causes tubular aggregate myopathy associated with hypocalcemia in patients. This syndrome is driven by dysregulated  $\text{Ca}^{2+}$  signaling in muscle cells secondary to constitutive  $\text{Ca}^{2+}$  entry through open CRAC channels. In this study, we aimed to understand the underlying mechanism of this mutation and determined that steric clash between L138F and T92 on TM1 drives constitutive Orai1 activation. Mutations on either L138 or T92 that increase the amount of contact between these two residues cause GOF, presumably because steric clash disrupts the closed state of the pore. By contrast, mutations that reduce the packing density at this interface such as small or flexible substitutions at L138 lead to LOF. This pattern of phenotypes suggests that L138 acts as a lever at the TM2-TM1 interface and contributes to conformational changes in the pore that mediate channel activation.

Interestingly, the dependence of side chain size at L138 on Orai1 channel activity is the opposite of that at position H134 located one helical turn above it (**Figure 4.5A**). In general, at L138, introduction of bulky amino acids (F/Y) yield GOF channels, whereas small or flexible residues (G/A/S/C/E/R) lead to LOF channels. As described in the previous chapter, the opposite is true for H134, where small or flexible substitutions (A/S/T/C/M/E) cause constitutive activity and large ones (K/F/Y/W) impede STIM1-mediated gating. The location of these two amino acids along with the opposite dependence of channel activity on side chain size implies that these two residues may be complementary in their effects in stabilizing the conformation of the pore helix by acting as a brace (**Figure 4.5A, B**). In this context, “pushing” at L138 through large amino acids and “pulling” at H134 through small substitutions both lead to channel activation, while “pulling” at L138 or “pushing” at H134 abolishes channel function. Although speculative, this pattern also raises the possibility that during STIM1-mediated gating, TM1 is pushed by L138 and

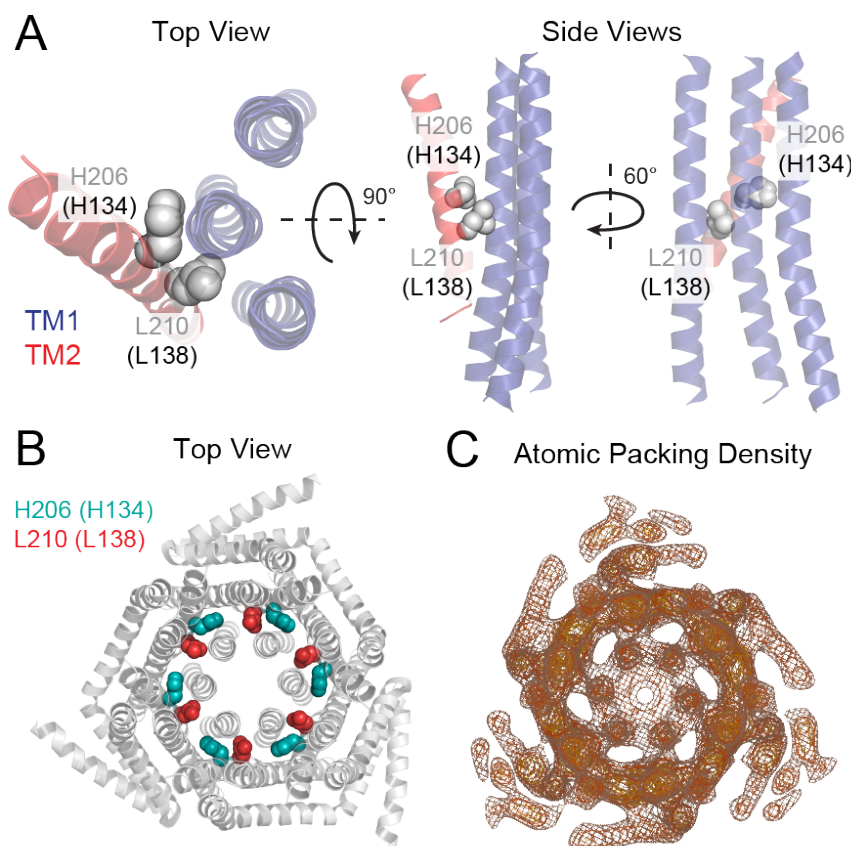


**Figure 4.5 Schematic of H134-L138 brace of TM1.** (A) Top and side views of residues H134 and L138 (grey spheres) at the TM1 (blue) and TM2 (red) interface. The two amino acids are on either side of the pore helix, approximately one turn apart. One TM2 and three TM1 helices are displayed for simplicity. (B) Top view of the dOrai hexameric channel with the relative positions at the TM1-TM2/3 ring interface with H134 (teal) and L138 (red) shown. (C) Contact dots density mapped onto 4HKR, showing dense packing at TMs 2-4 and areas of lower packing behind the TM1 helices above H134. These regions allow for more conformational movement and may also be filled by water crevices that facilitate gating (see Chapter 5).

tilts towards the H134 region. These two residues could act as a pivot point during tilting or twisting of the pore helix that is correlated with the open and closed states. Using contact dots analysis, which examines the relative packing densities at different regions of the channel (see Chapter 3, **Figure 3.12**), we can predict which areas are loosely packed to allow conformational movements to occur. The contact dots density mapped onto the structure of dOrai reveals an area above H134 at the TM1-TM2/3 ring interface that is relatively loosely packed (**Figure 4.5C**) and

thus could theoretically accommodate the predicted tilting of TM1 controlled by the L138 and H134 brace.

Unlike most other GOF mutants, Orai1 L138F displays a decline in current during hyperpolarizing steps in the absence of STIM1 (**Figure 4.4B, C**). Consistent with the idea that L138 is closely coupled with T92 on TM1, GOF mutations at T92 are able to phenocopy this aspect of L138F/Y channels (**Figure 4.4G-I**). Although several molecules, including calmodulin (89) and STIM1 (65, 86, 87), have been proposed to contribute to CDI, the mechanistic basis of fast CDI in Orai1 channels is currently not well understood. Within Orai1, the cytosolic domains are likely the key regulators based on studies using Orai1 and Orai3 chimeras and mutational analysis of the N-terminal inner pore, TM2-3 loop, and C-terminus (88, 90-92). The most recent studies suggest that the inactivation domain of STIM1 is coupled to the inner pore to regulate CDI (86, 88). Specifically, it was shown that mutations of aromatic residues Y80 and W76 at the most intracellular end of the N-terminal helix can enhance or abrogate CDI in Orai1 channels (88). To a lesser extent, the three positively charged residues (R91, K87, and R83), which have been implicated as an inner gate, also contribute to CDI (88).

We currently do not have a straightforward mechanistic explanation of why L138 and T92 mutants show CDI-like inactivation over hyperpolarizing steps. It is plausible that these channels are inactivated at baseline by  $\text{Ca}^{2+}$ , as seen through their large current amplitudes in DVF solutions compared with 20 mM  $\text{Ca}^{2+}$  solution (**Figure 4.1B**). Based on EGTA and 110 mM  $\text{Ca}^{2+}$  solution experiments, the inactivation seen in L138X and T92X is not sensitive to changes in  $\text{Ca}^{2+}$  near the pore and therefore may not be as tightly coupled to the  $\text{Ca}^{2+}$  sensor. To further understand the  $\text{Ca}^{2+}$  dependence of the inactivation, future experiments should include application of  $\text{Ba}^{2+}$ -based solutions. While Orai1 channels can conduct  $\text{Ba}^{2+}$  (a larger divalent compared to  $\text{Ca}^{2+}$ ) through

the pore, there is less CDI observed in  $\text{Ba}^{2+}$ -containing solutions, presumably due to decreased affinity for the  $\text{Ca}^{2+}$  sensing site. Given the current data, however, it appears that these mutations put the inner pore residues in a conformation that mimics the inactivated state. Further investigation of this intriguing phenomenon is necessary to tease apart the mechanism of inactivation in these mutants. Together, the results from this study suggest that L138-T92 interaction at the TM2-TM1 interface contributes to pore conformational changes that mediate both channel activation and inactivation.

## CHAPTER 5: A TM1-TM3 HYDROPHOBIC INTERACTION ACTS AS GATE LATCH TO FACILITATE ORAI1 CHANNEL ACTIVATION

*(Manuscript in preparation)*

### **Introduction**

Orai1 channels open in response to binding of STIM1 to the cytosolic surface of the protein, which is postulated to trigger a set of conformational changes in the protein that culminates in pore helix rotation and pore dilation. Based on the atomic packing analysis of the TM domains shown in the previous chapter, it is thought that the intra- and inter-subunit surfaces between neighboring TM2 and TM3 helices as well as the interface between TM4 and the TM2/3 ring are relatively rigid. Therefore, for the gating conformational changes in the pore to occur, the TM1-TM2/3 ring interface must provide a favorable environment that allows for a considerable amount of conformational flexibility of the pore helix. Here, we examined the interface between the TM2/3 ring and TM1 and discovered the presence of water crevices that may lower the energetic cost of pore helix rotation and facilitate Orai1 channel activation.

### **Results**

#### **Molecular dynamics simulations and cysteine accessibility analysis reveal water crevices behind the pore helices**

One unexpected finding from our previous MD simulations of the WT dOrai channel is the presence of water in crevices located behind the pore helices (**Figure 5.1**). Although the majority of water molecules in the channel were located in the pore, there was a substantial number of water molecules observed in narrow crevices between the TM2/3 ring and TM1. In some subunits, that channel of water continues from the extracellular side through the cytoplasmic surface, while

others had water enter from the outer and inner surfaces but remained dry in the region surrounding the hydrophobic cluster. This finding is currently awaiting further characterization and quantification by our MD collaborators.

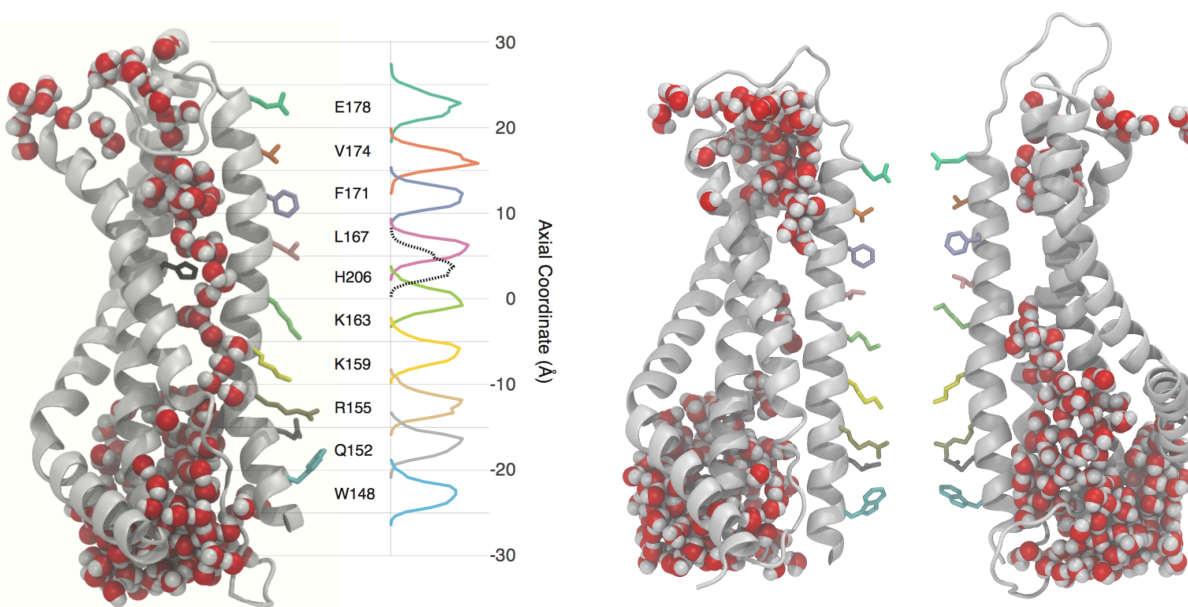


**Figure 5.1 Water crevices behind the pore helices revealed by MD simulations.** MD simulations of WT dOrai show water molecules (red and grey spheres) filling a narrow channel at the TM1-TM2/3 ring interface. Left: A snapshot of one monomer shown with pore residues and H206 on TM2 labeled for reference. Right: A snapshot of water crevices in two monomers across from each other. For simplicity, pore waters are not shown. (MD simulations were performed by Christopher Ing.)

In order to experimentally verify the presence of water crevices behind the pore observed in the MD simulations, we introduced cysteine residues along the TM1-TM2/3 ring interface and tested if  $\text{Ag}^+$  is able to modify these residues.  $\text{Ag}^+$  is a small monovalent cation that binds tightly to solvent-exposed thiol groups, forming S-Ag bonds. Because the charged ion is expected to be surrounded by water molecules in solution, modification of introduced cysteines by  $\text{Ag}^+$  can be used to as a readout for water accessible surfaces on ion channels. Although the effects of  $\text{Ag}^+$  binding on channel activity may be difficult to predict, a change in current amplitude or ion selectivity strongly implies that the residue in question is solvent accessible.

We found that channels with TM1 cysteine mutants had three different types of behaviors when exposed to  $\text{Ag}^+$ : inhibition, potentiation, or neither inhibition nor potentiation (**Figure 5.2**). Orail channels with cysteines introduced at residues that are known to be pore-facing in the STIM1-activated state were blocked by  $\text{Ag}^+$  (**Figure 5.2B, E, F**) presumably because  $\text{Ag}^+$  binding

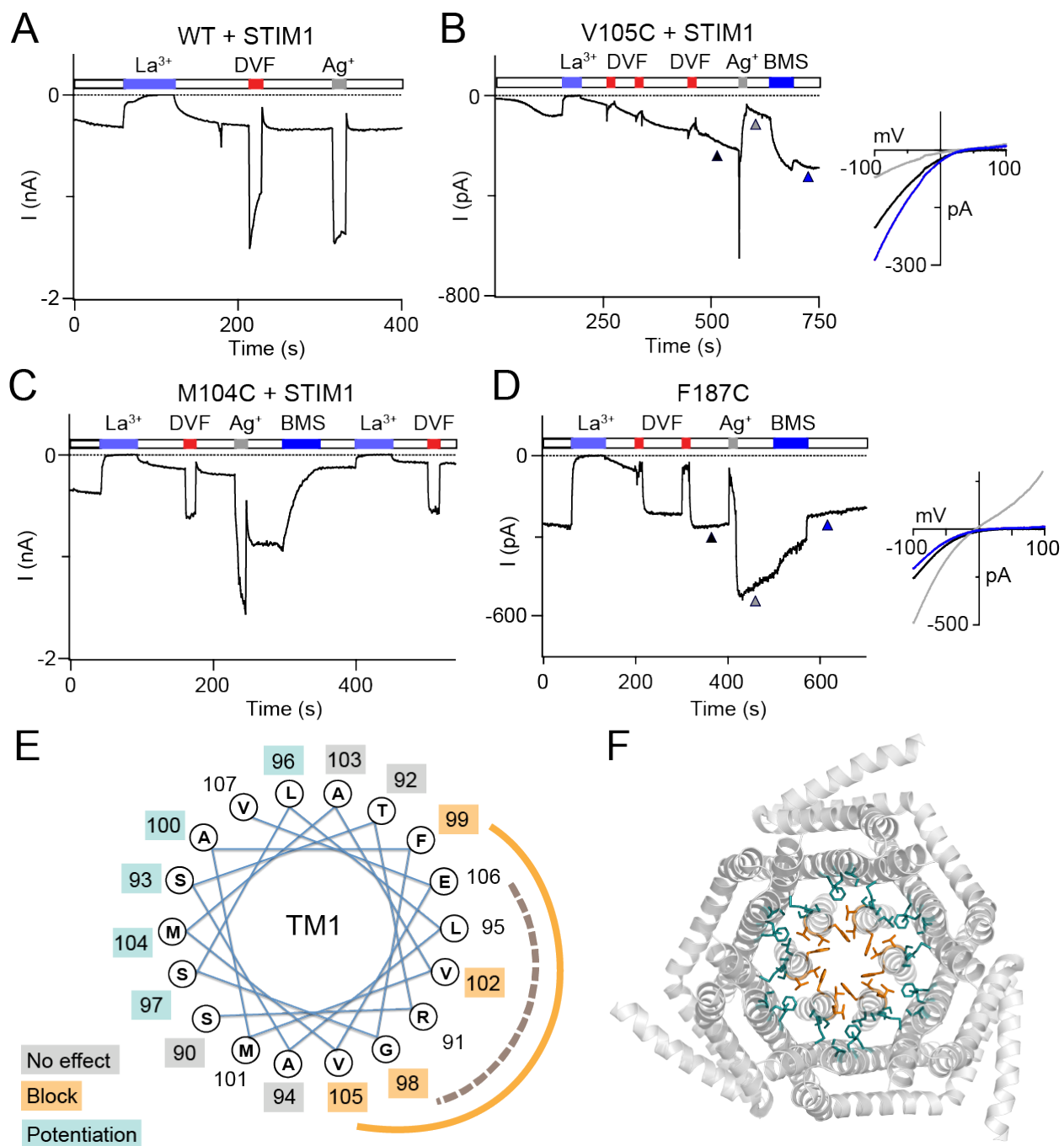


**Figure 5.2 Modification of non-pore lining residues by Ag<sup>+</sup> confirms water crevices behind the Orai1 pore helix.** (A) Application of Ag<sup>+</sup> (60 nM) in NO<sub>3</sub>-based DVF solution does not have any effect on STIM1-activated WT Orai1 channels. (B) Ag<sup>+</sup> (60 nM) blocks V105C Orai1 currents channels. I-V relationships at time points indicated by colored arrows are shown. (C-D) Ag<sup>+</sup> (60 nM) potentiates the currents of STIM1-activated M104C Orai1 and the constitutively active TM3 mutant F187C. The current potentiation is reversible by BMS (5 mM). I-V relationships at time points indicated by colored arrows are shown. (E) Helical wheel of TM1 as viewed from above. Cysteine mutations at positions that show no effect, block, or potentiation are shaded in grey, orange, and teal respectively. Orange line outlines pore-lining residues in STIM1-activated channels as identified by sensitivity to Ag<sup>+</sup> block. Dashed brown line outlines residues that can be modified by Cd<sup>2+</sup> in the open state. (F) Top view of dOrai structure with positions of cysteine mutants whose currents are blocked by Ag<sup>+</sup> shown in orange sticks and those that are potentiated by Ag<sup>+</sup> shown as teal sticks.

to these cysteines blocks ion conduction in the pore. Interestingly, in line with the presence of water crevices behind the TM1 helices, Ag<sup>+</sup> was able to modify residues on the non-pore lining face of TM1, including M104, M101, A100, S97, L96, and S93 (**Figure 5.2C-F**). At these positions, modification by Ag<sup>+</sup> was detected as potentiation of the current that could be reversed by reducing agent BMS that cleaves the S-Ag bond. On the other hand, Ag<sup>+</sup> also potentiated currents of Orai1 channels with cysteines introduced at the complementary TM2/3 ring surface, including F187, V191, and L194 (**Figure 5.2F**).

### **Mutational analysis suggests a distinct functional role of M101 in the TM1-TM3**

#### **hydrophobic cluster**

Our recent study of the TM1-TM3 hydrophobic stack (L96, M101, M104, F187, V191, and L194) suggested that M101 is crucial for relaying the gating signal to the pore based on the loss-of-function phenotype of M101A channels (**Figure 3.14**). Interestingly, another previous study using TM1 cysteine mutants noted that M101C is one of only two loss-of-function TM1 cysteine mutants (the other being the selectivity filter mutant E106C) (38). Given its sensitivity to the relatively mild perturbation of mutating Met to Cys and its location situated directly behind the hydrophobic gate formed by F99 and V102 (2, 36) (**Figure 5.3A**), we hypothesized that M101 may be an

especially crucial component of the TM1-TM3 hydrophobic cluster in regulating channel function. To further examine the contribution of M101 to gating, we performed detailed mutagenesis of this residue (**Figure 5.3B**). Consistent with its role in maintaining the hydrophobic cluster as a functional bridge from the TM2/3 ring to TM1, mutations of M101 to smaller or polar residues yielded LOF channels (**Figure 5.3B**). However, surprisingly, we found that mutation of M101 to similarly sized hydrophobic amino acids such as Leu or Ile also produced channels that could not be activated by STIM1 (**Figure 5.3B**). This unexpected finding suggested that hydrophobicity

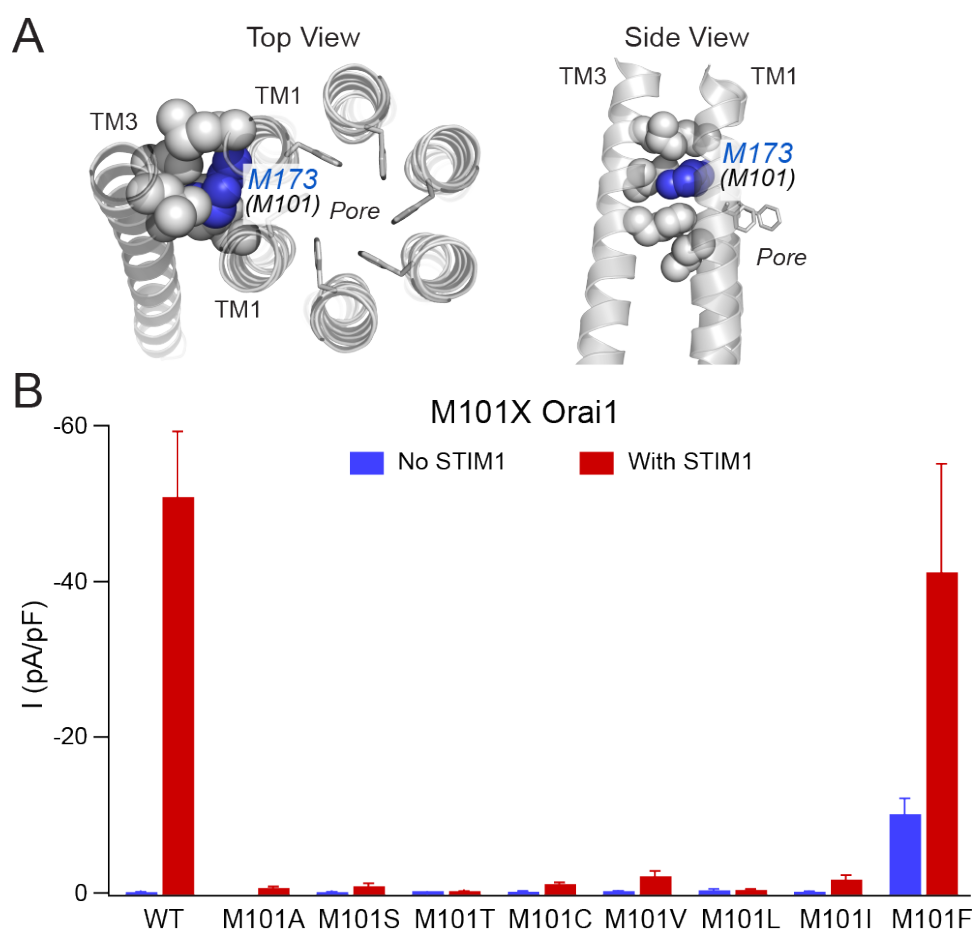


**Figure 5.3 Mutational analysis of M101 reveals predominantly loss-of-function channels. (A)** Top and side views of M173 (hOrai1 M101, blue) as part of the hydrophobic stack at the TM1-TM2/3 ring interface. **(B)** M101X mutants with and without STIM1 co-expression. Most of the mutants, including small and polar substitutions and even mutation to large hydrophobic residues like I/L, result in LOF channels. M101F is constitutively active and can be further gated by STIM1. Values are mean  $\pm$  S.E.M.

alone was not enough to retain channel function and implied that the Met residue at position 101 may also be important for a different function in addition to its role in the hydrophobic cluster.

### Molecular dynamics simulations show that M101 interacts with F99 in activated states

To explore this possibility, we turned to molecular dynamics simulations of the WT vs. GOF H206C/S channels. MD simulations revealed that although the residues in the rest of the hydrophobic stack displayed very small fluctuations consistent with their role as a rigid relay from TM3 to TM1, the M101 side chain was very flexible and regularly sampled rotamers that deviated from the crystal structure. In the WT simulation, M101 appeared to be mostly in contact with F187 as part of the hydrophobic stack behind TM1 (**Figure 5.4A**). Strikingly, in the H206S/C

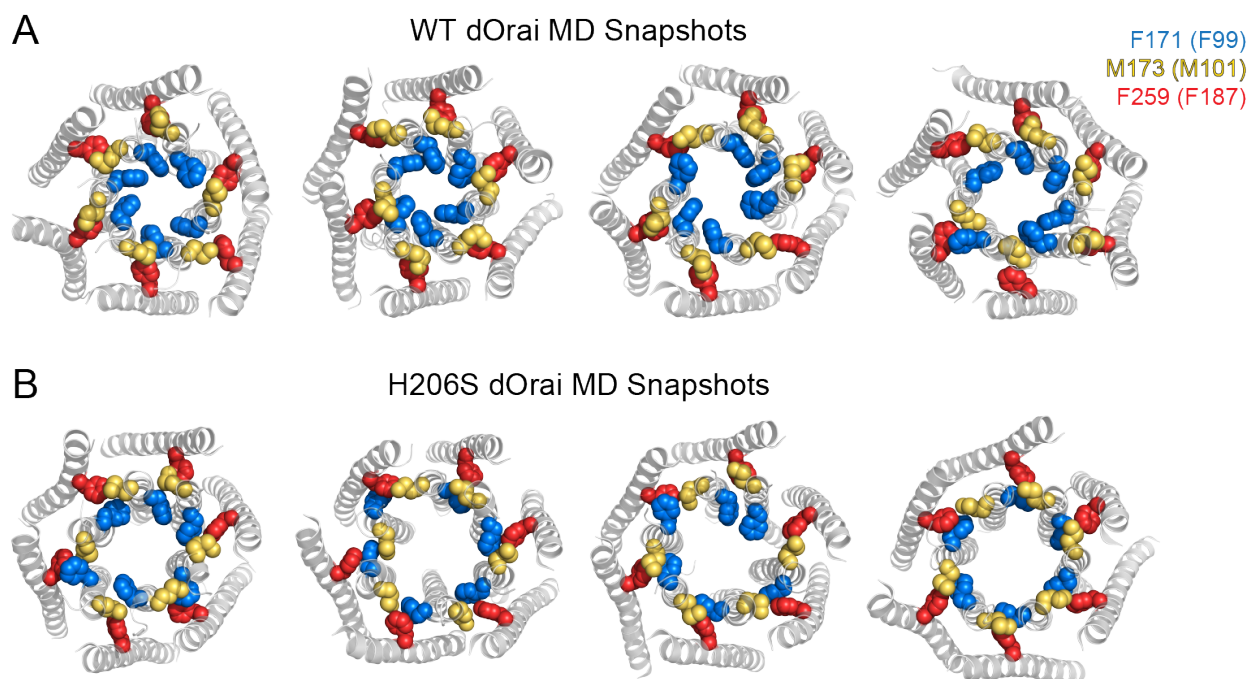


**Figure 5.4 Snapshots of the F99-M101-F187 locus in MD simulations of WT and H206S dOrai.** **(A)** Snapshots of four selected independent MD simulations of WT dOrai taken at 350 ns (equilibrium reached at approximately 100 ns). **(B)** Snapshots of four selected independent MD simulations of GOF mutant H206S (hOrai1 H134S) dOrai taken at 350 ns. Side chains of F171 (hOrai1 F99, blue), M173 (hOrai1 M101, yellow), and F259 (hOrai1 F187, red) are represented as spheres. In the WT simulations, M173 appears to predominantly interact with F259, while in the H206S dOrai snapshots, it interacts with F171 as well. (MD simulations were performed by Christopher Ing.)

channels, pore helix rotation and slight pore dilation often caused M101 side chains to reorient away from F187 and come into contact with the F99 residues of neighboring subunits (**Figure 5.4B**). Visual inspection of the movies suggested that the M101-F99 interaction is correlated with rotation of F99 away from the pore axis (awaiting further analysis and quantification from our MD collaborators). This observation raises the intriguing possibility that M101 may help stabilize F99 side chains in the rotated orientation in the open channel state (2).

### A $\text{Cd}^{2+}$ bridge between M101 and F99 enhances Orai1 channel activity

Because F99-M101 interactions are augmented in the active H206S/C channel compared with the closed WT state, we next tested whether forcing an interaction between F99 and M101 could activate the channel. Although F99C channels have inherently “leaky” gates due to disruption of the hydrophobic barrier in the pore, we examined if F99C/M101C channels could be further activated by the addition of thiol-reactive divalent ion  $\text{Cd}^{2+}$ , which would be expected to mediate a bridge between F99 and M101. Consistent with our hypothesis that F99-M101 interaction

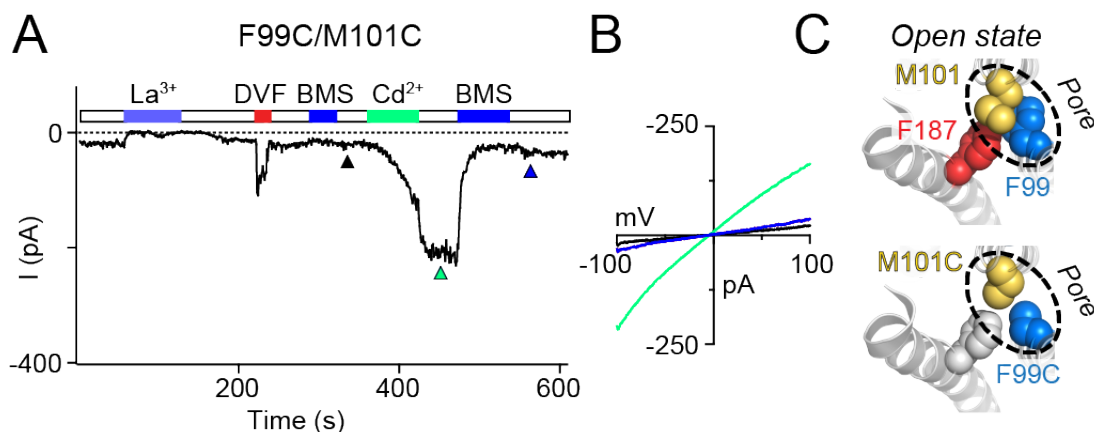


**Figure 5.5 A  $\text{Cd}^{2+}$  bridge between F99C and M101C potentiates Orai1 current.** (A) F99C/M101C Orai1 has some baseline activity without STIM1 that is significantly boosted by  $\text{Cd}^{2+}$  (5  $\mu\text{M}$ ). The enhancement of current by  $\text{Cd}^{2+}$  can be reversed by BMS (5 mM). (B) I-V relationships of F99C/M101C at the time points indicated by the colored arrowheads. (C) Top: Cartoon of the interaction between F99 and M101 in one subunit of the open state from a snapshot of a MD simulation of the constitutively open mutant H206S dOrai. Bottom: Cartoon of the interaction between F99C and M101C that mediates potentiation of the Orai1 current by  $\text{Cd}^{2+}$ .

stabilizes the open state, application of  $\text{Cd}^{2+}$  in F99C/M101C channels increased Orai1 current amplitude approximately ten-fold (**Figure 5.5A**). The  $\text{Cd}^{2+}$ -mediated potentiation was stable and could only be reversed by reducing agent BMS. F99C and M101C single cysteine mutants do not exhibit  $\text{Cd}^{2+}$ -dependent current enhancement, indicating that cysteines at both positions are required for the potentiation effect. On the other hand, STIM1-gated F99C/M101C channels are also not further activated by  $\text{Cd}^{2+}$ , presumably because they are already nearly fully active at baseline (not shown). Overall, the potentiation of F99C/M101C Orai1 current by  $\text{Cd}^{2+}$  suggests that M101 may play a role in rotating F99 away from the pore axis.

#### **A $\text{Cd}^{2+}$ bridge between M101 and F187 abrogates Orai1 currents**

If stabilizing a F99-M101 interaction can augment channel current, does the enhancement of the interaction between M101 and F187 favor the closed state? In order to test this idea, we applied  $\text{Cd}^{2+}$  to M101C/F187C double cysteine mutant. Although M101C cannot be gated by STIM1, the F187C GOF mutation conferred constitutive channel activity to it in the double mutant. Strikingly, when  $\text{Cd}^{2+}$  was applied, M101C/F187C Orai1 current was almost completely inhibited (**Figure 5.6A**). This inhibition was reversed by BMS, consistent with a cysteine-mediated effect. We surmised that  $\text{Cd}^{2+}$  was able to access the M101C/F187C interface, since  $\text{Ag}^+$  was also able to modify position F187 (**Figure 5.2D-F**) and that a bridge between M101C and F187C evokes pore closure.

However, it is also possible that either M101C or F187C becomes pore facing and that inhibition of the current was in fact due to pore block by  $\text{Cd}^{2+}$  coordinated by cysteines across the pore.  $\text{Cd}^{2+}$  application to M101C/H134S, which retains the M101C residue in the background of a different constitutively active mutant, did not show significant block, demonstrating that M101C likely does not become pore facing (**Figure 5.6D**). In addition, in the M101A/F187C double

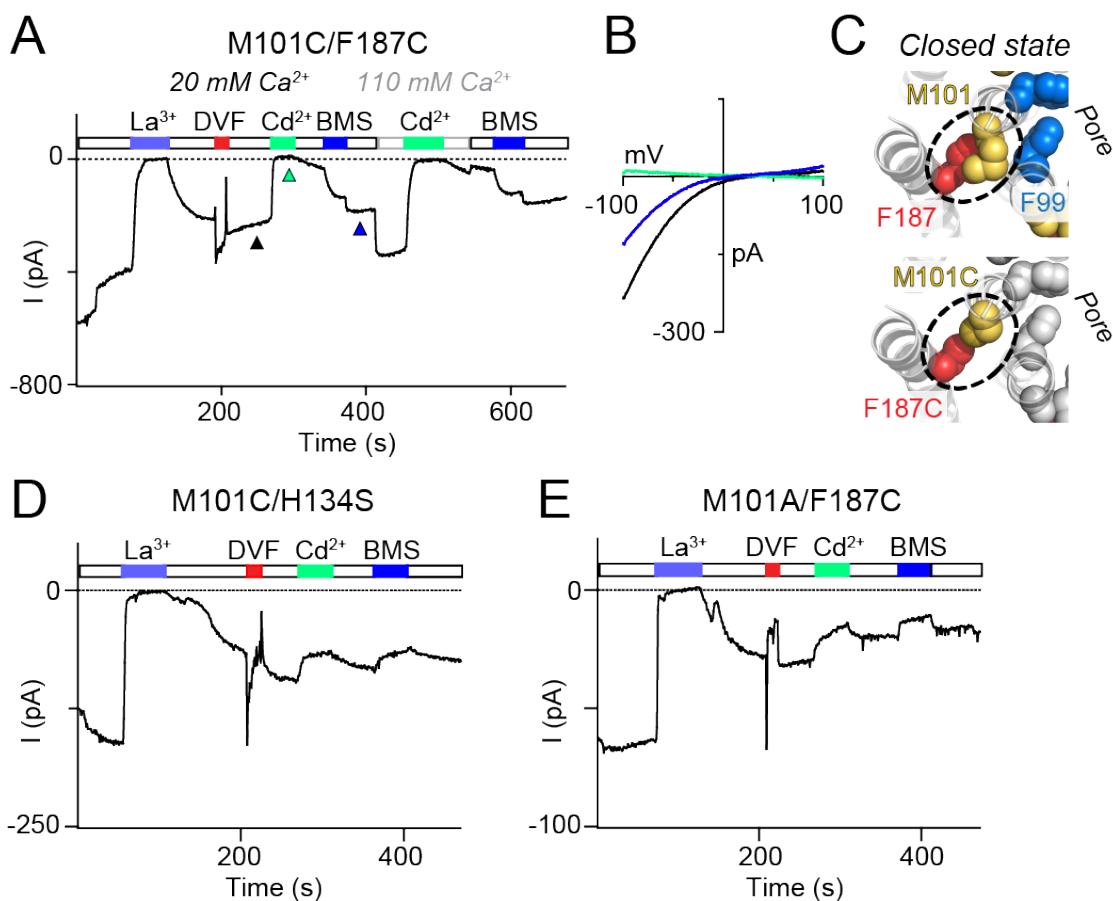


**Figure 5.6 A Cd<sup>2+</sup> bridge between M101C and F187C abrogates Orai1 current.** (A) Cd<sup>2+</sup> (5 μM) strongly inhibits the current of M101C/F187C channels, which can be reversed by BMS (5 mM). Application of Cd<sup>2+</sup> (5 μM) in 110 mM Ca<sup>2+</sup> solution also abrogates M101C/F187C currents. (B) I-V relationships of M101C/F187C at the time points indicated by the colored arrowheads. (C) Top: Cartoon of the interaction between M101 and F187C in one subunit of the closed state from a snapshot of a WT dOrai MD simulation. Bottom: Cartoon of the interaction between M101C and F187C that likely mediates inhibition of the Orai1 current by Cd<sup>2+</sup>. (D-E) Double mutants with only one cysteine at positions M101C or F187C do not exhibit current block by Cd<sup>2+</sup>, suggesting that the current inhibition seen in M101C/F187C is mediated by both residues.

mutant that retains F187C but with Ala instead of Cys at M101 also shows no significant effect with Cd<sup>2+</sup> application (**Figure 5.6E**). In another test to see if the Cd<sup>2+</sup> block in M101C/F187C channels occurs in the pore rather than at the TM1-TM2/3 ring interface, we applied Cd<sup>2+</sup> in 110 mM extracellular solution. If Cd<sup>2+</sup> was indeed coordinated in the pore, increased Ca<sup>2+</sup> flux through the channel is expected to compete with the Cd<sup>2+</sup> binding and reduce the amount of pore block. However, application of Cd<sup>2+</sup> in 110 mM Ca<sup>2+</sup> solution did not significantly alter the extent of

current inhibition (**Figure 5.6A**). Overall, these experiments show that both M101C and F187C are needed for the strong  $\text{Cd}^{2+}$  block effect in M101C/F187C channels and that enhancing the interaction between these residues facilitates closure of the channel pore.

## **Discussion**

The hydrophobic gate of Orai1 channels is activated, in part, through the rotation of the pore helix to move the bulky F99 side chains away from the pore axis (2). In this study, we examined two features of Orai1 that facilitate this process and help lower the energetic cost of pore helix rotation in the context for the entire channel. First, through MD simulations and  $\text{Ag}^+$  accessibility screening, we discovered the unexpected presence of water crevices behind the pore helices (**Figure 5.1**). MD simulations show that this narrow cleft of water is widest at the outer and inner portions of the channel, with the middle of TM1-TM2/3 ring interface near the hydrophobic clamp appearing to only accommodate one to two water molecules (awaiting quantification). Since  $\text{Ag}^+$  is only soluble in water and therefore can only access areas where water is present, modification of cysteine mutants at the TM1-TM2/3 ring interface by  $\text{Ag}^+$  (**Figure 5.2**) also lends strong support for the presence of water crevices. One straightforward interpretation of this finding is that water behind the pore helices is important for gating, perhaps by serving as a lubricant that facilitates the switching of hydrophobic/hydrophilic interaction partners at the TM1-TM2/3 ring interface. Moreover, the water may reside in the pockets of loose packing behind TM1 observed using contact dots analysis (**Figure 4.5C**) and may change locations as the TM1 rotates and tilts.

While appealing, direct tests of these ideas are challenging, because there is currently no direct way to visualize the water molecules during an experiment. Instead, we are constrained to inferring the location of water crevices based on results from cysteine accessibility and mutational

analysis studies. These methods have their limitations because attempts at modulating the amount or location of water behind the pore through mutagenesis is coupled with other confounding effects that cannot be easily teased apart given that the readout by patch clamping is channel current through the pore, which is an indirect measure for the water crevices. Thus, the functional significance of the water crevices await exploration in further studies.

Another feature of Orai1 that likely contributes to closed-open transitions in the pore is the M101 gate latch. MD simulations suggested that, in contrary to our previous predictions of its role in a conformationally constrained hydrophobic clamp, M101 retains a considerable amount of flexibility. Most notably, it appears to interact with F187 on TM3 in the closed state and with F99 in the open state. We confirmed this experimentally by introducing double cysteine mutants that can be bridged by  $\text{Cd}^{2+}$ . In F99C/M101C channels where  $\text{Cd}^{2+}$  enhances interaction between F99 and M101, Orai1 channel current was potentiated. The opposite is true for M101C/F187C channels, where  $\text{Cd}^{2+}$  abrogates channel current by stabilizing interaction between M101 and F187. Moreover, despite presumably retaining the hydrophobic clamp, M101L/I Orai1 channels cannot be activated by STIM1; hence, it is clear that this Met residue is essential to channel gating. This discrepancy can be explained by the fact that the sulfur group enables methionine-aromatic interactions which are stronger than purely hydrophobic interactions (93, 94), and Met is longer and more flexible than Leu or Iso, allowing it to interact with both F187 on TM3 and F99 in the pore. Therefore, M101 is perfectly positioned, with the suitable length and added sulfur group, to interact with F187 and F99 act as an effective gate latch to facilitate opening and closing of the F99 channel gate.

## MATERIALS AND METHODS

**Cells.** HEK293 cells were maintained in suspension at 37°C with 5% CO<sub>2</sub> in CD293 medium supplemented with 4 mM GlutaMAX (Invitrogen). For imaging and electrophysiology, cells were plated onto poly-L-lysine coated coverslips one day before transfection and grown in a medium containing 44% DMEM (Corning), 44% Ham's F12 (Corning), 10% fetal bovine serum (HyClone), 2 mM glutamine, 50 U/ml penicillin and 50 µg/ml streptomycin.

**Plasmids and transfections.** The Orai1 mutants employed for electrophysiology were engineered into either the previously described C-terminal myc-tagged Orai1 construct (MO70 Orai1) in the bicistronic expression vector pMSCV-CITE-eGFP-PGK-Puro (22) or a pEYFP-N1 vector (Clontech) to produce C-terminally tagged Orai1-YFP proteins (54). No differences in current density were observed between the two constructs. mCherry-STIM1 and CFP-CAD were kind gifts of Dr. R. Lewis (Stanford University, USA). All mutants were generated by the QuikChange Mutagenesis Kit (Agilent Technologies) and the mutations were confirmed by DNA sequencing. For electrophysiology, the indicated Orai1 constructs were transfected into HEK293 cells either alone (200 ng DNA per coverslip) or together with STIM1 (100 ng Orai1 and 500 ng STIM1 DNA per coverslip). For FRET and confocal microscopy experiments, cells were transfected with Orai1-YFP alone (200 ng DNA per coverslip) or with CFP-CAD constructs (100 ng each per coverslip). All transfections were performed using Lipofectamine 2000 (Thermo Fisher Scientific) 24-48 hours prior to electrophysiology or imaging experiments.

**Solutions and Chemicals.** The standard extracellular Ringer's solution used for electrophysiological experiments contained 130 mM NaCl, 4.5 mM KCl, 20 mM CaCl<sub>2</sub>, 10 mM tetraethylammonium chloride (TEA-Cl), 10 mM D-glucose, and 5 mM HEPES (pH 7.4 with NaOH). For the FRET and confocal imaging studies, the Ringer's solution contained 2 mM CaCl<sub>2</sub> and 150 mM NaCl with the other components as above. The DVF Ringer's solution contained 150 mM NaCl, 10 mM HEDTA, 1 mM EDTA, 10 mM TEA-Cl and 5 mM HEPES (pH 7.4). The internal solution contained: 135 mM Cs aspartate, 8 mM MgCl<sub>2</sub>, 8 mM Cs-BAPTA, and 10 mM HEPES (pH 7.2 with CsOH). For the Ag<sup>+</sup> block experiments, the external (divalent free) solution contained: 120 mM NaNO<sub>3</sub>, 10 mM EDTA and 10 mM HEPES (pH 7.4). 60 nM Ag<sup>+</sup> was added to this NaNO<sub>3</sub>-based divalent free solution at the appropriate amount calculated from the Max-Chelator software (WEBMAXC 2.10). A concentrated stock (100 mM) of AgNO<sub>3</sub> in water protected from the light was prepared freshly for each experiment and diluted as needed to obtain the working concentration.

**Electrophysiology.** Currents were recorded in the standard whole-cell configuration at room temperature on an Axopatch 200B amplifier (Molecular Devices) interfaced to an ITC-18 input/output board (Instrutech). Routines developed by R. S. Lewis (Stanford) on the Igor Pro software (Wavemetrics) were employed for stimulation, data acquisition and analysis. Data are corrected for the liquid junction potential of the pipette solution relative to Ringer's in the bath (10 mV). The holding potential was +30 mV. The standard voltage stimulus consisted of a 100-ms step to -100 mV followed by a 100-ms ramp from -100 to +100 mV applied at 1 s intervals. I<sub>CRAC</sub> was typically activated by passive depletion of ER Ca<sup>2+</sup> stores by intracellular dialysis of 8 mM

BAPTA. All currents were acquired at 5 kHz and low pass filtered with a 1 kHz Bessel filter built into the amplifier. All data were corrected for leak currents collected in 100-200  $\mu\text{M}$   $\text{LaCl}_3$ .

**Data analysis.** Analysis of current amplitudes was typically performed by measuring the peak currents during the -100 mV pulse. Specific mutants were categorized as gain-of-function if their currents exceeded 2 pA/pF, which is more than ten times the current density of WT Orai1 without STIM1. Reversal potentials were measured from the average of several leak-subtracted sweeps in each cell. Fractional blockade of current was quantified as:  $\text{blockade}=(1-I_b/I_{\text{Ctrl}})$ , where  $I_b$  is the Orai1 current in the presence of  $\text{Cd}^{2+}$ , and  $I_{\text{Ctrl}}$  is the Orai1 current prior to application of the blocker. The fold increase in current following whole-cell break-in was calculated by measuring the peak of the STIM1-gated current amplitude at 300 s or later divided by the amount of constitutive current seen at the time of whole-cell break-in ( $t=0$ ). In cells where 100-200  $\mu\text{M}$   $\text{LaCl}_3$  did not completely block the current, the raw non-leak subtracted current amplitude was used as the baseline current at whole-cell break-in to compare with the current amplitude after store-depletion, with the assumption that most of the standing current arose from the over-expressed open mutant rather than from other sources.

**FRET microscopy.** HEK293 cells transfected with Orai1-YFP and CFP-CAD DNA constructs were imaged using wide-field epifluorescence microscopy on an IX71 inverted microscope (Olympus, Center Valley, PA). Cells were imaged with a 60X oil immersion objective (UPlanApo NA 1.40), a 175 W Xenon arc lamp (Sutter, Novato, CA), and excitation and emission filter wheels (Sutter, Novato, CA). At each time point, three sets of images (CFP, YFP, and FRET) were captured on a cooled EM-CCD camera (Hamamatsu, Bridgewater, NJ) using optical filters specific

for the three images as previously described. Image acquisition and analysis was performed with SlideBook software (Imaging Innovations Inc., Denver, CO). Images were captured at exposures of 100-500 ms with 1\*1 binning. Lamp output was attenuated to 25% by a 0.6 ND filter in the light path to minimize photobleaching. All experiments were performed at room temperature.

FRET analysis was performed as previously described (2, 54). The microscope-specific bleed-through constants ( $a=0.12$ ;  $b=0.008$ ;  $c=0.002$  and  $d=0.33$ ) were determined from cells expressing cytosolic CFP or YFP alone. The apparent FRET efficiency was calculated from background-subtracted images using the formalism (95):

$$E_{FRET} = \frac{F_c}{F_c + G I_{DD}}$$

where  $F_c = I_{DA} - aI_{AA} - dI_{DD}$

$I_{DD}$ ,  $I_{AA}$  and  $I_{DA}$  refer to the background subtracted CFP, YFP, and FRET images, respectively.

The instrument dependent G factor had the value  $1.85 \pm 0.1$ . E-FRET analysis was restricted to cells with YFP/CFP ratios in the range of 2-6 to ensure that E-FRET was compared across identical acceptor to donor ratios, and measurements were restricted to regions of interest drawn at the plasma membrane.

**Confocal microscopy.** HEK293 cells expressing various Orai1-YFP mutants and CFP-CAD were imaged on an Andor XDI Revolution spinning-disk confocal microscope equipped with a 100X oil immersion objective. Cells were maintained at 37°C with 5% CO<sub>2</sub>. Fluorophores were excited with 445 nm (CFP) and 515 nm (YFP) laser diodes with the intensity of laser light attenuated to 15-40% for CFP and 5-30% for YFP. Images were obtained at 512\*512 pixels at an exposure of 200-500 ms per frame and a slice thickness of 0.8 μm. An average of four frames were used for each image. Images analysis was performed using NIH ImageJ software (NIH, Bethesda, MD).

**Molecular dynamics simulations.** Molecular models were constructed using the crystal structure of the *Drosophila melanogaster* Orai channel (PDB: 4HKR) (7). Missing residues of the M1-M2 loop (amino acids 181 to 190) and the M2-M3 loop (amino acids 220 to 235) were modelled *de novo* using MODELLER (96). System preparation was performed using CHARMM-GUI membrane builder (97). The protein was embedded within a hydrated 1-palmitoyl,2-oleoyl-sn-glycero-3-phosphocholine (POPC) bilayer with 150 mM NaCl, consisting of ~112K atoms. Single point mutations were made using CHARMM-GUI to create the H206C, H206S, H206C, H206Y, H206Q, and V174A systems. The CHARMM36 force field was used for protein (98, 99), ions, and lipids (100) along with the TIP3P water model (101). Simulations were performed using GROMACS 2016.3 (102) using default CHARMM-GUI output parameters. Thirty simulation repeats were then created for each of the six systems, with the exception of H206C (ten repeats). Production simulations were initialized with randomized velocities and conducted for ~400 ns for each repeat of the WT system and each repeat of the mutant systems, for an aggregate total of 67.46  $\mu$ s. Three additional systems containing ten repeats of length ~400 ns were independently simulated to examine the effect of temperature and Na<sup>+</sup> binding on hydration and conformational fluctuations of F171, which resulted in an additional 12.77  $\mu$ s of data. Analysis was performed on all simulation frames spaced at 1.0 ns after removing the first 100 ns of data from each simulation repeat.

**Atomic packing analysis.** Atomic packing analysis including explicit hydrogen atoms was carried out using the programs REDUCE and PROBE (71, 72). The PROBE algorithm simulates rolling a 0.25Å radius sphere along the van der Waals surfaces; where the probe sphere contacts two surfaces, each is marked with an indication (a 'dot') that classifies whether the surfaces are in wide

contact ( $>0.25\text{\AA}$  apart), close contact ( $0.25\text{-}0.0\text{\AA}$ ), overlapped (interpenetrating to  $-0.25\text{\AA}$ ), and clashing ( $>-0.25\text{\AA}$ ). Bad contacts, or clashes, arise from inaccuracies in the model and are found increase with decreasing crystallographic resolution (71, 72). Although the structure of 4HKR was determined at  $3.3\text{\AA}$  resolution, the distribution of small-probe contact dots nevertheless provides a qualitative measure of the extent and complementarity of local packing interactions. Helix-helix specific contacts were investigated using selection flags available in PROBE (71, 72). The resulting contact dot scores were summed for all atoms of a residue and assigned on a residue-by-residue basis using a script based on ScoreDotsAtAtom (71, 72), then tabulated and displayed using PyMOL. Contact dots density cage of 4HKR (Figure 4.5) was displayed using KiNG (Kineimage, Next Generation) developed by Duke University.

**Generation of averaged structures from MD simulations.** Each monomer of WT and H206C dOrai from ten representative frames from the MD simulations (six monomers per channel \* ten frames per mutant = sixty monomers total per mutant) was aligned to a monomer from the dOrai crystal structure in order to synchronize the orientation of the monomers. The positions of each atom were then averaged using ProDy (a Python-based structural dynamics analysis package) to generate an averaged model of the various mutants. The hexameric channel was reassembled by replacing each monomer of a snapshot of the mutant with the averaged monomeric structure.

**REFERENCES**

1. Radzicka A & Wolfenden R (1988) Comparing the polarities of the amino acids: side-chain distribution coefficients between the vapor phase, cyclohexane, 1-octanol, and neutral aqueous solution. *Biochemistry* 27(5):1664-1670.
2. Yamashita M, *et al.* (2017) STIM1 activates CRAC channels through rotation of the pore helix to open a hydrophobic gate. *Nature communications* 8:14512.
3. Yeung PS, Yamashita M, & Prakriya M (2017) Pore opening mechanism of CRAC channels. *Cell calcium* 63:14-19.
4. Tieleman DP, Shrivastava IH, Ulmschneider MR, & Sansom MS (2001) Proline-induced hinges in transmembrane helices: possible roles in ion channel gating. *Proteins* 44(2):63-72.
5. Clapham DE (2007) Calcium signaling. *Cell* 131(6):1047-1058.
6. Putney JW, Jr. (1986) A model for receptor-regulated calcium entry. *Cell calcium* 7(1):1-12.
7. Putney JW (2009) Capacitative calcium entry: from concept to molecules. *Immunological reviews* 231(1):10-22.
8. Prakriya M & Lewis RS (2015) Store-Operated Calcium Channels. *Physiological reviews* 95(4):1383-1436.
9. Hoth M & Penner R (1992) Depletion of intracellular calcium stores activates a calcium current in mast cells. *Nature* 355(6358):353-356.
10. Feske S (2010) CRAC channelopathies. *Pflugers Archiv : European journal of physiology* 460(2):417-435.

11. Feske S, *et al.* (2006) A mutation in Orai1 causes immune deficiency by abrogating CRAC channel function. *Nature* 441(7090):179-185.
12. Lacruz RS & Feske S (2015) Diseases caused by mutations in ORAI1 and STIM1. *Ann N Y Acad Sci* 1356:45-79.
13. Nesin V, *et al.* (2014) Activating mutations in STIM1 and ORAI1 cause overlapping syndromes of tubular myopathy and congenital miosis. *Proceedings of the National Academy of Sciences of the United States of America* 111(11):4197-4202.
14. Endo Y, *et al.* (2015) Dominant mutations in ORAI1 cause tubular aggregate myopathy with hypocalcemia via constitutive activation of store-operated Ca(2)(+) channels. *Human molecular genetics* 24(3):637-648.
15. Garibaldi M, *et al.* (2016) A novel gain-of-function mutation in ORAI1 causes late-onset tubular aggregate myopathy and congenital miosis. *Clin Genet.*
16. Bohm J, *et al.* (2017) ORAI1 Mutations with Distinct Channel Gating Defects in Tubular Aggregate Myopathy. *Hum Mutat* 38(4):426-438.
17. Roos J, *et al.* (2005) STIM1, an essential and conserved component of store-operated Ca<sup>2+</sup> channel function. *The Journal of cell biology* 169(3):435-445.
18. Zhang SL, *et al.* (2005) STIM1 is a Ca<sup>2+</sup> sensor that activates CRAC channels and migrates from the Ca<sup>2+</sup> store to the plasma membrane. *Nature* 437(7060):902-905.
19. Liou J, *et al.* (2005) STIM is a Ca<sup>2+</sup> sensor essential for Ca<sup>2+</sup>-store-depletion-triggered Ca<sup>2+</sup> influx. *Current biology : CB* 15(13):1235-1241.
20. Vig M, *et al.* (2006) CRACM1 multimers form the ion-selective pore of the CRAC channel. *Current biology : CB* 16(20):2073-2079.

21. Yeromin AV, *et al.* (2006) Molecular identification of the CRAC channel by altered ion selectivity in a mutant of Orai. *Nature* 443(7108):226-229.
22. Prakriya M, *et al.* (2006) Orai1 is an essential pore subunit of the CRAC channel. *Nature* 443(7108):230-233.
23. Zhou Y, *et al.* (2010) STIM1 gates the store-operated calcium channel ORAI1 in vitro. *Nature structural & molecular biology* 17(1):112-116.
24. Hoth M & Niemeyer BA (2013) The neglected CRAC proteins: Orai2, Orai3, and STIM2. *Current topics in membranes* 71:237-271.
25. Shim AH, Tirado-Lee L, & Prakriya M (2015) Structural and functional mechanisms of CRAC channel regulation. *Journal of molecular biology* 427(1):77-93.
26. Park CY, *et al.* (2009) STIM1 clusters and activates CRAC channels via direct binding of a cytosolic domain to Orai1. *Cell* 136(5):876-890.
27. Yuan JP, *et al.* (2009) SOAR and the polybasic STIM1 domains gate and regulate Orai channels. *Nature cell biology* 11(3):337-343.
28. Lewis RS (2007) The molecular choreography of a store-operated calcium channel. *Nature* 446(7133):284-287.
29. Hoth M & Penner R (1993) Calcium release-activated calcium current in rat mast cells. *The Journal of physiology* 465:359-386.
30. Hoth M (1995) Calcium and barium permeation through calcium release-activated calcium (CRAC) channels. *Pflugers Archiv : European journal of physiology* 430(3):315-322.
31. Yamashita M, Navarro-Borelly L, McNally BA, & Prakriya M (2007) Orai1 mutations alter ion permeation and Ca<sup>2+</sup>-dependent fast inactivation of CRAC channels: evidence for coupling of permeation and gating. *The Journal of general physiology* 130(5):525-540.

32. Prakriya M & Lewis RS (2006) Regulation of CRAC channel activity by recruitment of silent channels to a high open-probability gating mode. *The Journal of general physiology* 128(3):373-386.
33. Bakowski D & Parekh AB (2002) Monovalent cation permeability and Ca(2+) block of the store-operated Ca(2+) current I(CRAC) in rat basophilic leukemia cells. *Pflügers Archiv : European journal of physiology* 443(5-6):892-902.
34. Sather WA & McCleskey EW (2003) Permeation and selectivity in calcium channels. *Annu. Rev. Physiol* 65:133-159.
35. Yamashita M & Prakriya M (2014) Divergence of Ca<sup>2+</sup> selectivity and equilibrium Ca<sup>2+</sup> blockade in a Ca<sup>2+</sup> release-activated Ca<sup>2+</sup> channel. *J. Gen. Physiol.* 143(3):325-343.
36. McNally BA, Somasundaram A, Yamashita M, & Prakriya M (2012) Gated regulation of CRAC channel ion selectivity by STIM1. *Nature* 482(7384):241-245.
37. Zweifach A & Lewis RS (1993) Mitogen-regulated Ca<sup>2+</sup> current of T lymphocytes is activated by depletion of intracellular Ca<sup>2+</sup> stores. *Proceedings of the National Academy of Sciences of the United States of America* 90(13):6295-6299.
38. McNally BA, Yamashita M, Engh A, & Prakriya M (2009) Structural determinants of ion permeation in CRAC channels. *Proceedings of the National Academy of Sciences of the United States of America* 106(52):22516-22521.
39. Zhou Y, Ramachandran S, Oh-Hora M, Rao A, & Hogan PG (2010) Pore architecture of the ORAI1 store-operated calcium channel. *Proceedings of the National Academy of Sciences of the United States of America* 107(11):4896-4901.

40. Rulisek L & Vondrasek J (1998) Coordination geometries of selected transition metal ions (Co<sup>2+</sup>, Ni<sup>2+</sup>, Cu<sup>2+</sup>, Zn<sup>2+</sup>, Cd<sup>2+</sup>, and Hg<sup>2+</sup>) in metalloproteins. *J Inorg Biochem* 71(3-4):115-127.
41. Hou X, Pedi L, Diver MM, & Long SB (2012) Crystal structure of the calcium release-activated calcium channel Orai. *Science* 338(6112):1308-1313.
42. Yen M, Lokteva LA, & Lewis RS (2016) Functional Analysis of Orai1 Concatemers Supports a Hexameric Stoichiometry for the CRAC Channel. *Biophysical journal* 111(9):1897-1907.
43. Cai X, *et al.* (2016) The Orai1 Store-operated Calcium Channel Functions as a Hexamer. *The Journal of biological chemistry* 291(50):25764-25775.
44. Zhang SL, *et al.* (2011) Mutations in Orai1 transmembrane segment 1 cause STIM1-independent activation of Orai1 channels at glycine 98 and channel closure at arginine 91. *Proceedings of the National Academy of Sciences of the United States of America* 108(43):17838-17843.
45. Frischauf I, *et al.* (2017) Transmembrane helix connectivity in Orai1 controls two gates for calcium-dependent transcription. *Sci Signal* 10(507).
46. Gudlur A, *et al.* (2014) STIM1 triggers a gating rearrangement at the extracellular mouth of the ORAI1 channel. *Nature communications* 5:5164.
47. Dong H, Fiorin G, Carnevale V, Treptow W, & Klein ML (2013) Pore waters regulate ion permeation in a calcium release-activated calcium channel. *Proceedings of the National Academy of Sciences of the United States of America* 110(43):17332-17337.
48. Miyazawa A, Fujiyoshi Y, & Unwin N (2003) Structure and gating mechanism of the acetylcholine receptor pore. *Nature* 423(6943):949-955.

49. Neale C, Chakrabarti N, Pomorski P, Pai EF, & Pomes R (2015) Hydrophobic Gating of Ion Permeation in Magnesium Channel CorA. *PLoS Comput Biol* 11(7):e1004303.
50. Chang G, Spencer RH, Lee AT, Barclay MT, & Rees DC (1998) Structure of the MscL homolog from *Mycobacterium tuberculosis*: a gated mechanosensitive ion channel. *Science* 282(5397):2220-2226.
51. Li Z, *et al.* (2007) Mapping the interacting domains of STIM1 and Orai1 in Ca<sup>2+</sup> release-activated Ca<sup>2+</sup> channel activation. *The Journal of biological chemistry* 282(40):29448-29456.
52. McNally BA, Somasundaram A, Jairaman A, Yamashita M, & Prakriya M (2013) The C- and N-terminal STIM1 binding sites on Orai1 are required for both trapping and gating CRAC channels. *The Journal of physiology* 591(Pt 11):2833-2850.
53. Palty R & Isacoff EY (2016) Cooperative Binding of Stromal Interaction Molecule 1 (STIM1) to the N and C Termini of Calcium Release-activated Calcium Modulator 1 (Orai1). *The Journal of biological chemistry* 291(1):334-341.
54. Navarro-Borelly L, *et al.* (2008) STIM1-Orai1 interactions and Orai1 conformational changes revealed by live-cell FRET microscopy. *The Journal of physiology* 586(Pt 22):5383-5401.
55. Palty R, Stanley C, & Isacoff EY (2015) Critical role for Orai1 C-terminal domain and TM4 in CRAC channel gating. *Cell research* 25(8):963-980.
56. Zheng H, *et al.* (2013) Differential roles of the C and N termini of Orai1 protein in interacting with stromal interaction molecule 1 (STIM1) for Ca<sup>2+</sup> release-activated Ca<sup>2+</sup> (CRAC) channel activation. *The Journal of biological chemistry* 288(16):11263-11272.

57. Derler I, *et al.* (2013) The extended transmembrane Orai1 N-terminal (ETON) region combines binding interface and gate for Orai1 activation by STIM1. *The Journal of biological chemistry* 288(40):29025-29034.
58. Zhou Y, *et al.* (2016) The STIM1-binding site nexus remotely controls Orai1 channel gating. *Nature communications* 7:13725.
59. Changeux JP & Christopoulos A (2016) Allosteric Modulation as a Unifying Mechanism for Receptor Function and Regulation. *Cell* 166(5):1084-1102.
60. Bogdanov M, Zhang W, Xie J, & Dowhan W (2005) Transmembrane protein topology mapping by the substituted cysteine accessibility method (SCAM(TM)): application to lipid-specific membrane protein topogenesis. *Methods* 36(2):148-171.
61. Srikanth S, Yee MK, Gwack Y, & Ribalet B (2011) The third transmembrane segment of orai1 protein modulates Ca<sup>2+</sup> release-activated Ca<sup>2+</sup> (CRAC) channel gating and permeation properties. *The Journal of biological chemistry* 286(40):35318-35328.
62. Li Z, *et al.* (2011) Graded activation of CRAC channel by binding of different numbers of STIM1 to Orai1 subunits. *Cell research* 21(2):305-315.
63. Mullins FM, Park CY, Dolmetsch RE, & Lewis RS (2009) STIM1 and calmodulin interact with Orai1 to induce Ca<sup>2+</sup>-dependent inactivation of CRAC channels. *Proc Natl Acad Sci USA* 106(36):15495-15500.
64. Scrimgeour N, Litjens T, Ma L, Barritt GJ, & Rychkov GY (2009) Properties of Orai1 mediated store-operated current depend on the expression levels of STIM1 and Orai1 proteins. *J Physiol*.

65. Derler I, *et al.* (2009) A  $\text{Ca}^{2+}$  release-activated  $\text{Ca}^{2+}$  (CRAC) modulatory domain (CMD) within STIM1 mediates fast  $\text{Ca}^{2+}$  -dependent inactivation of ORAI1 channels. *J Biol Chem* 284(37):24933-24938.
66. Lis A, Zierler S, Peinelt C, Fleig A, & Penner R (2010) A single lysine in the N-terminal region of store-operated channels is critical for STIM1-mediated gating. *The Journal of general physiology* 136(6):673-686.
67. Derler I, *et al.* (2018) Authentic CRAC channel activity requires STIM1 and the conserved portion of the Orai N terminus. *J Biol Chem* 293(4):1259-1270.
68. Schindl R, *et al.* (2008) 2-aminoethoxydiphenyl borate alters selectivity of Orai3 channels by increasing their pore size. *J Biol Chem* 283(29):20261-20267.
69. Srikanth S, Yee MK, Gwack Y, & Ribalet B (2011) The third transmembrane segment of orai1 protein modulates  $\text{Ca}^{2+}$  release-activated  $\text{Ca}^{2+}$  (CRAC) channel gating and permeation properties. *The Journal of biological chemistry* 286(40):35318-35328.
70. Smart OS, Neduvélil JG, Wang X, Wallace BA, & Sansom MS (1996) HOLE: a program for the analysis of the pore dimensions of ion channel structural models. *J Mol Graph* 14(6):354-360, 376.
71. Word JM (2000) All-atom small-probe contact surface analysis: An information-rich description of molecular goodness-of-fit. *Ph.D. Thesis, Duke University*.
72. Word JM, *et al.* (1999) Visualizing and quantifying molecular goodness-of-fit: small-probe contact dots with explicit hydrogen atoms. *J Mol Biol* 285(4):1711-1733.
73. Hou X, Pedi L, Diver MM, & Long SB (2012) Crystal Structure of the Calcium Release-Activated Calcium Channel Orai. *Science* 338:1308-1313.

74. Fahrner M, *et al.* (2018) Communication between N terminus and loop2 tunes Orai activation. *J Biol Chem* 293(4):1271-1285.
75. Dong H, Klein ML, & Fiorin G (2014) Counterion-assisted cation transport in a biological calcium channel. *J. Phys. Chem. B* 118(32):9668-9676.
76. Chamberlain AK & Bowie JU (2004) Analysis of side-chain rotamers in transmembrane proteins. *Biophys J* 87(5):3460-3469.
77. Lovell SC, Word JM, Richardson JS, & Richardson DC (1999) Asparagine and glutamine rotamers: B-factor cutoff and correction of amide flips yield distinct clustering. *Proc Natl Acad Sci U S A* 96(2):400-405.
78. Shu X, *et al.* (2011) A genetically encoded tag for correlated light and electron microscopy of intact cells, tissues, and organisms. *PLoS Biol* 9(4):e1001041.
79. Souslova EA, Mironova KE, & Deyev SM (2017) Applications of genetically encoded photosensitizer miniSOG: from correlative light electron microscopy to immunophotosensitizing. *J Biophotonics* 10(3):338-352.
80. Bogeski I, Kilch T, & Niemeyer BA (2012) ROS and SOCE: recent advances and controversies in the regulation of STIM and Orai. *The Journal of physiology* 590(17):4193-4200.
81. Alansary D, *et al.* (2016) Thiol dependent intramolecular locking of Orai1 channels. *Sci Rep* 6:33347.
82. Chin JW, Martin AB, King DS, Wang L, & Schultz PG (2002) Addition of a photocrosslinking amino acid to the genetic code of Escherichiacoli. *Proceedings of the National Academy of Sciences of the United States of America* 99(17):11020-11024.

83. Klippenstein V, Ghisi V, Wietstruk M, & Plested AJ (2014) Photoinactivation of glutamate receptors by genetically encoded unnatural amino acids. *J Neurosci* 34(3):980-991.
84. Fierro L & Parekh AB (1999) Fast calcium-dependent inactivation of calcium release-activated calcium current (CRAC) in RBL-1 cells. *J Membr Biol* 168(1):9-17.
85. Zweifach A & Lewis RS (1995) Rapid inactivation of depletion-activated calcium current (ICRAC) due to local calcium feedback. *The Journal of general physiology* 105(2):209-226.
86. Mullins FM & Lewis RS (2016) The inactivation domain of STIM1 is functionally coupled with the Orai1 pore to enable Ca<sup>2+</sup>-dependent inactivation. *The Journal of general physiology* 147(2):153-164.
87. Scrimgeour N, Litjens T, Ma L, Barritt GJ, & Rychkov GY (2009) Properties of Orai1 mediated store-operated current depend on the expression levels of STIM1 and Orai1 proteins. *The Journal of physiology* 587(Pt 12):2903-2918.
88. Mullins FM, Yen M, & Lewis RS (2016) Orai1 pore residues control CRAC channel inactivation independently of calmodulin. *The Journal of general physiology* 147(2):137-152.
89. Mullins FM, Park CY, Dolmetsch RE, & Lewis RS (2009) STIM1 and calmodulin interact with Orai1 to induce Ca<sup>2+</sup>-dependent inactivation of CRAC channels. *Proceedings of the National Academy of Sciences of the United States of America* 106(36):15495-15500.
90. Lee KP, *et al.* (2009) Molecular determinants of fast Ca<sup>2+</sup>-dependent inactivation and gating of the Orai channels. *Proceedings of the National Academy of Sciences of the United States of America* 106(34):14687-14692.

91. Frischauf I, *et al.* (2011) Cooperativeness of Orai cytosolic domains tunes subtype-specific gating. *The Journal of biological chemistry* 286(10):8577-8584.
92. Srikanth S, Jung HJ, Ribalet B, & Gwack Y (2010) The intracellular loop of Orai1 plays a central role in fast inactivation of Ca<sup>2+</sup> release-activated Ca<sup>2+</sup> channels. *The Journal of biological chemistry* 285(7):5066-5075.
93. Valley CC, *et al.* (2012) The methionine-aromatic motif plays a unique role in stabilizing protein structure. *The Journal of biological chemistry* 287(42):34979-34991.
94. Reid KSC, Lindley PF, & Thornton JM (1985) Sulphur-aromatic interactions in proteins. *FEBS letters* 190(2):209-213.
95. Zal T & Gascoigne NR (2004) Photobleaching-corrected FRET efficiency imaging of live cells. *Biophysical journal* 86(6):3923-3939.
96. Fiser A & Sali A (2003) Modeller: generation and refinement of homology-based protein structure models. *Methods in enzymology* 374:461-491.
97. Jo S, Kim T, & Im W (2007) Automated builder and database of protein/membrane complexes for molecular dynamics simulations. *PloS one* 2(9):e880.
98. Best RB, *et al.* (2012) Optimization of the additive CHARMM all-atom protein force field targeting improved sampling of the backbone phi, psi and side-chain chi(1) and chi(2) dihedral angles. *J Chem Theory Comput* 8(9):3257-3273.
99. MacKerell AD, *et al.* (1998) All-atom empirical potential for molecular modeling and dynamics studies of proteins. *The journal of physical chemistry. B* 102(18):3586-3616.
100. Klauda JB, *et al.* (2010) Update of the CHARMM all-atom additive force field for lipids: validation on six lipid types. *The journal of physical chemistry. B* 114(23):7830-7843.

101. Jorgensen WL, Chandrasekhar J, Madura JD, Impey RW, & Klein ML (1983) Comparison of simple potential functions for simulating liquid water. *The Journal of chemical physics* 79(2):926-935.
102. Abraham MJ, *et al.* (2015) GROMACS: High performance molecular simulations through multi-level parallelism from laptops to supercomputers. *SoftwareX* 1-2:19-25.